Προσφορά στήν Ἀθηνά

γιά τῆς Σέρυς Θεῖο χάρισμα τῆς σοφίας

CONTENTS

ABSTRACT

A mathematical model has been developed, simulating various aspects of an iron blast furnace, for the purpose of analysing its behaviour. This involved the simulation of a counter current compressible gas flow, through a packed bed, dealing with the momentum and thermal energy of both phases. Directional resistances were added to the gas momentum, so as to account for the interphase friction caused by the packed bed. This enabled the prediction of the cohesive zone geometry, together with the active coke and stack, thus providing an important step for a successful analysis. The availability of multi-phase codes to solve such a system was limited and those existing being inadequate to represent these kinds of problems. What resulted was, the development of an algorithm to solve for two phases (gas and solids) with interspersed counter current flow, where the solids behaved as a packed bed. The algorithm developed is an enhanced version of existing algorithms.

As well as the numerical model, a physical model of the raceway was developed, using dry ice particles to simulate the packed bed. The sublimation properties of the ice give a more realistic simulation to coke combustion, compared to the use of inert particles. The results of the experiment brought to light the effects of particle-particle interaction as being most significant in enabling the solids bed to move freely, around and into the raceway.

From numerical modelling results, it is concluded that the ore:coke charging profile plays a dominant role in furnace behaviour. More interestingly, the gas distribution was not affected by raceway geometries when the cohesive zone was not in the immediate vicinity. It was therefore concluded that, the size and shape of the raceway zone has little influence on the gas distribution in the iron blast furnace.

ACKNOWLEDGEMENTS

I would like to express sincere gratitude to my supervisors Dr Mark Cross and Dr Vaughan Voller for their constant interest and support throughout. In particular, my appreciation is further extended to Dr Cross for his ongoing assistance.

I am also indebted to Professor Nikos Markatos for his initial guidance on the use of the computer code PHOENICS, and for the keen interest he has shown.

In conjuction I would like to extend my appreciation to Professor J W Evans for his continual guidance on the experiments performed at the University of California, Berkeley; and also to Professor D W Fuerstenau for agreeing to finance the work.

I also wish to thank my family, friends and colleagues for all their help, and for keeping me sane during the last few months.

Many thanks also to Mr F B Traice and colleagues at the British Steel Corporation Teesside Laboratories for permitting my site visit and many data acquisitions.

Finally, I would like to thank Edie McFall for her devotion to the typing of this thesis; and for tolerating and surviving my pedantocratic attention to detail.

CHAPTER 1

INTRODUCTION

1.1 The Iron Blast Furnace Process

The iron blast furnace process is the means by which hot metal is produced by the interaction of reducing gases. The furnace itself is a packed bed reactor into which alternate layers of coke and ferrous burden materials are charged at the top while hot air blast is blown through tuyeres at the bottom around the furnace circumference. A schematic diagram of the internal structure of a large blast furnace is shown in Figure (1.1).

The hot air blast, on entering the furnace via the tuyeres, reacts with the coke particles within a combustion zone, known as a raceway, forming the reducing gases:carbon monoxide and hydrogen. The gas flow then travels upwards through the furnace to react with the iron oxide, in the ferrous layers, reducing these iron ores to molten iron. The layers of burden materials descend into the furnace and, as they descend, the gas solid interaction causes an increase in the temperature of the material due predominantly to convective heat transfer.

The packed bed of ore and coke layers retains its layered structure until the temperature of the ferrous material reaches its softening temperature. This region of the blast furnace is known as the stack or lumpy zone, and it is in this zone that the reduction of the higher oxides takes place. The temperature of the gas falls rapidly as it passes through the stack due to cooling by the incoming solids.

Once the ferrous material reaches its softening temperature it becomes a cohesive mass which has a low permeability to gas flow. As the temperature increases further, the ferrous material melts and

flows downwards through the furnace to the hearth. The softening and melting mechanism results in a series of annular rings of softened material, separated by layers of coke. Due to these rings being virtually impervious to gas flow, the ascending gases must pass horizontally through the coke 'slits' in order to pass into the top of the furnace. This region of the furnace is consequently known as the cohesive zone or softening-melting zone.

Below this zone is a region known as the active coke zone in which the remaining coke particles descend with molten ore percolating through. Gases exiting the raceway then rise through the active coke zone transferring heat to the descending coke and dripping iron. The hot blast, entering the furnace through the tuyeres, has such a high velocity that the blast clears a 'raceway' of gas and rapidly hurtling coke in front of each tuyere. The raceways are bounded by coke, some loosely packed due to the rapid ascent of raceway gas and lack of fines build up. As coke pieces periodically fall into the raceways they are consumed by the incoming air, and hence the whole bed is gradually moving down to be combusted to produce the reducing gases.

The molten material flowing from the melting part of the cohesive zone passes through the active coke zone to the bottom of the furnace. This zone is called the hearth, and the liquids collect in this zone to be tapped off periodically.

1.2 Research Aims

An understanding of the gas flow through the ironmaking blast furnace is of fundamental importance for the study of furnace phenomena and ultimately the control of furnace productivity.

In the cohesive zone, due to the impermeable nature of the softening layers, the gas flowing upwards from the raceway must pass predominantly through the permeable coke 'slits' in order to reach the stack zone above. Consequently, the geometrical shape of the cohesive zone, together with its position in the furnace, is one of the major factors in determining the gas distribution through the upper zone of the furnace. Therefore, one of the aims is to be able to successfully determine the position and shape of the cohesive zone so as to obtain an accurate description of gas flow and heat exchange in the region.

Another important factor in the determination of gas flow is the raceway. The work on raceway phenomena, to date, has been concerned with raceway depth and height influenced by various parameters such as blast velocity, particle size and density. While it is desirable to understand the formation mechanism of the raceway it is more important to investigate the role of this region with respect to the complete furnace process. Therefore, a further aim of the research is to clarify the role of the raceway in terms of the effects on overall furnace operation. During this investigation it will also be necessary to look at other factors that affect the gas flow phenomena in connection with the overall theme of the research (ie. gas flow and thermal distribution).

1.3 Existing Philosophy

Although the iron blast furnace is an extremely well established traditional process, it still provides the vast majority of hot metal across the world. Due to its substantial importance there has been a great deal of research on every aspect of the process, both mathematically and physically.

The research underaken by many authors has spanned from chemical kinetic models to the study of furnace hydrodynamics. Much work has been done by authors in chemical kinetics, such as: Perrott and Kinney (1923); Kinney, Royster and Joseph (1927); Muchi (1967); Fielden and Wood (1968); Yagi and Muchi (1970); Yagi and Szekely (1977a),(1977b); Turkdogan (1978); Sohn (1978a),(1978b); Mackin (1979); Hatano et al (1980); Togino et al (1980); Grebe and de Haas (1983). However, the current research is involved in the modelling of furnace hydrodynamics, with particular interest in the behaviour of the gas distribution.

The initial stages to mathematically modelling the blast furnace would entail an analysis of gas flow through porous media. Ergun and Orning (1949) looked at this problem by studying fluid flow through randomly packed columns and fluidized beds. It was shown that the ratio of pressure gradient to superficial fluid velocity was a linear function of fluid mass flow rate. On obtaining the constants in the linear function from experimentation, Ergun (1952) showed that pressure losses are caused by simultaneous kinetic and viscous energy losses. Conditions were chosen so that the effect of one variable at a time could be considered, thereby enabling the relationship to be examined from its dependence on various parameters. This, however, did cause restrictions of incompressible and isothermal conditions. The relationship of Ergun formed the basis to analyse flow through porous media for further research and therefore enabled the analysis of furnaces to develop.

Work later considered by Stanek and Szekely (1972) was concerned with two dimensional flow of a fluid through a packed bed having variable void fraction. They regarded this as a first step to

understanding heat transfer and mass transfer, concluding that lateral distribution in porosity can cause flow maldistribution. While this study assumed isothermal and incompressible conditions, Stanek and Szekely (1973) took their ideas further and studied the flow maldistribution in two dimensional packed beds involving non-isothermal systems. They also extended the ideas to compressible fluids and systems in cylindrical coordinates. The conclusions were that flow maldistribution could be caused by variations in resistance, which in turn were caused by changes in porosity and temperature. Through the statement of the Ergun equation in vectorial form, Stanek and Szekely (1974) then presented a formulation for three dimensional flow of fluids through packed beds having a spatially variable resistance to flow. The vectorial form enabled convenient solution by numerical methods leading to a better understanding of flow maldistribution in packed beds.

Poveromo, Szekely and Propster (1975) showed how flow maldistribution in the iron blast furnace may be analysed via the vectorial form of the Ergun equation, as proposed earlier by Stanek and Szekely. Cold model experimentation illustrated the validity of this method. The experimentation by Szekely and Poveromo (1975b) reported on flow maldistribution in packed beds containing side streams and deliberately created spatially non-uniform resistance to flow. The measurements compared with numerical solution of a vectorial form of the inertial term of Ergun's equation and confirmed the existence of preferential flow in the vicinity of the walls, even for uniformly packed beds.

Kuwabara and Muchi (1975), on wishing to clarify the characteristics of non-uniform flow of gas through layered burdens, solved flow

equations of continuity and motion via Ergun's equation. This did clarify the effective role of the longitudinal and radial distributions of process variables in an existing Japanese furnace. In the 1970's Japanese investigators quenched four operating furnaces and then carefully dissected their internal solid material structure. Kanabara et al (1976) reported on the operation, locating the partially melted region and determining flow in the furnace and positions of reactions. Numerous reports resulted from the operation, and, as a result, transformed the conventional understanding of the blast furnace and provided clear evidence of the important role of the gas distribution in the process. (More recently, Bonnekamp et al (1984) performed a furnace dissection. However, they realised that the influence of quenching water could cause severe changes in the physical and chemical condition of the burden materials. As a result they used a new media, nitrogen, as the cooling medium. The analysis of the results is at present being performed. It was identified that the burden plays an important role in gas distribution. Kuwabara and Muchi (1977a,b) studied the characteristics of the blast furnace with horizontally layered burdens and then radial distribution of process variables. The models were defined by a set of equations concerning the unsteady-state heat transfer, the overall heat and mass balances and the pressure drop in each layer via Ergun. These models were used to analyse features of operating furnaces and showed agreement with operation data. In a later study, Kuwabara and Muchi (1977c) analysed characteristics of gas flow, in the shaft of a blast furnace, from a theoretical standpoint. The shaft had a layered ore and coke burden and solved flow via continuity and motion, the Ergun equation being used to satisfy motion. The results highlighted maldistribution due to resistance changes in the layers.

Since the Japanese dissections, the research moved to the areas of flow maldistribution and later its causes, being: resistance variations due to burden configuration. Szekely and Propster (1977) performed an experiment on resistance of layer burden to gas flow using blast furnace materials. It was found that when smaller materials were placed on larger materials (ie. ore pellets on coke) the resistance of the interfacial regions contributed appreciably to the overall resistance to flow. In a later experiment, Szekely and Propster (1979a), then performed a similar analysis only using glass beads as the packed bed. The relationship between pressure drop and gas flow rate was developed for various configurations of layer charge arrangements; and as in the previous paper, 1977, they found the interface of layers to have significant effect on overall flow resistance. Szekely and Propster (1979b) then used a vectorial form of Ergun's equation to mathematically model spatially non-uniform gas flow through blast furnace burdens. Agreement with experimentation led them to conclude that serious flow maldistribution will necessarily occur in all blast furnace burdens where the solid charge is not layered uniformly in horizontal layers.

Propster and Szekely (1979) took their model, previously described as a vectorial form of Ergun's equation to model spatially non-uniform gas flow, and used it to show the effects of maldistribution of the gas by the active coke and cohesive zone. This led to a conclusion about the importance of these zones affecting the resistance to flow. In a similar direction, Wakayama et al (1979) obtained results, via experiments and furnace dissection data, regarding relationships between burden distribution and furnace operation. The findings showed that burden distribution

has an important role to play on the configuration of the cohesive zone.

Important developments occurred regarding the use of Ergun's equation for flow through blast furnace burdens. Yoskizawa (1979) developed a proper tensorial form of the D'Arcy-Ergun equation and showed that the replacement of a tensor by a scalar, in the equation, still produces satisfactory results. More important was the development, by Cross and Gibson (1979), of a practical theory to describe the gas flow through multilayered porous structures, by characterising layered structures as anisotropic materials. The formulation involved modification of the vectorial Ergun equation and definition of directional resistances, reflecting influences of physical properties, proportions and inclination of layers. Cross et al (1979) then performed a number of experiments to verify the validity of the 'anisotropic' theory. The results showed that the theory adequately: describes flow across multilayered regions, reflects the change in pressure gradient when the physical properties in the region vary, and provides a good description of gas flow distribution in a region of similar configuration to a blast furnace. With this newly developed theory various furnace characteristics were investigated (Cross, Gibson and Hill (1980); Cross et al (1981)).

Work continued on the analysis of the cohesive zone, Tashiro et al (1980) performed an experiment to clarify the dynamic behaviour of the zone, using wax grains and coke. This method was used to study the likely factors responsible for the cohesive zone formation. It was found that, as general contributors to the formation of the cohesive zone, the effects of burden distribution and blast volume

were clarified to provide an operating guideline for the geometrical control of the cohesive zone.

Clarification was required for the previously developed models of Cross et al, as a result two experiments were performed, both analogues of a blast furnace (McIntee and Robertson (1981); McIntee et al (1982)). These models were based on the use of wax to simulate iron ore, and naphthalene or plastic to simulate coke in each analogue respectively. Comparisons between analogue measurements and model predictions showed successful prediction of some features, however, it was pointed out that modifications were required as regards pressure in the cohesive zone.

More recently, models have tried to incorporate as much of the blast furnace process as possible. Yagi, Takeda and Omori (1982) and Kudoh et al (1983) produced results from a two dimensional gas flow model, solved via a finite element method. The gas flow was described by a multi-dimensional Ergun equation and continuity equation, the solids flow approximated by potential flow, and energy via heat balance equations. They concluded that radial distribution predominantly controls flow maldistribution, which in turn controls temperature distribution. In this analysis however, the cohesive zone had to be fixed during the solution, unlike work later done by Cross et al (1984). This new work was an inert model which accounted for interaction of gas flow distribution, heat exchange and melting influences, therefore predicting the cohesive zone. The gas flow was described by the newly developed Ergun relationship of Cross and Gibson (1979).

Another area of interest, as specified in the research aims, is that

of the raceway zone. Work on this area started in the early 1950's. Elliot, Buchanan and Wagstaff (1952) performed model studies and high speed photography, showing a rapidly moving raceway of gases and coke before each tuyere. They concluded that the effect of changing penetration of blast is physical not chemical, which in turn would have an appreciable effect on the flow of gas further up the stack. Wagstaff (1953) took these studies on and provided a correlation for the penetration of the blast while suggesting further evidence that the coke is densely packed in the centre of the furnace to form the 'dead man'. Another observation was that the raceway was spherical in shape. A few years later, further work by Wagstaff and Holman (1957) resulted in an improved correlation of raceway measurements. Good agreement was obtained between experimental and plant data despite the model being inert, and it was observed that variation of the tuyere diameter had an irregular effect on the magnitude of penetration. A new correlation of blast penetration in model and operating blast furnaces was presented by Gardner (1960). His objections raised in previous correlations concerning the ratio with hearth area were overcome by the introduction of a new ratio. As a result, his previous suspicions, of the role of the tuyere diameter being of small importance in the determination of magnitude of penetration, were confirmed.

McCutcheon (1965) and Hillnhüter et al (1975) acquired data on various furnaces which aided a better understanding of the philosophy of raceway formation.

Via a macroscopic momentum balance, Szekely and Poveromo (1975a) developed a mathematical model for predicting the size of the raceway region. The formulation involved the establishment of a

force balance where the radial momentum transfer from the incoming gas was balanced against the weight of the bed. Although there was no accounting for hanging or bridging, the model agreed well with an experiment set up for the purposes of validation. Hatano et al (1977) showed the possibility for estimation, of raceway depth, in conjunction with Wagstaff's equation. His experimental blast furnace simulated the lower part of a commercial furnace and observations were made on the chemistry of fuel burning and gas tracking.

Later investigations moved on to observe the effects of liquid iron dripping and the role of this liquid in the vicinity of the raceway. Szekely and Kajiwara (1979a) presented a mathematical model to describe the counter-current flow of a gas and liquid stream through a packed bed of particles. Their experimental measurements, Szekely and Kajiwara (1979b), were concerned with the counter-current flow of air and water through glass beads, under conditions such that both the gas and liquid streams are maldistributed. Results showed that gas tends to displace liquid from the vicinity of the tuyeres and there exists a 'dry zone' where the gas flow effectively displaced virtually all the liquid. Kuwabara et al (1981) proposed theoretical and experimental studies to clarify the physical and chemical behaviour of the tuyere combustion zone. The results showed that the maximum consumption of coke occurs at the intermediate region of the raceway and can be altered by changing characteristics of blast or particle properties. The solid flow pattern around the tuyere combustion zone was visualised by two dimensional equipment and the sublimation of dry ice. The observations indicated that the solids descending toward the tuyere combustion zone behave like a viscous flow. Durnov et al (1981)

studied the structure and hydrodynamics of the raceway of a blast furnace on a cold model. The model established the effects of the tuyere parameters, blast parameters and the amount of liquid products of smelting on the configuration of raceway, pressure and velocity. The overall topography of a raceway had therefore been determined.

A mathematical model of the raceway was discussed by Hatano et al (1983), which had been developed by the use of fluid dynamics theory. The model set up a raceway boundary depending on interactive forces and then specified the equation of motion and coke density to use. A similar model was set up, NERDD project (1983), to solve for the transport of mass and momentum, specifying the raceway region rather than solving for it. In both models it was shown that the gas from the tuyere flows as a jet straight into the raceway having sufficient inertia to carry it to the rear of the raceway where high pressures were observed causing the flow to travel upwards. Another raceway model was developed by Taggart et al (1983) for gas flow through the raceway. The simulation had a specified raceway geometry and it predicted the existence of the upper and lower recirculation zones which are responsible for the rotary movements of entrained particles.

Thus it can be observed that research into the blast furnace has been extensive over the years, though each investigation leaving new areas of research to improve on. Although each specialised area has been investigated by many workers, the need for process analysis models, to observe the effects of various parameters on overall furnace operation, is still apparent.

CHAPTER 2

EXPERIMENTAL RACEWAY MODEL

2.1 Introduction

Experimental work on raceway phenomena has been undertaken as early on as 1952, when Elliot, Buchanan and Wagstaff (1952) observed raceways, as a result of their model studies using wood particles and high speed photography of operating furnaces. Wagstaff (1953) developed the model further by using wood particles and crushed coke to simulate the raceway, and, together with Holman, in 1957, improved their correlation for blast penetration. McCutcheon (1965), and Hillnhütter et al (1975) investigated the raceway by acquiring data from various furnaces and added to the understanding of raceways. The possibility of estimating raceway depth in conjunction with Wagstaff's equation was investigated by Hatano et al (1977), by their simulation of the lower part of a commercial furnace.

Kuwabara et al (1981) performed theoretical and experimental studies to clarify the physical and chemical behaviour of the tuyere combustion zone of blast furnaces. Their results showed characteristics of coke consumption and solids flow behaviour. The flow pattern of the solids was visualised by two dimensional equipment and the sublimation of dry ice. Kuwabara et al (1983) later extended the studies to burden flow caused by factors such as raceway and cohesive zone formation. The moving bed was simulated by the use of dry ice and glass beads, the sublimation of dry ice, again, simulating coke consumption.

In past studies, many materials have been used to simulate coke in the raceway region, such as glass beads, wood particles, polystyrene and carbon to name a few. Many experiments performed, using these particles, have the limitation that the packed bed is inert and

therefore does not simulate coke combustion. The use of dry ice has been investigated before, particularly in the work by Kuwabara et al but not as extensively as would be believed. The apparent advantage of this material, in cold model studies, is the sublimation property causing the dry ice to be consumed as in coke combustion. The effective features of using this material for its properties are that: the downward movement of solids is inherent in the model, and the constant sublimation of dry ice pellets in the raceway results in a solids flow into the raceway that is analogous to coke flow in the real furnace.

The original aim of the current research was to develop a mathematical model of the blast furnace together with a predictive model of the raceway region. The objectives of the experiment was to develop a technique for validating the raceway model. It was desired to see the effects of gas flow on raceway formation so as to attempt to validate not only the raceway model itself, but also its role in furnace behaviour via its sensitivity to gas flow. The experiment was therefore set up to see the effects of different blast rates on raceway size and shape. The realisation of the role of the raceway became apparent later in the investigation and consequently the predictive raceway model was not pursued. At this point the experimental technique had been designed and the raceway studies underway. Much was observed as to the behaviour of the raceway region and the behavioural characteristics of burden descent, thus giving insight into the complex problems of furnace modelling.

2.2 Experimental Design [Part I]

The design of the complete experimental system was broken down into

two problems, the furnace design and that of the air delivery system. A schematic diagram of the air delivery system to furnace is given in Figure (2.1). The set up shown is for the air delivery to a single tuyere in the furnace; the complete design involves the sharing of meters and gauges together with a multiple hookup of compressed air cylinders to a single delivery line.

The data required from the air delivery system was the gas mass flowrate and temperature on entering the tuyere. The temperature was obtained via the use of thermocouples, while the mass flowrate was obtained from the relationship between temperature, absolute pressure and pressure gradient through an orifice meter. (The method of measuring the mass flowrate is explained fully in section 2.2.2).

The reason for such an apparently complex mass flow measurement was the desire to attain an accurate account of the flow conditions.

2.2.1 Furnace construction

The initial stage of the furnace design was to make assessments about the construction of the experimental system. It was necessary to establish what approximate raceway dimensions would be obtained for the blast rates that could be supplied. The correlations available, for predicting raceway depth and height, were those of Wagstaff, Gardner or Szekely and Poveromo. The most convenient appeared to be that of Szekely and Poveromo (1975a), therefore it was decided to use their correlation as a preliminary study.

They proposed a two and three dimensional macroscopic momentum balance using the following simplifying assumptions:

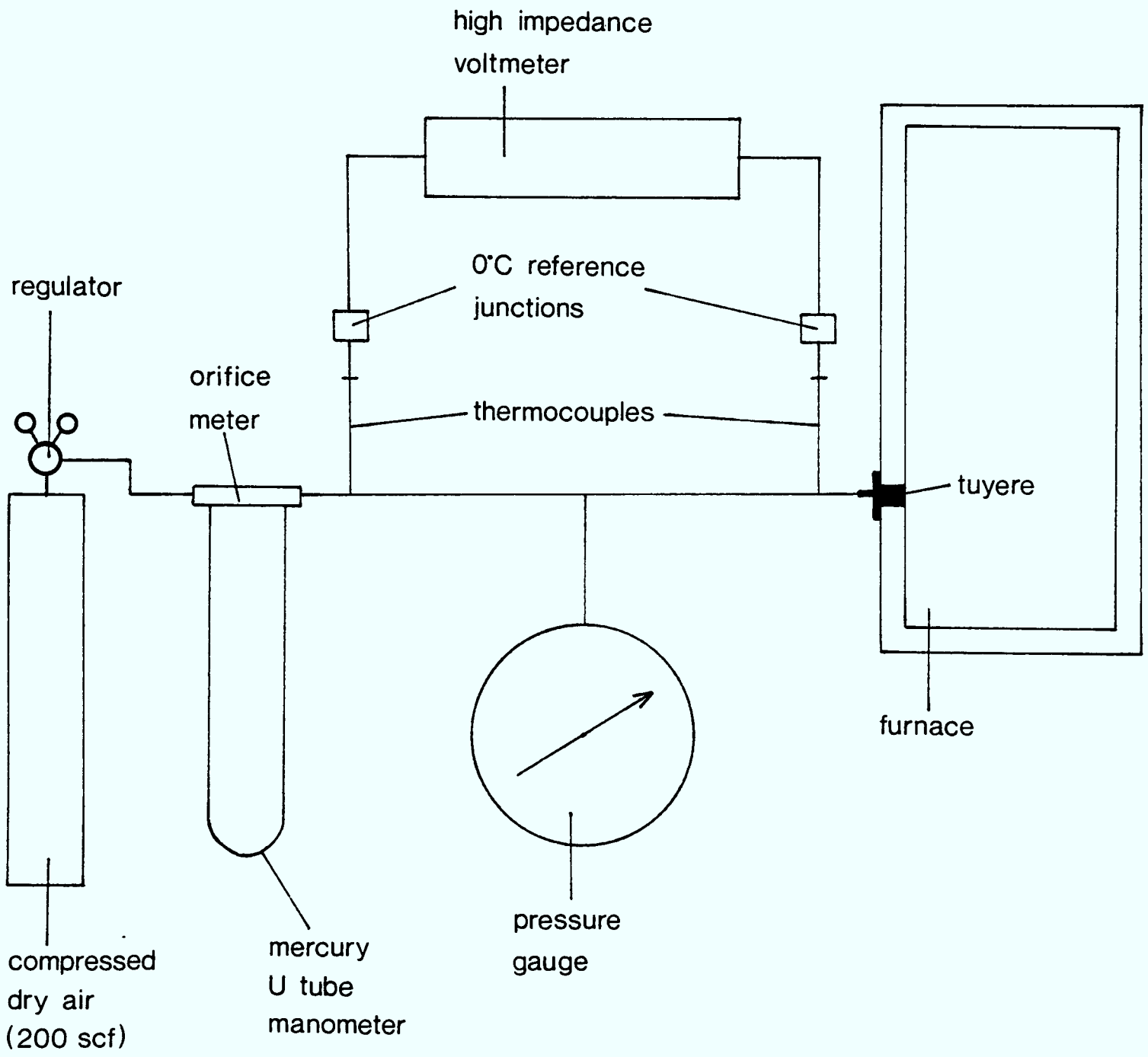

Figure 2.1: Schematic diagram of experimental setup

i) the raceway was assumed spherical and interaction between tuyere cavities neglected,

ii) the effect of non-uniform particle size and the presence of percolating liquid was neglected,

iii) isothermal conditions were assumed throughout,

iv) in deriving the macroscopic momentum balance equation it was assumed that the gas leaving the raceway passed through only a fraction of the total surface area of the raceway cavity.

These assumptions were regarded as the most critical and it was recognised that they formed a gross idealisation. However, the penetration distance obtained is thought to be a reasonable guide as shown in comparison with experimental and plant scale data.

The three dimensional momentum balance developed, is written as

$$R_r'^2 = \frac{P_o^2 V_o^2 D_o^2 M_A \pi^2}{4 P_r R T \epsilon_r^2 (1-\epsilon_b) \rho_b g h_b} + F_r'' \qquad (2.1)$$

where

$$F_r'' = \frac{F_r'}{2P_z} \qquad (2.2)$$

It was shown that F_r' is related to the viscous forces exerted by the gas, and that on experimentation F_r'', the empirical term, is negligible for most conditions. Therefore equation (2.1) provides a simple relationship for the evaluation of R_r'. P_r, the pressure inside the void, can be measured experimentally or calculated via

the one dimensional Ergun equation, similar to equation (4.5), where

$$-\frac{\Delta p}{L} = \frac{P_{top}-P_r}{h_b} \qquad (2.3)$$

Standard values were prescribed to the variables on the r.h.s. of equation (2.1); while, varying one or two parameters at a time gave indication to the range and limits of the variables, as regards raceway radius. The standard values are given in Table (2.1) together with the nomenclature for equations (2.1) to (2.3). It must be noted that the nomenclature used in these equations does not refer to the standard nomenclature throughout the thesis, and the extra nomenclature and data refers to the calculation of P_r via Erguns equation.

On completion of this initial study, it was found that the particle diameter had little effect on the raceways' predicted size. However, it must be noted that Szekely and Poveromo stated that if the particle size exceeded some unknown value then a distinct raceway is no longer observed but rather a region of intense circulation. Varying other parameters gave a raceway predicted radius range of 0·04-0·15m. Therefore if the operating parameters are within the ranges tested then it is predicted a raceway will form, and of reasonable size to acquire data.

From this study, therefore, it was decided that the furnace should be a 60° pie slice to allow a number of tuyeres to be operated, with an approximate radius of 0·5m and height 1m. A photograph of the furnace and tuyere constructions can be seen in Figure (2.2). The model was built of double walled clear PVC. Using an auxiliary

Nomenclature			Standard Values
R_r'	=	three dimensional raceway radius (m)	Predicted
P_o	=	pressure at tuyere ($kg/m/s^2$)	$1{\cdot}5\times10^5$
V_o	=	velocity of gas at tuyere (m/s)	$f(G_o,D_o)$
D_o	=	diameter of tuyere (m)	0·02
M_A	=	molecular weight of gas (air)	28·95
P_r	=	pressure inside void ($kg/m/s^2$)	f(Ergun)
R	=	universal gas constant (J/mol/K)	8314·4
T	=	temperature (K)	291
ϵ_r	=	surface porosity of raceway "walls"	0·3
ϵ_b	=	porosity of the bed	0·4
ρ_b	=	density of the bed (kg/m^3)	1565·4
g	=	gravitational constant (m/s^2)	9·81
h_b	=	height of bed above tuyere (m)	0·7
P_{top}	=	top pressure ($kg/m/s^2$)	$1{\cdot}0\times10^5$
G_o	=	gas mass flowrate (kg/s)	0·015
μ	=	laminar viscosity (kg/m/s)	$1{\cdot}488\times10^{-5}$
ρ_A	=	density of gas (air) (kg/m^3)	1·293
D_p	=	diameter of solid particles (m)	0·01

Table 2.1: Nomenclature and standard values for Szekely and Poveromo equation, and Ergun equation.

etween the double walls and this results being free from condensation, even when filled with dry ice. The dimensions of the model furnace are given in Figure (2.3) and those of the tuyere constructions in Figure (2.4).

Five tuyeres were mounted onto the furnace and their positions are shown in Figure (2.5). (The tuyeres were mounted straight and not facing the furnace centre, this was due to restrictions with working lathe machinery). Each tuyere position was interchangeable with a different diameter nozzle, the range available being 0·5cms, 1cm, 2cm and 3cm tuyere diameters.

2.2.2 Air delivery system

The air supply was available to the experiment in the form of compressed air cylinders, each with a capacity of 200scf (standard cubic feet), and distributed via Matheson regulators (model 8). It was necessary that the air had little moisture content so as to avoid freezing in the furnace. The moisture content in a typical cylinder was 0·2 parts per million with a dew point of -84°C, well below the sublimation temperature of dry ice (-78·5°C). Due to the low moisture content and dew point, the problem of moisture entering the furnace, freezing and bonding dry ice particles together was eliminated, therefore permitting the uninhibited flow of solids. The problem of room air descending into the furnace is of minor consequence due to the dry air gas flow ascending. The dry air properties also permitted the internal faces of the double walled cavity to remain condensation free and permit a good visual surface for photography of raceway formation.

not to scale

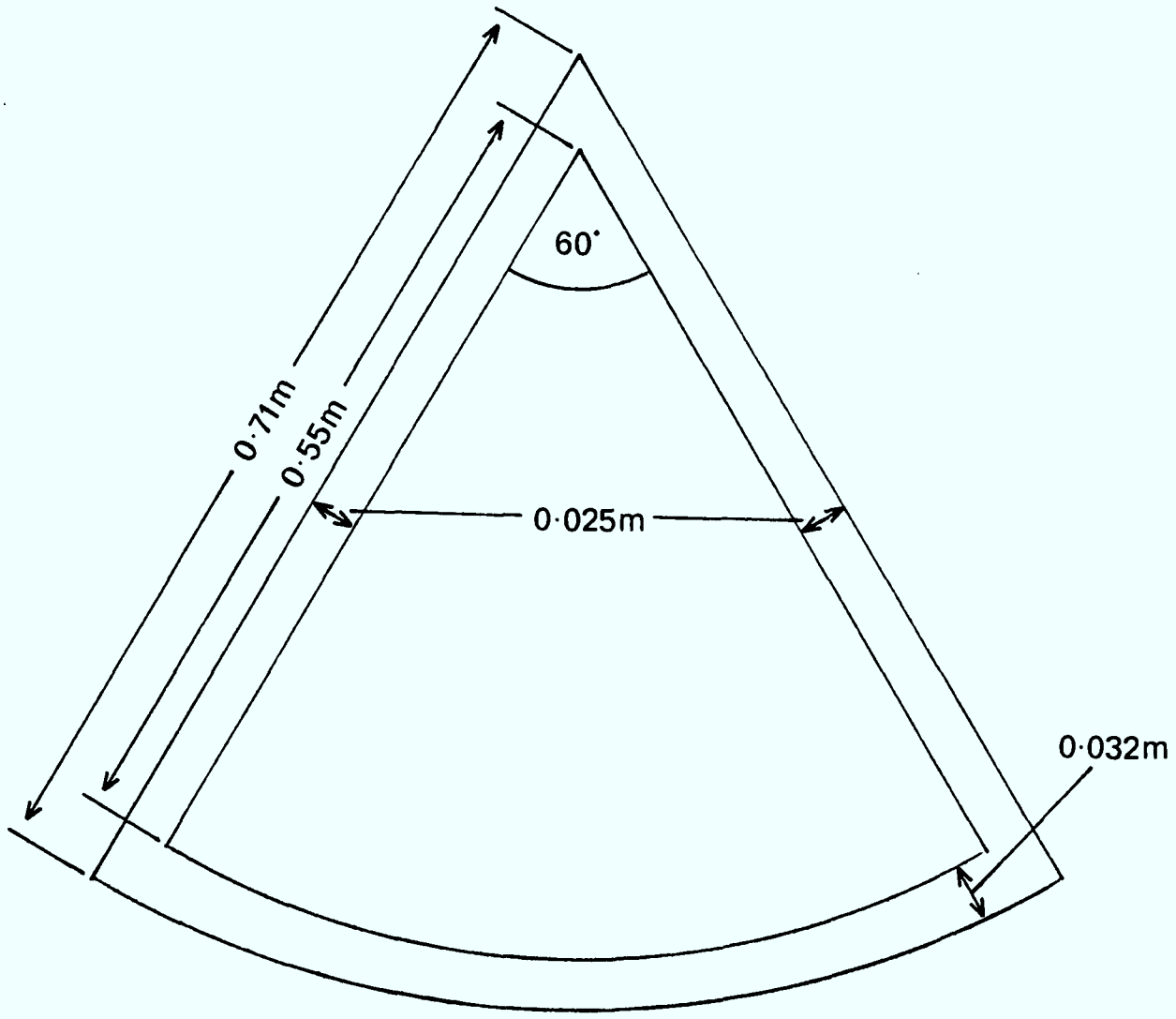

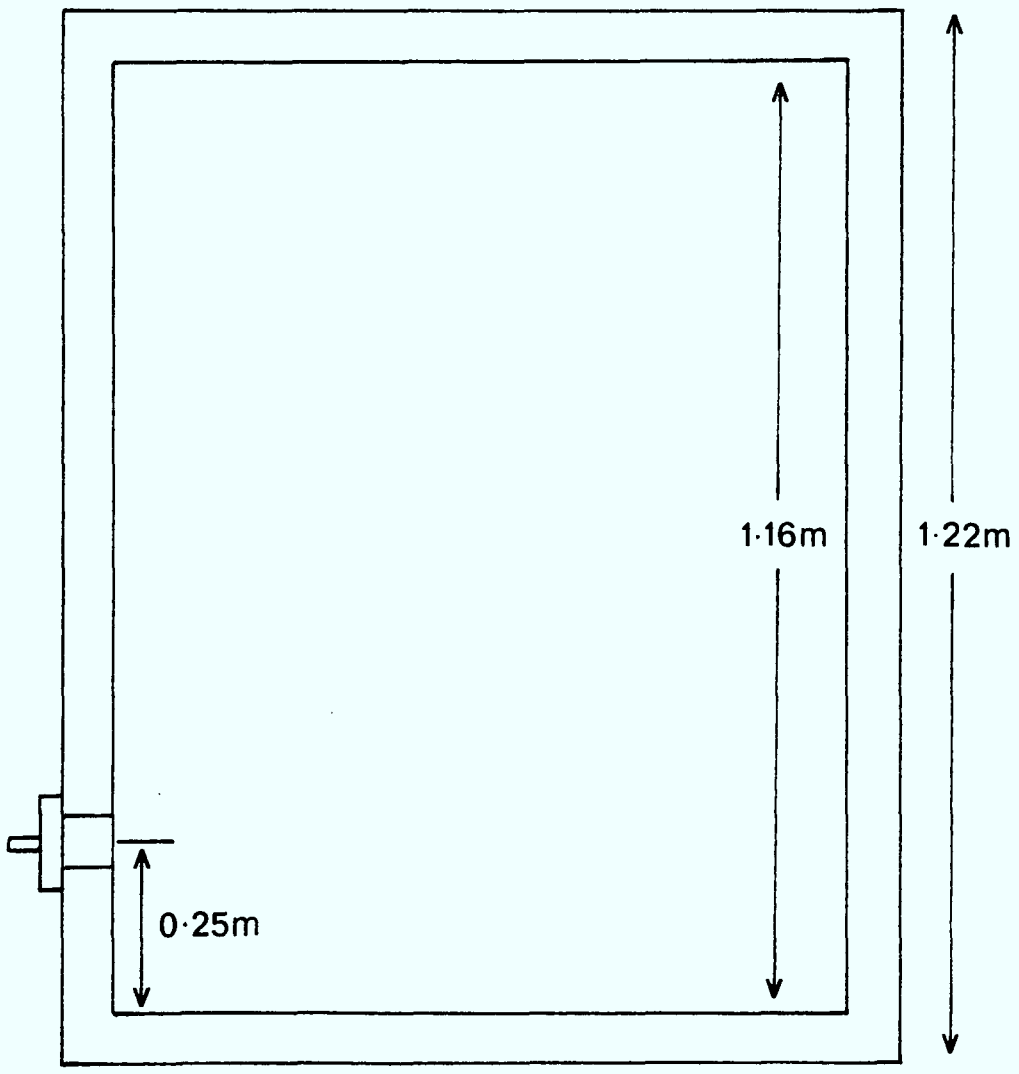

Figure 2.3: Furnace dimensions

not to scale

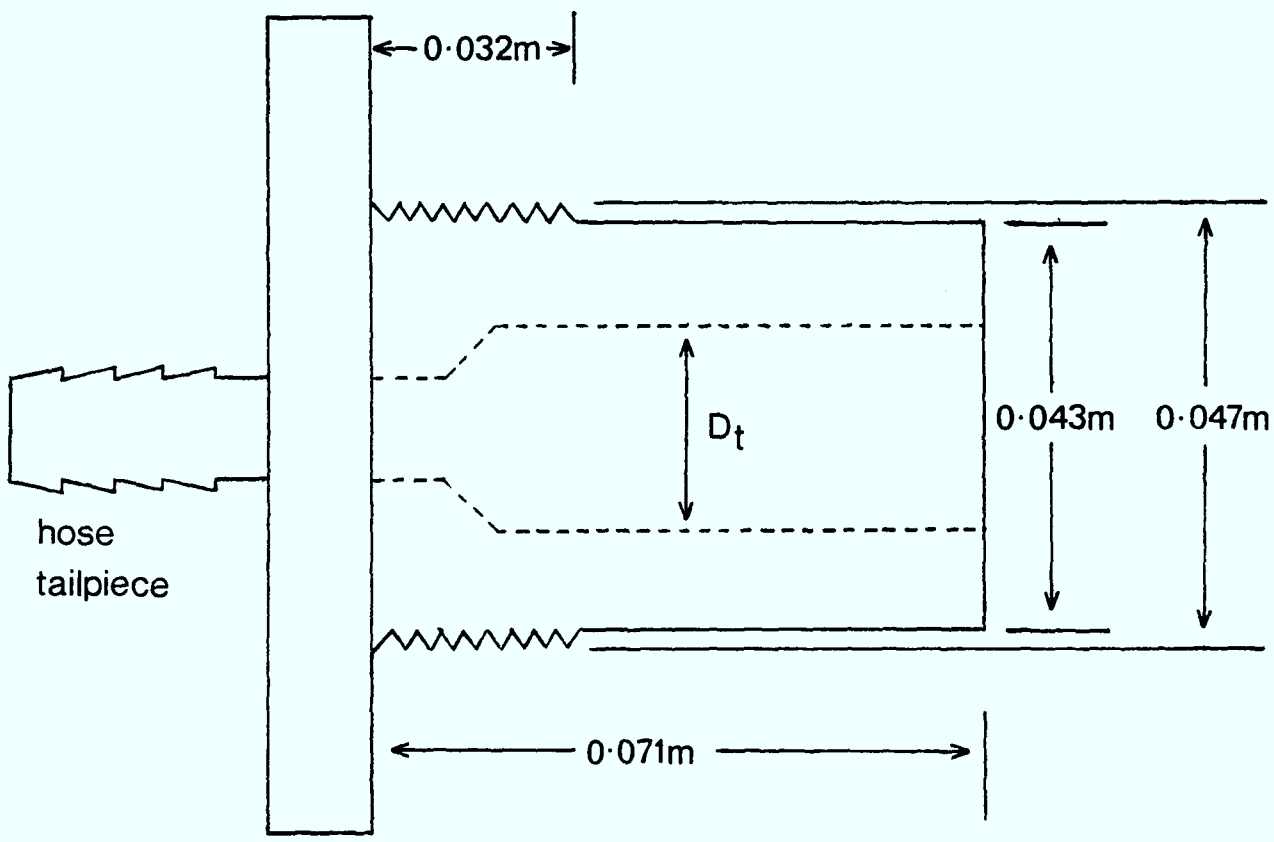

D_t = tuyere diameter

Figure 2.4: Tuyere dimensions

not to scale

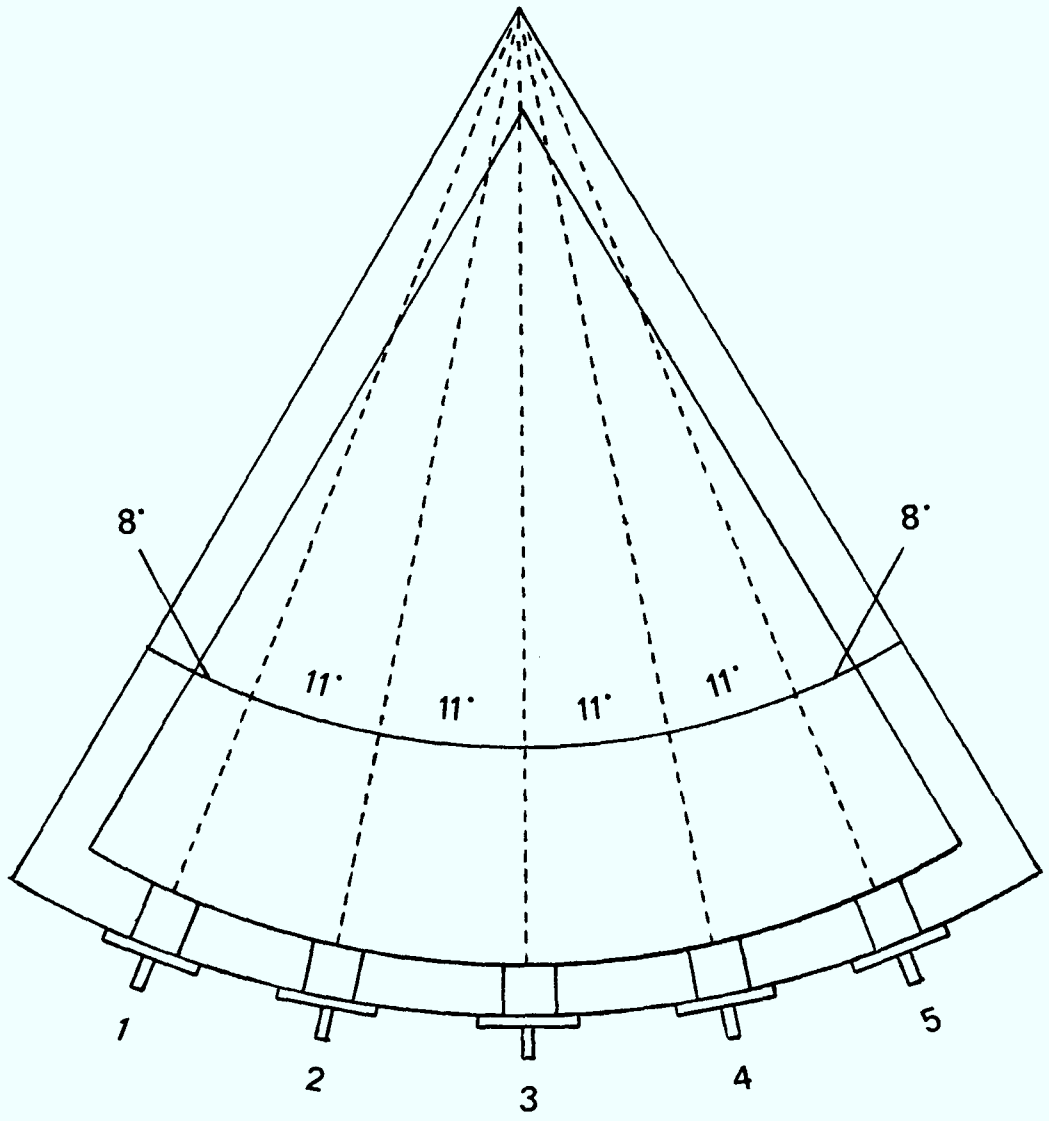

Figure 2.5: Tuyere positions

The data desired, for the air flow conditions, was temperature, operating pressure and flowrates. The pressure was measured by a standard pressure meter, which ranged from (-30)-(+30) inches H_g. The air stream temperature was measured by the use of thermocouples. Each thermocouple was constructed of Nickel-Chromium vs Nickel-Aluminum, (more commonly known as Chromel-Alumel). Two options were open as to how to treat the reference junctions:

i) they could be left at ambient temperature, thereby requiring the measurement of, and adjusting for, the laboratory temperature.

or ii) they could be fixed at 0°C by means of an ice bath.

It was not likely that there would be large fluctuations in the flow temperatures from room temperature. As a result, any errors in the measurement of ambient temperature would have a significant effect on the flow temperature result. The reference junctions, therefore, were fixed at 0°C by means of an ice bath, to eliminate the sensitivity of measurements to room temperature. The properties of the thermocouples used were: a temperature range of 0-1250°C and error limits of ± 2·2°C or ± 0·75%, whichever is greater. (The limits of error of the thermocouples were based on a reference junction temperature of 0°C and does not include use or installation errors). Before each series of experimental runs, all thermocouples were calibrated to 0°C. (All thermocouple readings were taken from a Hewlett Packard 3435A digital multimeter).

A method of measuring the gas flow rate was required, and in the absence of a flow meter, an alternative method was devised. It is understood that

$$\Delta p = \rho U^2 C \qquad (2.4)$$

where C is a weak function of flowrate and physical properties, and

$$U \propto \frac{\text{Standard flowrate}}{\text{Pressure}} \qquad (2.5)$$

and

$$\rho \propto \frac{\text{Pressure}}{\text{Temperature}} \qquad (2.6)$$

Therefore from the relationships of equations (2.4) to (2.6) it is clear that

$$\Delta pTp \propto (\text{Standard flowrate})^2 C \qquad (2.7)$$

Having measurements for the pressure and temperature leaves the requirement for a pressure gradient measurement so as to establish a correlation against the standard flowrate. An orifice meter was constructed from copper pipe and connected to a mercury U-tube manometer, and one was attached to each air line associated with an operating tuyere. These constructed meters were calibrated against known flowrates, thus providing the correlation of equation (2.7). The relationship between pressure gradient, temperature and absolute pressure vs standard flowrate is therefore given empirically, for each meter, and is shown in Figure (2.6).

2.2.3 Packed bed properties

The packed bed was simulated by dry ice pellets. The pellets were

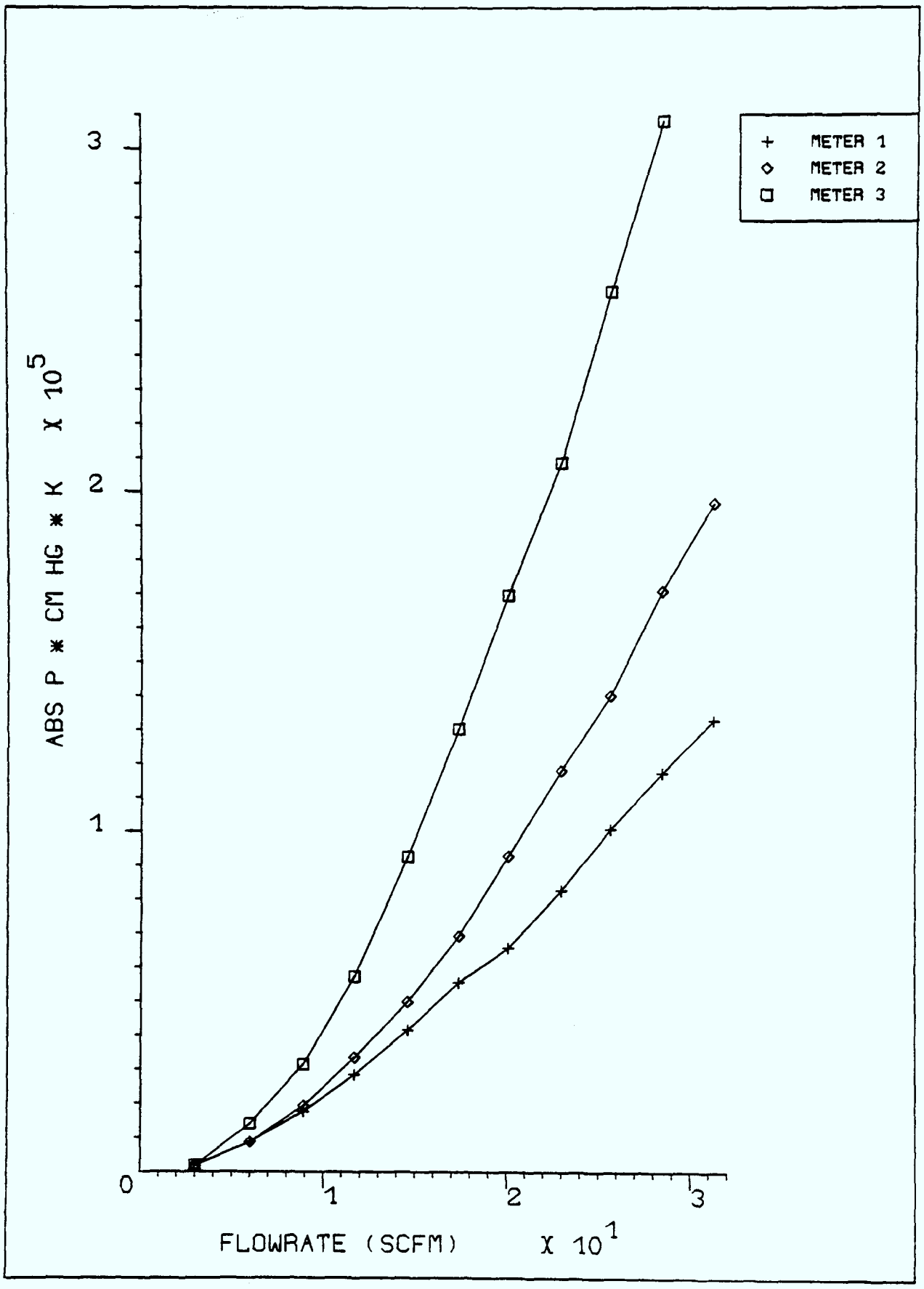

Figure 2.6: Empirical relationship for orifice meters

ordered in this form, as, in tests on crushing dry ice it was found that too many fines were produced and the uniformity of size was difficult to obtain. It was also observed that due to the long process of crushing, the ice started to sublimate if not kept refrigerated. The pellets were only available in a 1·25cm diameter size (½ inch), and on a size distribution analysis it was observed that the pellets were supplied within an acceptable tolerance. Their shape was 'coin like', where the thickness was approximately 0·5cm with a diameter as specified above. Analysis carried out on the voidage of the dry ice in the furnace provided a dry ice volume fraction of 0·7. Therefore in summary the packed bed has the properties of

particle diameter ≈ 1·25cm

dry ice density (true) = 1565 kg/m^3

dry ice volume fraction ≈ 0·7

bed porosity ≈ 0·3.

2.2.4 Data acquisition and running conditions

Results for the experiment were obtained via time lapse photography. A reference grid of 1cm×1cm cells was placed on the surface of the furnace to enable the calculation of raceway penetration and height. This grid was used for all the runs, except run nos.1,2 and 3 where a ½cm×½cm cell grid was used. The stills were taken every 15 seconds so as to analyse the time at which the raceway becomes steady state. An example of the results is given in Figure (2.7).

Due to logistics of compressed air cylinders, only two cylinders could be connected to each delivery line, and due to the high blast rates used, each run only lasted approximately 6-8 minutes. This

was ample time for the raceway to be formed, and it was believed enough time for steady state conditions to be obtained.

The initial runs were performed, blowing through tuyeres 1 and 2; and later on in experimental developments, through tuyeres 1, 3 and 5.

2.3 Furnace Redesign [Part II]

The initial experimental runs, blowing through tuyeres 1 and 2, did not form a raceway, despite previous expectations. It is believed that the cause for this is, the distribution of gas throughout the furnace has reduced the effective blast in front of tuyeres 1 and 2. Due to tuyeres 3,4 and 5 being shut off during the run, this allowed the gas to distribute in an azimuthal direction. A full account of the results is given in Chapter 3.

As a result of the experimental observations a redesign of the furnace was necessary. To prevent gas flow travelling in the azimuthal direction, in front of tuyeres 3,4 and 5, a partition was inserted between tuyeres 2 and 3. The redesign can be seen in Figure (2.8). Experimental runs were then resumed, still blowing through tuyeres 1 and 2.

2.4 Experimental Redesign [Part III]

Further experimental results introduced the problem of solids flow in the furnace. It is believed that this was caused by a combination of hanging and bridging, consequently the furnace was redesigned to introduce inclination of the circumferential wall. The acquisition of a Hastings flowmeter enabled the reconstruction of the air delivery system, giving better control of the flow to

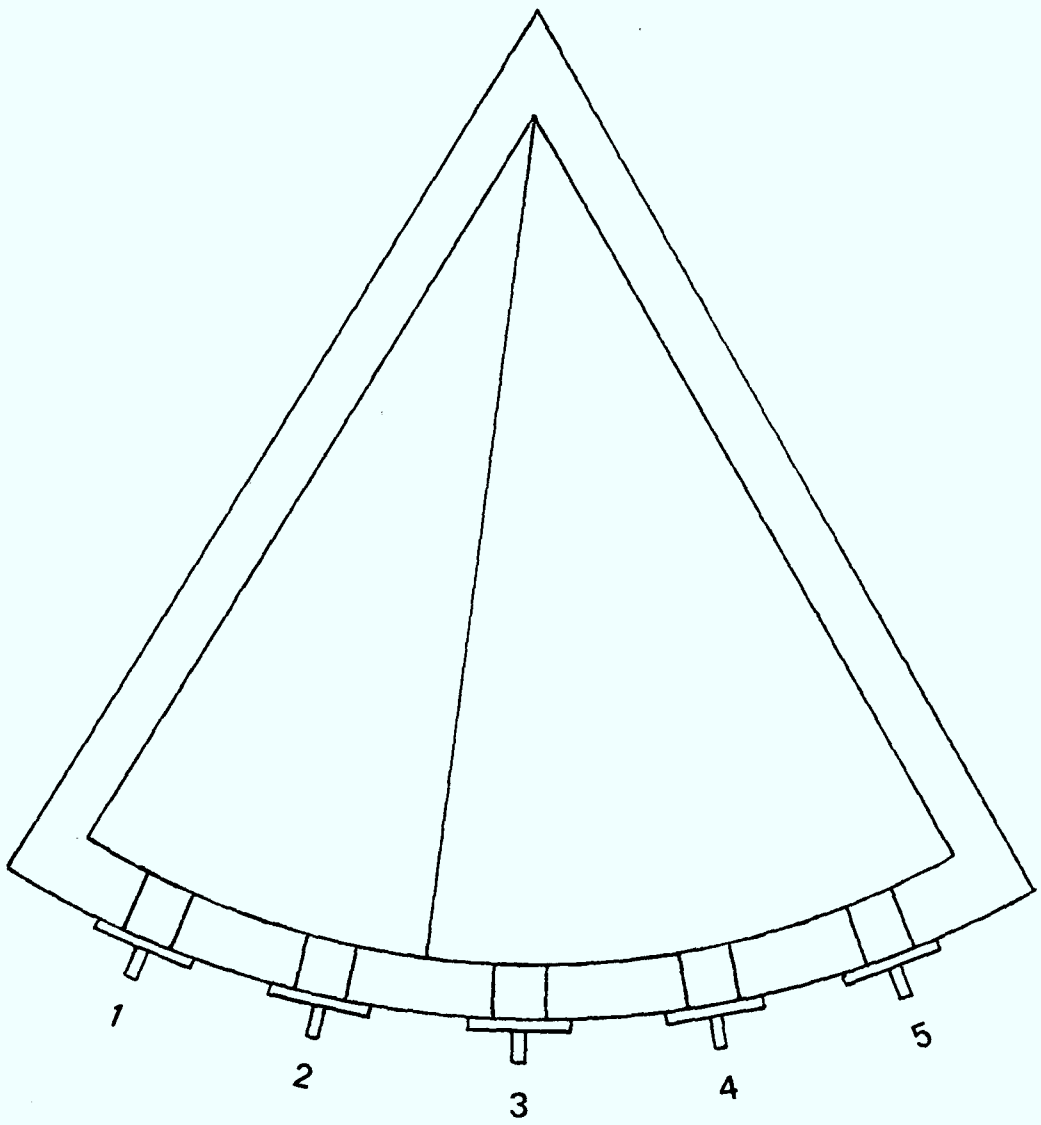

Figure 2.8: Addition of furnace partition

each tuyere. Figure (2.9) shows the new schematic diagram of the experimental system. The regulators used were also upgraded, enabling higher flowrates to be used, this then increasing the pressure in the system. As the previous pressure meter did not cope with these increases, the orifice meters were retained to calculate the absolute pressure.

2.4.1 Furnace redesign

The addition of an inclined surface on the circumferential wall posed a variety of problems. It would have been ideal to introduce a cone surface, and thereby simulate the furnace incline accurately, however this would have proved costly and time consuming to prepare. An alternative was the addition of three segments fitted at an incline. This would provide the wall angle required, and as a result the reduction of particle bridging, without lengthy design and construction work. The dimensions of the three segments to be added are shown in Figure (2.10). (The previously added partition was removed as the experiment now proceeded to blow through tuyeres 1,3 and 5). The dimensions of the furnace with inclined walls are shown in Figure (2.11). The wall angle achieved is approximately 9°, whereas full scale furnace inclination is at an angle of approximately 6·5°. The slight over estimation is not important as the reason for inclination is to try and eliminate the effects of particle bridging.

2.4.2 Air delivery redesign

The acquisition of a new Hastings flowmeter and Hastings channel flow monitor prompted the redesign of the air delivery system. As shown in the schematic diagram of Figure (2.9), the flowrates were measured on exit from the compressed air cylinders. The air

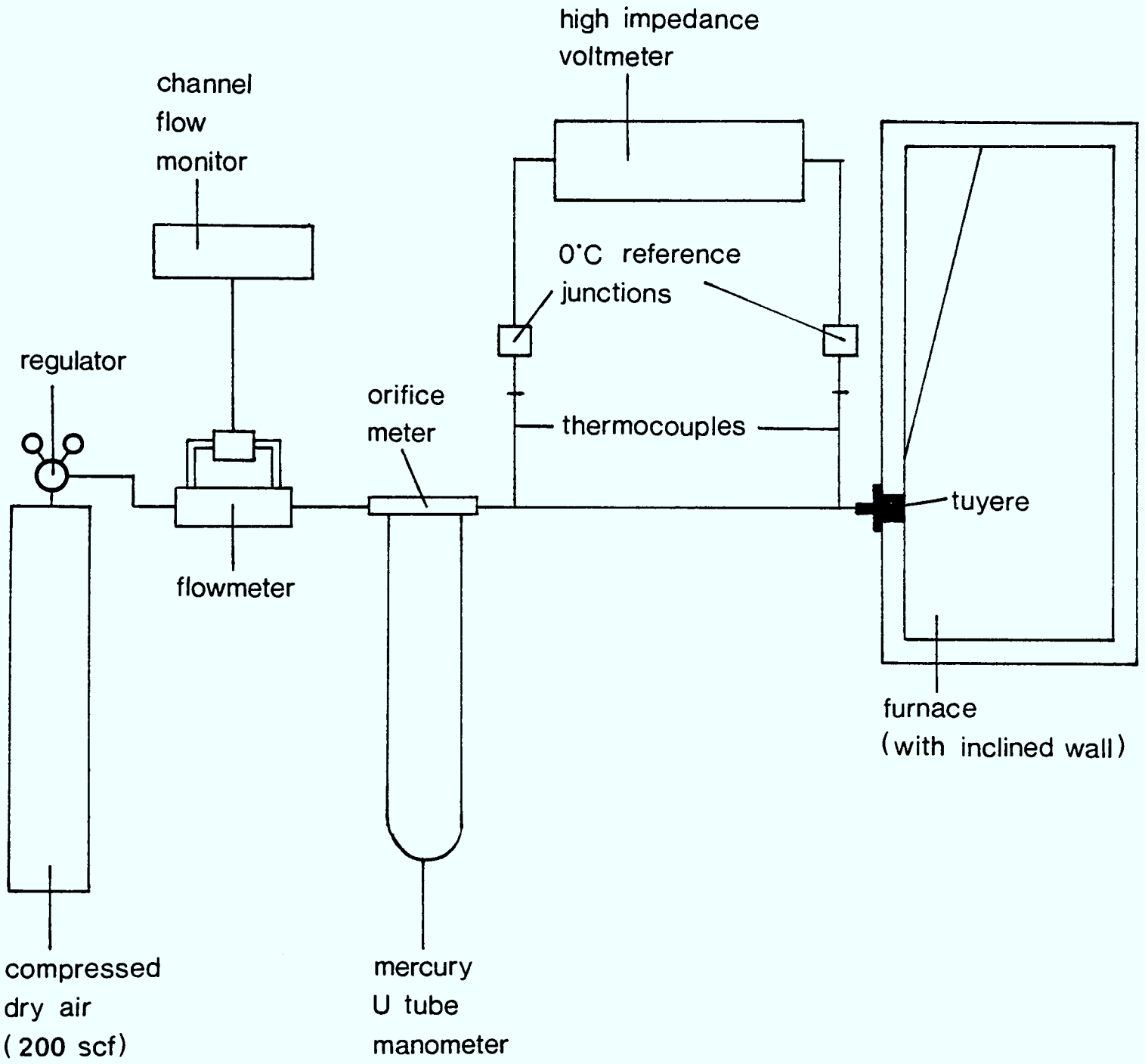

Figure 2.9: Schematic diagram of new experimental setup

not to scale

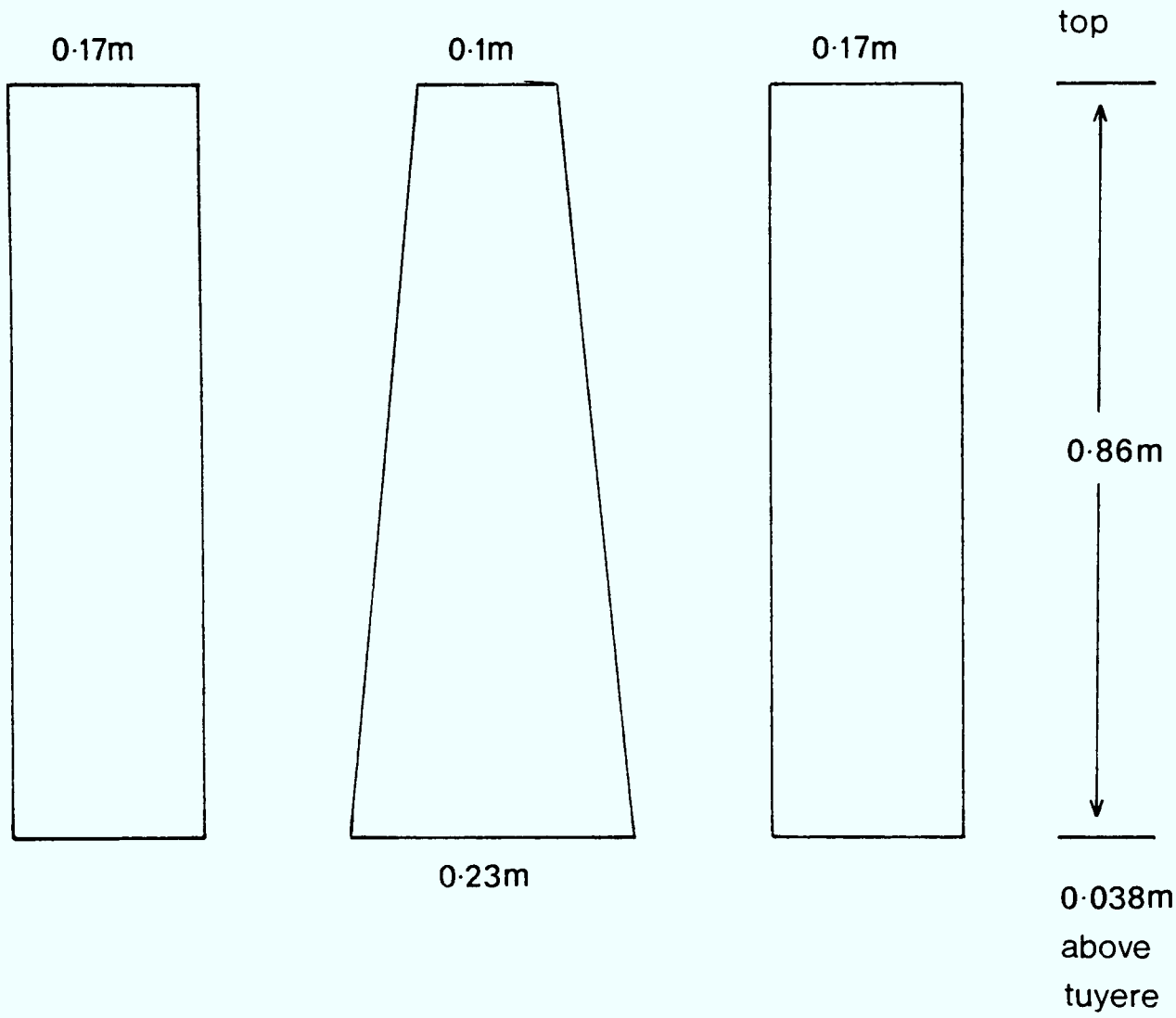

Figure 2.10: Dimensions of inclined wall segments

not to scale

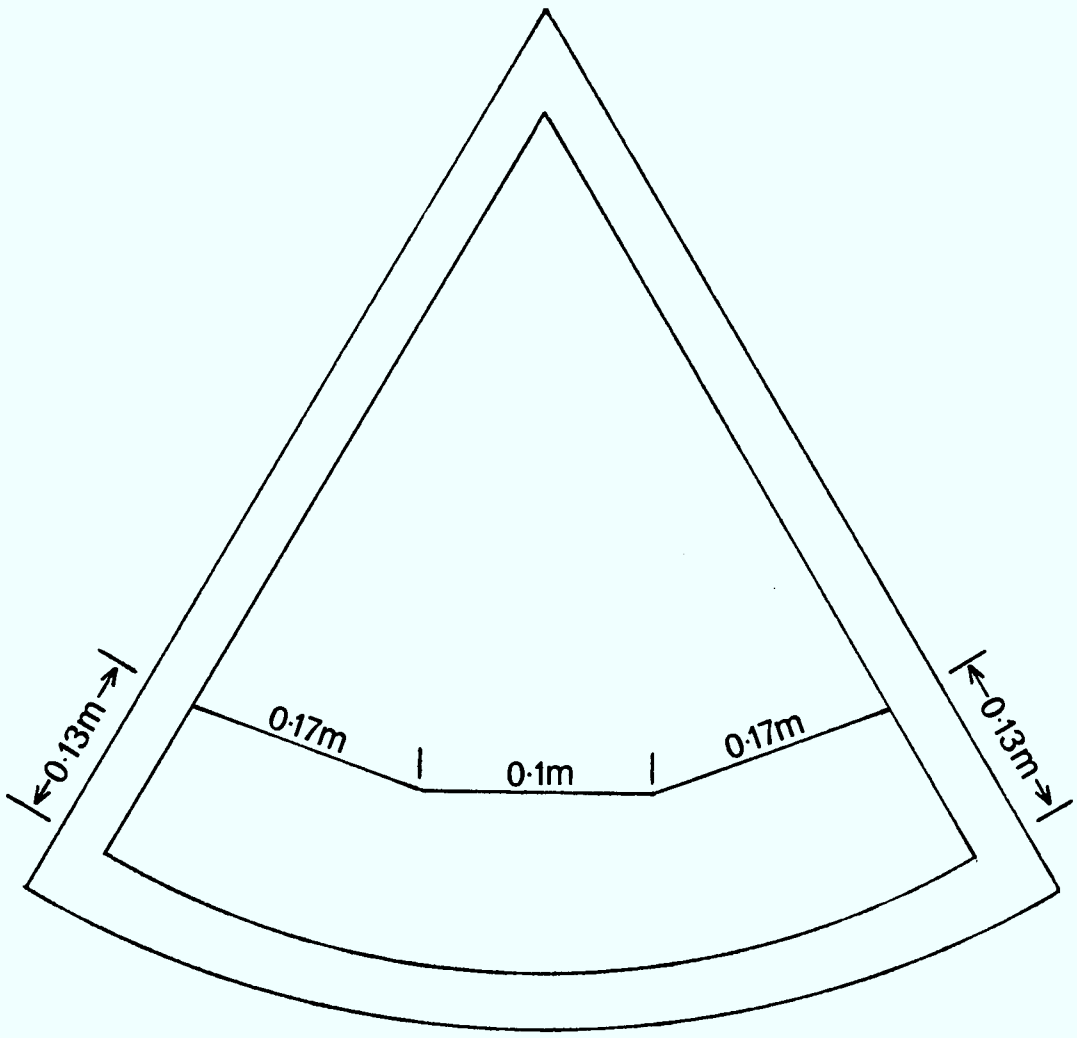

Figure 2.11: Additional dimensions of inclined wall furnace

temperature, as before, was measured by the use of Chromel-Alumel thermocouples placed immediately before the tuyeres and at the orifice meters.

The orifice meters from the previous design, were still used in the system but for a different purpose. The new system was designed to allow higher flowrates to each tuyere, by the upgrading of the cylinder regulators (from model 8 to 8H), and resultantly produced an increase in the line pressure. This increase exceeded the capabilities of the previous pressure meter giving rise to the need for an alternative method. The relationship of equation (2.7), together with the corresponding empirical relationships, still applied to the orifice meters, consequently these were used to calculate absolute pressures now that the flowrate was known.

2.4.3 Additional packed bed properties

From previous experimental runs, the problem still arose concerning the hanging and bridging of particles. Due to the angled walls eliminating the problem of wall friction, and the major contribution to bridging, it was believed that particle-particle interaction played a more significant role than previously assumed. As shown in the analysis of the dry ice, the volume fraction was calculated at approximately 0·7, it was therefore desired to reduce this and resultantly reduce the particle-particle interaction. A new media was introduced and mixed in with the dry ice at a volumetric ratio of 1:1. The second media was garbanzo beans, chosen for their shape, density and packing porosity.

The shape of the beans were near spherical and this helped in reducing the dry ice particle interaction when mixed in a volumetric

ratio of 1:1. The resultant bed porosity was increased slightly and the combined true density reduced. On observations of further runs, the combination of all these properties had the desired effect of enabling the packed bed to descend freely.

A summary of the analysis on the properties of the beans is given as:

bean diameter ≈ 1·0cm

bean density (true) ≈ 1346 kg/m^3

bean packing porosity ≈ 0·4.

2.4.4 Running conditions

The compressed air system remained as before, having two cylinders (200 scf) linked up to each delivery line. The flowrate capability was increased as a result of the upgrading of the regulators from Matheson model 8 to model 8H. The original model 8's could deliver the flow at a pressure of 60 psi (pounds per square inch) while the new model 8H's delivered a higher flowrate at a pressure of 100 psi. In actual fact, the maximum attainable flowate in the new system was less than that of the original. The reason for this was that the new air delivery system created a greater resistance to flow. As a result the regulators would have needed to deliver the flow at a higher pressure than they were capable of doing.

The runs were performed, while blowing through tuyeres 1,3 and 5.

2.5 Conclusion

An experimental technique has been designed for the analysis of raceway formation using dry ice, and later dry ice and inert particles, as the solids media. It became clear from

experimentation that the initial design needed various changes to accommodate the successful running of the simulation. Finally a good experimental method was developed for the analysis of raceway geometry and formation.

CHAPTER 3

EXPERIMENTAL RESULTS

3.1 Introduction

The results of the experimental raceway model are presented in this chapter, in the order each experiment was performed. Some results presented do not have operating conditions fully recorded due to the unexpected failure of equipment from time to time. It must also be noted that the data recorded is represented in a variety of units. This was due to the equipment being of different manufacturing origins. Despite the lack of standard units, there is no loss of clarity in the comparison of results.

3.2 Part I

The first run performed was in accordance with the experimental design of section 2.2. The tuyeres in operation were nos.1 and 2, while nos.3,4 and 5 were closed off. Dry ice pellets filled the furnace to a bed height of 0·81m (32in) and the air delivery operating condition are given in Table (3.1). Of the data given in Table (3.1), the temperature and pressure were obtained from direct measurement whereas the flowrates were calculated via an empirical relationship, as explained in section 2.2.2.

It is observed that the flowrates for each tuyere differ. The measurements of pressure and temperature both contain a certain percentage error together with the orifice manometer reading. As a result of these errors, it can be seen from the relationship of equation (2.7) that the combined error in obtaining the empirical relationship could be as much as 10%. As the flowrates were calculated from the pressures, temperatures and pressure gradients it was not possible to set the flowrate at a desired value, due to the short run times available. What was of more importance at this stage of experimentation was to observe the formation of a raceway.

	Tuyere 1	Tuyere 2
Diameter (m)	0·02	0·02
Flowrate (slpm)	920	850
Temperature (K)	265	268
Pressure (bar)	2·029	2·029

Table 3.1: Operating conditions for run 1.

With the above operating conditions run 1 was performed. It was observed that even with the small run times available, enough dry ice sublimated to be able to form a raceway of the largest predictable size. However, no distinct raceway did form, only a region of 'movement' was observed at the expected raceway position. The air flow appeared to be redirected; while most of the sublimation occurred above the tuyere, causing channelling, the lack of raceway penetration seemed to be caused by the air flowing towards the centre of the furnace, in front of tuyeres 3,4 and 5. (Note: at this point no photogaphic results were available).

These results prompted the immediate redesign of the furnace, as explained in section 2.3, so as to try and eliminate the circumferential flow of air.

3.3 Part II

This section is subdivided into two stages of experimentation. The first stage is the running of the experiment using the modified furnace, recommended by the results of section 3.2, and blowing through tuyeres 1 and 2 only. The second stage is the removal of the partition, thus returning to the original furnace construction, and blowing through tuyeres 1,3 and 5 only. The second stage also uses the modified air delivery system, as explained in section 2.4.2.

3.3.1 Partitioned furnace

Due to the results of run 1 (section 3.2), the furnace was modified by the addition of a partition between tuyeres 2 and 3. A diagram of the location of this fixture is given in Figure (2.8). The tuyeres in operation were, as before, nos.1 and 2, with nos.3,4 and

5 shut off. Three experiments were performed under these conditions and they will be identified as runs 2,3 and 4. For runs 2 and 3, the partition was inserted to fit as tightly as possible, however, the results showed air leakage along the partition edges. Therefore, run 4 was performed after the edges were sealed via rubber cement.

The operating conditions of run 2 are shown in Table (3.2), and the dry ice was loaded to a bed height of 0·81m (32in). The addition of the partition had the desired effect on the air flow. The air was predominantly channelled through the region required but it was still observed that the sublimation took place directly above the tuyeres. This implied that the blast velocity was not high enough to penetrate into the raceway region. Run 3 was then set up to account for this problem by using smaller tuyere diameters. The operating conditions are given in Table (3.3). The bed height in this case was only 0·66m due to a temporary delay in the dry ice supply.

It is observed in Table (3.3) that the flowrates and pressure are approximately the same for the previous runs, despite the use of a smaller tuyere diameter. The smaller diameter would have increased the pressure, but this expected increase was counteracted by a decrease in the required pressure gradient of the furnace due to a lower bed height. The observations of the raceway region showed that the increased blast velocity had caused a region of high recirculation, however the bubble formation above the tuyere position was still evident. A photograph of the observed region is shown in Figure (3.1); this records the region 6 mins after start up and therefore well into the formation of any raceway.

	Tuyere 1	Tuyere 2
Diameter (m)	0·02	0·02
Flowrate (slpm)	920	850
Temperature (K)	265	265
Pressure (bar)	2·029	2·029

Table 3.2: Operating conditions for run 2.

	Tuyere 1	Tuyere 2
Diameter (m)	0·01	0·01
Flowrate (slpm)	920	880
Temperature (K)	265	265
Pressure (bar)	2·029	2·029

Table 3.3: Operating conditions for run 3

The apparent channelling of air above the tuyere and the lack of formation of a definite raceway was still a problem. The furnace partition was fitted as tightly as possible though it was evident that leakage was occurring at various regions along the partition's edge. This problem of an insufficient seal was solved by using a rubber cement along the partition's edges.

Before the results to run 4 are discussed it must be pointed out, with reasons, why the flowrates could not be calculated. It was observed during, and on completion of, the run that both the thermocouples and orifice meters were not performing correctly. On closer inspection it was apparent that the thermocouples had to be rebuilt, a relatively fast task. However, the orifice meters' problem was not diagnosed until a later stage; it was believed that they had been altered and therefore the empirical relationships of Figure (2.6) no longer applied. (The experiment was built and operated in two separate periods, it is therefore conceivable that some accidental alteration took place between these periods). The recalibration of the orifice meters, to obtain an empirical correlation, would have been a lengthy process. With time constraints taken into consideration, it was decided that the meters were not absolutely necessary. Again, it must be stressed that the discovery and eventual decision was not made until many more experiments had been run. Thus, the new air delivery system, explained in section 2.4.2, contained the meters. Also, they were not considered important as the new system still enabled the measurement of flowrate and temperature.

Run 4 was then performed, with tuyere diameters of 0·01m and a packed bed height of 0·93m. The results of the run are given in

Figure (3.2). It can be seen from the photographs that the blast still penetrates into the raceway region. What is also observed, is the continued growth of the raceway height and depth as time progresses. From this it was concluded that channelling above the tuyere still occurred, and the packed bed appeared to have great difficulty in moving, particularly around the raceway region. The immobility of the packed bed had to be confirmed, and thus the next set of experiments were for this purpose.

3.3.2 Operating tuyeres 1,3,5

With the task of confirming the packed beds apparent immobility, four runs were perfomed (nos.5 to 8). Due to the acquisition of a flowmeter the air delivery system was redesigned, as laid down in section 2.4.2. As discussed in the previous section, the new air delivery system allowed for the measurement of flowrates and temperature thereby eliminating the necessity for the pressure measurement.

The results of run 4 showed the effect of the sealed partition in the furnace design confirming the need to reduce circumferential flow. With the new equipment it was more feasible now to achieve this aim by blowing through tuyeres 1,3 and 5. So runs 5 to 8 were performed with the original furnace design and the new delivery system.

For all the runs (nos.5 to 8) the bed height was maintained at 1·05m so as to preserve some form of reproducibility of the results. The operating conditions of runs 5 to 8 are given by Tables (3.4) to (3.7) respectively. It is observed in these operating conditions that for each run, the flowrates at each tuyere were similar. This

	Tuyere 1	Tuyere 2	Tuyere 3
Diameter (m)	0·01	0·01	0·01
Flowrate (slpm)	600	600	600
Temperature (K)	276	276	276

Table 3.4: Operating conditions for run 5.

	Tuyere 1	Tuyere 2	Tuyere 3
Diameter (m)	0·01	0·01	0·01
Flowrate (slpm)	500	500	500
Temperature (K)	278	278	278

Table 3.5: Operating conditions for run 6.

	Tuyere 1	Tuyere 2	Tuyere 3
Diameter (m)	0·01	0·01	0·01
Flowrate (slpm)	600	600	600
Temperature (K)	278	278	278

Table 3.6: Operating conditions for run 7.

	Tuyere 1	Tuyere 2	Tuyere 3
Diameter (m)	0·01	0·01	0·01
Flowrate (slpm)	600	600	600
Temperature (K)	281	281	281

Table 3.7: Operating conditions for run 8.

is possible due to the new flowmeter recording the flowrate in real time, and not requiring a calculation as before. As a result, the temperatures at each tuyere were the same. It should be pointed out however, that while the rates of these variables are recorded as identical, measurement error and round off of data is present. Run 6 was executed with a lower flowrate so as to try and record a basic change from run 5, while runs 7 and 8 were designed to reproduce 5.

The results of the runs are shown in Figures (3.3) to (3.5). As will be explained later, runs 7 and 8 gave very similar results and therefore it is unnecessary to show the photographs of run 8.

As can be seen in Figure (3.3), the blast velocity is high enough for effective raceway penetration. As the run progressed, the raceway size continued to enlarge in both the depth and height measurements, implying that not enough ice particles were flowing in. The flowrate was reduced for run 6, and as shown in Figure (3.4) less penetration occurred, as expected. It is also observed that the raceway grew faster in the vertical direction, which may have been caused by a build up of fines. Although for each new run the furnace was topped up with ice and the raceways forced to collapse, the fines built up from the previous run, still remained in the raceway vicinity. In this case, the resistance to flow at the farthest end of the raceway would be greater than at the raceway roof, thus directing flow in an upward manner. Run 7 then increased the flowrate, and it would have been expected to see a deeper penetration. As illustrated by the results of Figure (3.5) this was not the case. The depth of raceway was slightly less than for the previous run of lower flowrate. This strengthened the belief of the fines building up, and thereby playing a major role in penetration

distance. The rapid and continuous growth in the vertical direction also confirms the stationary behaviour of the dry ice packed bed. The results of run 8, designed to simulate the previous, showed a slightly greater penetration; more importantly, the same rapid vertical growth was observed strengthening the beliefs of the particulate behaviour.

From this set of experiments it was believed that the packed beds' reluctance to flow was caused by hanging and bridging of particles. To alleviate this problem a new furnace design was needed which reduced the wall friction effect. This was achieved, as explained in section 2.4.1, by the introduction of an inclined wall on the circumferential section. The next section deals with the experiments performed with the modified furnace.

3.4 Part III

Four experiments were performed with the 'inclined wall furnace' to demonstrate the important role of particle-particle interaction. Two stages to the analysis took place. Firstly, the experiments used the standard dry ice packed bed, demonstrating the persistence of the problem; secondly, a new media was added to the dry ice bed to highlight the effect of particulate interaction.

With all the following runs, the new air delivery system was still in operation.

3.4.1 Inclined furnace wall

The previous four runs (nos.5 to 8) succeeded in confirming a problem with the mobility of the dry ice packed bed. It was concluded that the requirement of an inclined wall existed. This

was achieved by the construction set down in section 2.4.1, whereby the circumferential surface was modified to include wall inclination.

The operating conditions of runs 9 and 10 are given in Tables (3.8) and (3.9) respectively. The packed bed, being dry ice particles only, was filled to a height of 1·1m for run 9 and 0·85m for run 10. For both runs, the raceway growth was observed to be continuous; this is illustrated by the photographic results in Figures (3.6) and (3.7). The penetration of blast in run 10 was slightly less effective than for run 11, though the vertical growth was more effective. This slight variation was clearly caused by the condition of the particles in the raceway region before each run; they would obviously be different due to the production of fines. It should also be pointed out that the packed bed heights for the experiments were not identical.

So far, the packed bed has failed to flow into the raceway region as desired. The previous runs, performed in the old furnace construction, showed the need to eliminate factors causing hanging and bridging. From these conclusions it was believed that wall inclination would be the solution to the problem of packed bed immobility, and therefore such a furnace was constructed. However, the previous two runs (nos,9 and 10) have shown the problems' continued existence. It was thus believed that the dry ice particle shape was a more dominant factor than previously believed. Due to their thick 'coin like' shape it was clear that a form of 'particle interlocking' was taking place. The need, therefore, to separate particles by the addition of another, more spherical particle, became apparent.

	Tuyere 1	Tuyere 2	Tuyere 3
Diameter (m)	0·01	0·01	0·01
Flowrate (splm)	600	600	600
Temperature (K)	278	278	278

Table 3.8: Operating conditions for run 9.

	Tuyere 1	Tuyere 2	Tuyere 3
Diameter (m)	0·01	0·01	0·01
Flowrate (splm)	600	600	600
Temperature (K)	270	270	270

Table 3.9: Operating conditions for run 10.

3.4.2 Addition of secondary particles

The media chosen to mix with the dry ice was garbanzo beans, the properties of which are given in section 2.4.3. The beans were mixed with the dry ice, in a volumetric ratio of 1:1, while loading both media into the furnace. Such a high volumetric ratio was used so as to ensure the desired effect of separation occurred. This ratio was not calculated analytically but decided upon as a result of the experience gained working with the dry ice.

The operating conditions for run 11 are given in Table (3.10), and the packed bed of mixed particles was loaded to a height of 0·85m. Due to the beans not having a sublimation property (ie. the beans being inert) the blast momentum needed to be higher than before so as to push back the beans media from the raceway region. This was necessary as particles flowing into the raceway would not all sublimate and therefore the raceway could conceivably fill up with beans. There was no complete raceway observed, as a result no photographic results are presented for run 11. There was, however, a region of high activity which could be described as the recirculation effects in front of the tuyere positions.

As 700slpm (standard litres per minute) was the maximum attainable flowrate for this system set up, it was decided to increase the blast velocity further by using a smaller tuyere diameter. The operating conditions for run 12 are given in Table (3.11), and the packed bed was loaded to a height of 0·75m. Note that in the operating conditions of run 12 the flowrate was set to 640slpm. This was not an arbitrary choice but the maximum attainable rate for the size of tuyere used. As mentioned before (section 2.4.2) due to the air delivery redesign, the line resistance changed thereby

	Tuyere 1	Tuyere 2	Tuyere 2
Diameter (m)	0·01	0·01	0·01
Flowrate (slpm)	700	700	700
Temperature (K)	278	278	278

Table 3.10: Operating conditions for run 11.

	Tuyere 1	Tuyere 2	Tuyere 3
Diameter (m)	0·005	0·005	0·005
Flowrate (slpm)	640	640	640
Temperature (K)	283	283	283

Table 3.11: Operating conditions for run 12.

limiting the delivery rate, due to the model of regulators used. As the results of Figure (3.8) show, the increased blast velocity had the desired effect. From the photos, two spherical regions can be identified, one inside the other. The darker, internal sphere, was the raceway void, which consisted of very loosely packed beans recirculating very rapidly. The lighter and larger sphere appeared to be a slower recirculating region of crushed beans. As this was on the face of the furnace wall, it was more than likely that the true raceway extended further than the observed darker region. The view of the total raceway was therefore obscured by the slower moving region. On observing the results further, it is clear that the raceway size becomes steady, and therefore showing that the packed bed is flowing into the raceway region. This was confirmed on stopping the experiment, as the raceway collapsed unaided.

The strong effect of dry ice particle interaction, for the particular shape used, was therefore confirmed and a successful method for overcoming this problem found.

3.5 Conclusion

The performance of the experimental raceway runs showed a number of factors which affect the raceway region and packed bed behaviour. The effect of circumferential flow was highlighted by experiments 1 to 3, showing the important effect of adjacent raceways. A factor thought to have been significant in raceway formation was that of fines, and particle properties in general, in the region concerned; though this was judged on observations of a limited number of experiments. A more detailed analysis of this factor would need to take place to be able to make a more reliable statement. The hanging and bridging of particles was brought to light, though again

this was not analysed fully enough.

An overall conclusion of the experimental results is that a new experimental technique for the analysis of raceway geometry has been developed, and on initial runs proved successful.

CHAPTER 4

MATHEMATICAL MODEL

4.1 Introduction

It is clear that if a blast furnace model is going to adequately represent the process it must account for the prediction of the gas flow distribution. As seen, in more detail, in section 1.3, Stanek, Szekely and co-workers developed a generalised Ergun equation to describe flow through blast furnace stack structures. While, Yagi et al pursued the development of models which account for the gas flow distribution, using a finite element method to account for interphase heat transfer. An important fact to notice is that the cohesive zone must be specified. Cross et al (1984) developed an inert model of multilayered ore/coke furnace structure which predicts the cohesive zone shape as a function of process operating conditions. This model makes assumptions about the solids flow and utilises a pressure-stream-function based finite difference formulation, and specifies the vertical descent pattern of the solids.

The present contribution is derived from fluid dynamics theory, and is concerned with a control volume based finite difference formulation of gas and solids flow through the furnace with inert interphase heat exchange. The solids are assumed to move with potential flow and the cohesive zone shape and location are predicted as a function of solids temperature.

4.2 Problem Considered and Governing Equations

The basic features and flow conditions of the iron blast furnace are outlined in Figure (4.1). The domain considered is a furnace construction, on a polar cylindrical coordinate system, containing a solids packed bed and gaseous media. Assumptions made about the characteristics of the solids media are as follows: the particles

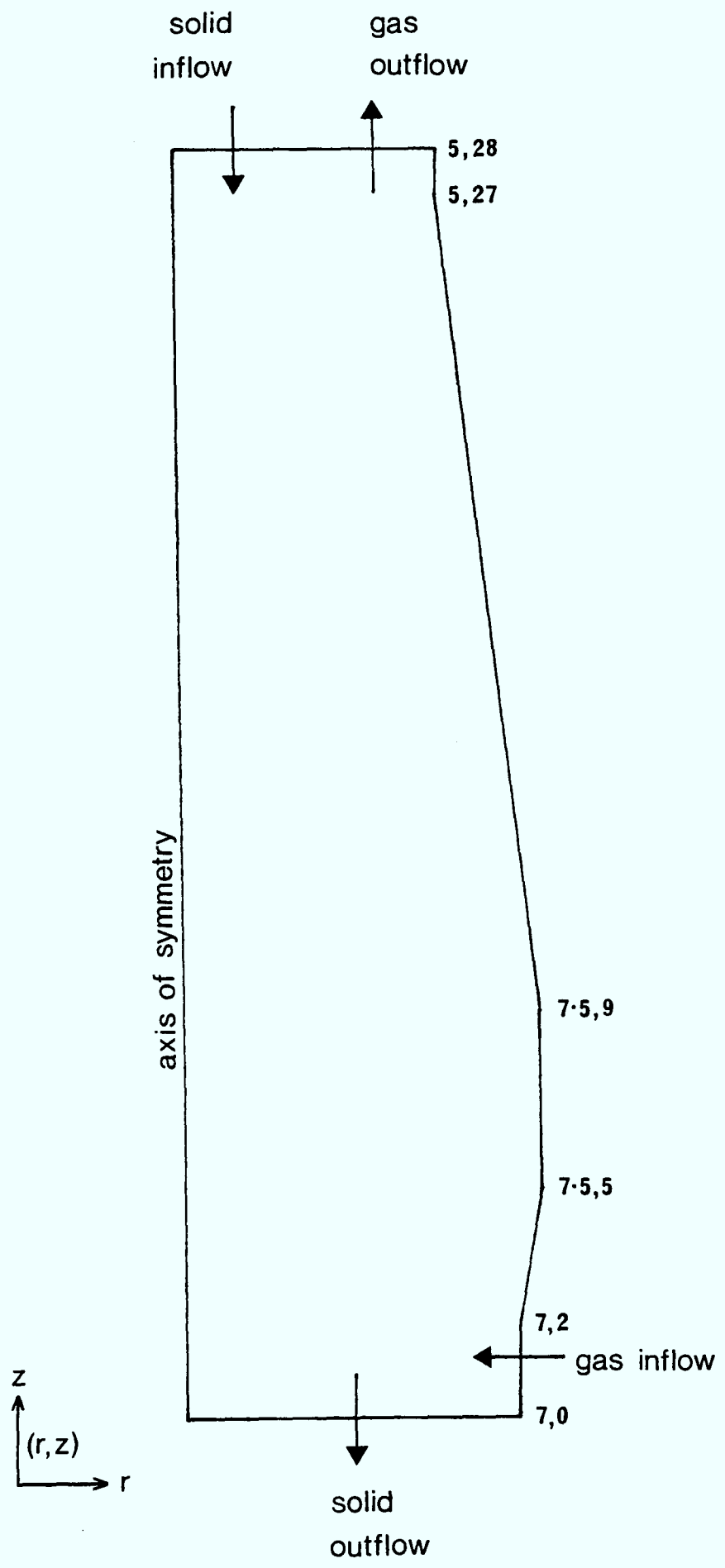

Figure 4.1: Basic features of iron blast furnace

are assumed to be of uniform shape factor for the calculation of the frictional resistances, this factor being determined via observations; particulate shape factor is assumed spherical in the determination of the energy transfer between phases; and, the particles are assumed isothermal. The gas phase is air, as in the physical problem; and, the components of the solids phase are assumed to be coke and ore, the predominant materials in the packed bed.

The incoming air jet distributes as it enters the furnace, providing the energy required to heat the solids phase. The incoming particles on absorbing energy, change their ore to coke proportions, as the ore phase softens and melts, and eventually become predominantly coke. These varying phases of ore to coke proportions (stack, cohesive and active zones) create varying resistance to the gas flow and resultantly affect the pressure gradients both radially and axially.

The two-phase flow phenomena is steady, requiring multi-phase gas-dynamic equations together with the utilisation of empirical relations associated with interphase frictional resistance and heat transfer.

4.2.1 Dependent and Independent variables

The dependent variables of the model are; the radial and axial velocities for the gas and solids phase, V_g, W_g, V_s and W_s; the pressure p; the gas solid volume fractions, r_g and r_s; and the enthalpies of the gas and solids, h_g and h_s.

The independent variables are the radial and axial distances, r and

z, in a polar cylindrical coordinate system.

4.2.2 Mass conservation

The volume fraction, density and velocities for the gas phase must, in order to satisfy the mass conservation principle, obey the following equation:

$$\mathrm{div}(r_g \rho_g \underline{V}_g) = 0 \qquad (4.1)$$

and for the volume fractions, r_g and r_s are related via the 'space sharing' equation,

$$r_g + r_s = 1. \qquad (4.2)$$

The volume fraction for the solids, r_s, is evaluated according to the voidage that the solids mass make at various levels in the furnace. The volume fraction for the gas, r_g, therefore always satisfies the equation (4.2).

4.2.3 Conservation of momentum

The conservation of momemtum for the gas phase is given by:

$$\mathrm{div}(r_g \rho_g \underline{V}_g \Phi) = \mathrm{div}(\mu_g r_g \ \mathrm{grad}\ \Phi) - \underline{i}\,\mathrm{gradp} + S_\Phi \qquad (4.3)$$

where

$$S_\Phi = \underline{i} \rho_g \ \underline{a}_{grav} - F_g \underline{i}(\underline{V}_g - \underline{V}_s) \qquad (4.4)$$

and Φ stands for the radial and axial gas velocities, V_g and W_g. The pressure gradient term, in equation (4.3), and the terms of the source, S_Φ, equation (4.4), are multiplied by the vector $\underline{i}$,

where $\underline{i}$ is a direction vector. The first term in the source equation is the gravitational force and the second an interphase friction term, where F_g is a friction factor.

The interface friction term takes account of the directional resistances in an anisotropic packed bed. The Ergun equation to describe the pressure drop across a porous layer, Ergun (1952), is given by

$$-\frac{\Delta p}{L_b} = \frac{150(1-\epsilon)^2}{\epsilon^2(\bar{\Phi}_s d_p)^2}\mu_g \bar{V}_g + \frac{1.75(1-\epsilon)}{\epsilon(\bar{\Phi}_s d_p)}\rho_g \bar{V}_g^2 \qquad (4.5)$$

where the first term represents viscous resistance and the second inertial resistance to flow. The form shown in equation (4.5) differs slightly from Erguns original representation. Originally, the viscous and inertial resistance terms had ϵ^3 terms, instead of ϵ^2 and ϵ respectively. This representational difference occurs as equation (4.5) is using actual velocities as opposed to Erguns original correlation using superficial velocities. The actual average velocity of the gas in the bed is obtained from the ratio of the superficial gas velocity, $\bar{U}_g$, to the fractional voids, $\bar{V}_g = \bar{U}_g/\epsilon$.

Generalising equation (4.5) to vectorial form to describe the gas flow through isotropic porous media, Stanek and Szekely (1974), gives

$$-\nabla p = (f_1 + f_2|\underline{V}_g|)\underline{V}_g \qquad (4.6)$$

where f_1 and f_2 represent the viscous and inertial resistances. This vectorial form was developed further to take into account

multi-layered structures, classified as a single equivalent anisotropic region, and the inclination of such structures by Cross and Gibson (1979). The gas flow in an iron blast furnace has a high enough Reynolds number to render viscous resistance negligible, leaving a modified form of the Ergun equation for anisotropic regions, ie.

$$- \nabla p = |\underline{V}_g| (f_x V_g, f_y W_g) \qquad (4.7)$$

where the directional resistances account for the individual layer resistances and their relative thickness, ie.

$$f_x = F_1 F_2 / \{\alpha \sqrt{F_2} + (1-\alpha) \sqrt{F_1}\}^2 \qquad (4.8)$$

$$f_y = F_1 \alpha + F_2 (1-\alpha). \qquad (4.9)$$

Cross and Gibson, on taking into account the inclination of the multilayered structure, developed the form,

$$|\underline{V}_g| \; \underline{\underline{H}} \; \underline{V}_g = - \nabla p \qquad (4.10)$$

where $\underline{\underline{H}}$ is the matrix,

$$\underline{\underline{H}} = \begin{bmatrix} (f_x \cos^2\theta + f_y \sin^2\theta) & (f_x - f_y)\cos\theta\sin\theta \\ (f_x - f_y)\cos\theta\sin\theta & (f_x \sin^2\theta + f_y \cos^2\theta) \end{bmatrix} \qquad (4.11)$$

and θ is the angle of inclination.

As the equation (4.10) describes the inertial resistance to flow, it may be represented in a form to account for two phase flow, and thus

an interphase friction term. Therefore extending equation (4.10) leads to

$$- \nabla p = F_g(\underline{V}_g - \underline{V}_s) \tag{4.12}$$

where F_g is the interphase friction term,

$$F_g = |\underline{V}_g - \underline{V}_s|\underline{\underline{H}} \tag{4.13}$$

The solids flow patterns are obtained by solving the equations of potential flow, assuming the fluid is ideal (ρ_s = constant, $\mu_s = 0$) and the flow is irrotational. The latter assumption yields

$$\nabla x \underline{V}_s = 0. \tag{4.14}$$

The solid velocity components in the radial and axial directions, V_s and . W_s respectively, can be represented in terms of a stream function, where

$$V_s = \frac{1}{r}\frac{\partial \Psi}{\partial z} \tag{4.15}$$

and

$$W_s = - \frac{1}{r}\frac{\partial \Psi}{\partial r} \tag{4.16}$$

The model is considered in the two dimensional plane rz, thus equation (4.14) is the coefficient of the vorticity vector, perpendicular to that plane, giving

$$\frac{\partial V_s}{\partial z} - \frac{\partial W_s}{\partial r} = 0 \tag{4.17}$$

Substituting the velocity components by their stream function relationships, equations (4.15) and (4.16), equation (4.17) becomes

$$\frac{\partial}{\partial r}\left[\frac{1}{r}\frac{\partial \Psi}{\partial r}\right] + \frac{1}{r}\frac{\partial^2 \Psi}{\partial z^2} = 0. \qquad (4.18)$$

4.2.4 Conservation of energy

The conservation of energy is derived from the first law of thermodynamics applied to a fluid passing through an infinitesimal, fixed control volume, yielding for the gas phase

$$\text{div}(r_g \rho_g \underline{V}_g h_g) = \text{div}\left(r_g \frac{k_g}{c_g} \text{ grad } h_g\right) - h\bar{A}_s(T_g - T_s) \qquad (4.19)$$

and the solid phase

$$\text{div}(r_s \rho_s \underline{V}_s h_s) = \text{div}\left(r_s \frac{k_s}{c_s} \text{ grad } h_s\right) + h\bar{A}_s(T_g - T_s). \qquad (4.20)$$

The assumptions are that: h_g and h_s are the thermodynamic enthalpies of the gas and solid phase respectively, by which is meant the exclusion of the kinetic and potential energy of the phases; and, the energy equations exclude the work done on the control volume by the body and surface forces (these being ignored in the momentum equations).

The last term on the right hand side of equations (4.19) and (4.20) is a source term to prescribe the rate of heat transfer from one phase to another. The heat transfer coefficient is given by h, and $\bar{A}_s$ is the total surface area of the solids phase per unit volume, calculated as follows: consider N particles in a volume

V, then the solids volume fraction is defined as

$$r_s = N(\text{particle volume})/V. \tag{4.21}$$

Assuming the particles are spherical and of uniform size, radius r_p, then the surface area of the particles per unit volume is given by

$$\bar{A}_s = N(4\pi r_p^2)/V. \tag{4.22}$$

On substituting equation (4.21) into equation (4.22) the surface area per unit volume is given by

$$\bar{A}_s = \frac{3\ r_s}{r_p} \tag{4.23}$$

4.3 Auxiliary Relations

The above set of differential equations has to be solved in conjunction with observance of constraints on the values of the variables. The following auxiliary models look at aspects concerned with the formation of the packed bed; these being the structure and location of the various zones and the charge patterns of the coke and ore.

4.3.1 Zones

Due to the work by Cross and Gibson in enabling the properties of the different layers of solids to influence the directional resistances applied to the interphase friction term in equation (4.4), models determining the zones can be implemented. The properties of the ore:coke layers in the model are broken down into

three zones which are determined by the temperature of the solids phase. These are the Stack, Cohesive and Active coke zones, determined by the following temperature relationships.

a) Stack zone $T_S < 1200$ (K)

b) Cohesive zone $1200 \leqslant T_S \leqslant 1400$ (K)

c) Active coke zone $T_S > 1400$ (K).

On identifying the zones, the properties of effective particle diameter and bed voidage of the coke and ore are set, as laid down in Table (4.1). These properties are used in the calculation of the individual layer inertial resistances, F_1 and F_2. In the blast furnace the active coke zone is predominantly filled with coke and has a very low proportion of molten ore dripping through. As a result, the properties of ore, in the active coke zone, are set to those of coke in the same zone, thus having the effect of setting the model's active zone to an isotropic region of coke (see Table (4.1)).

4.3.2 Cohesive zone mushy region

During the solution of the mathematical model convergence instability was observed due to the high resistance gradients between the active coke and cohesive zones, and between the cohesive and stack zones. A model was introduced to reduce this gradient by the implementation of averages of the properties of coke and ore, ie. voidage and effective particle diameter, in the vicinity of the high gradients.

Figure (4.2a) shows a general mesh in the circumferential plane where various example cases are demonstrated. In cases A and B the

Zone	Material	Voidage	Effective particle diameter(m)
Stack	ore	0.3	0.009
	coke	0.5	0.05
Cohesive	ore	0.1	0.009
	coke	0.5	0.05
Active	ore	0.5	0.04
	coke	0.5	0.04

Table 4.1: Particle proportion

(a)

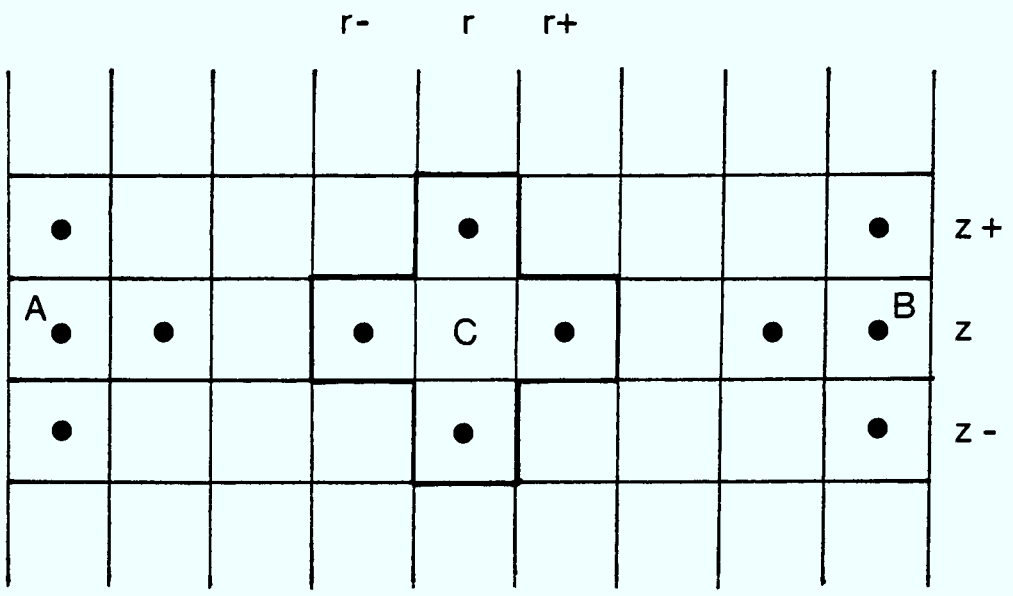

(b)

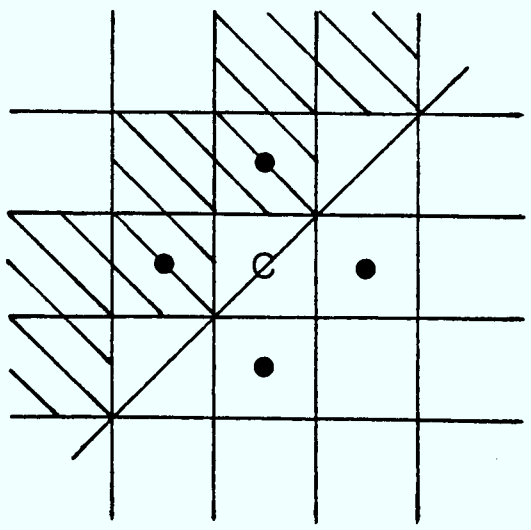

Figure 4.2: Cohesive zone mushy region implementation

model is concerned with the mushy region being implemented at the cell boundaries. The properties at the cell are the averages of the properties above, below, adjacent and the original properties at the point considered. In case C, where the cell considered is within the boundaries, the average is taken of the adjacent four cell properties. In case C the centrally located values of the properties are not implemented in the averaging so as to simulate a line boundary across all centres. By excluding the C location cell properties the new properties will simulate a cell filled with half of each of the zones, as shown in Figure (4.2b).

The new calculated values of voidage and particle diameter for the coke and ore layers are not preserved throughout the solution but only used in the immediate calculation of the individual layer resistances, F_1 and F_2.

4.3.3 Enthalpy - Temperature relationship

In the interphase heat transfer source terms of the energy equations (4.19) and (4.20), the temperatures T_g and T_s are related to the thermodynamic enthalpies h_g and h_s by the following relationships:

$$h_g = c_g T_g \qquad \forall T_g \qquad (4.24)$$

and

$$h_s = \begin{cases} c_s T_s & T_s < T_\ell \qquad (4.25) \\ c_s T_s + \dfrac{(T_s - T_\ell)}{(T_u - T_\ell)} . m_o . L & T_\ell \leqslant T_s \leqslant T_u \qquad (4.26) \\ c_s T_s + m_o . L & T_s > T_u \qquad (4.27) \end{cases}$$

where T_u and T_ℓ are the upper and lower temperatures defining the cohesive zone boundaries and L is the latent heat of melting of ore. The ore mass fraction is given by m_o, such that

$$m_o = \frac{(1-\alpha)\rho_o}{\rho_s} \qquad (4.28)$$

where α is the coke volume fraction and $(1-\alpha)$ the ore volume fraction.

4.3.4 Charge patterns

As well as setting the zones and the corresponding properties of coke and ore, the actual ore:coke ratio is prescribed as shown in Figure (4.3). At the centre of the furnace, along the radial direction, it is assumed there is no ore, whereas on moving towards the furnace boundary the ore:coke ratio increases. Along the radial direction, at any axial location, the total volume ratio of ore:coke is 1:1.

In general, the setting of the properties in various zones and the ore:coke ratio are implemented to assist in the accurate calculation of: the directional resistances f_x and f_y; the interphase heat transfer source term when calculating an average effective particle diameter; and, the calculation of the ore mass fraction, thus determining the relationships between the temperature and thermodynamic enthalpy of the solids phase.

The gas and solids volume fractions, r_g and r_s, do not change from their prescribed values to accommodate for the above mentioned auxiliary models.

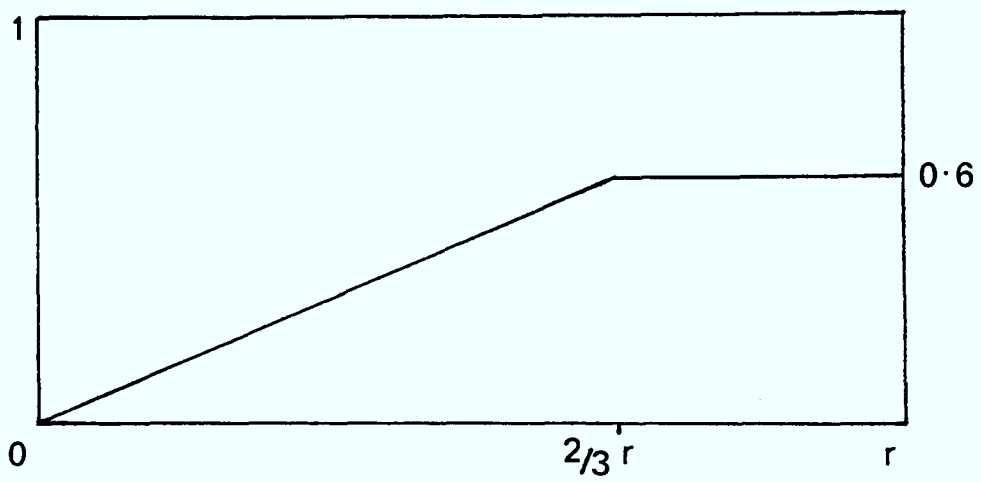

Figure 4.3: Ore:coke ratio along radial distance

4.3.5 Equation of state

The equation of state for the gas phase is dependent on the temperature and pressure, as prescribed by the ideal gas law.

$$\rho_g = \frac{p\ M_A}{R_o T_g} \qquad (4.29)$$

where M_A is the molecular weight of the gas, air, and R_o is the molar (universal) gas constant.

The equation of state for the solid particles is independent of the direct effects of temperature and pressure, and is stated as

$$\rho_s = (1-\alpha)\rho_o + \alpha\rho_c . \qquad (4.30)$$

For the purpose of the potential flow of the solids the density is assumed constant, and obtained via an average of the loading rates of the various particles, as set down in Table (4.2).

However, when dealing with the energy equations (4.19) and (4.20), the thermodynamic enthalpy of the solids phase is related to the temperature via equations (4.25), (4.26) and (4.27) which show a dependence on the ore mass fraction m_o and the latent heat of melting L. It is required that the equation for the solids density, (4.30), is used in the calculation of the ore mass fraction, equation (4.28), so as to ensure

$$0 < m_o < 1 \quad , \qquad \forall \alpha \in [0,1].$$

The use of a constant solids density in the definition of the solids

	Rate (kg/THM)	Bulk Density (kg/m^3)
Coke	503.4	550.0
Sinter (ore)	1152.7	1850.0
Pellets (ore)	443.4	2220.0

Table 4.2: Standard case loading rates.

potential flow is an approximation, but due to the solids relatively slow flow the efffects of this on the solids flow field is negligible.

4.3.6 Boundary conditions

In the above model, an axis of symmetry is assumed, at $r=0$, defined as

$$\frac{\partial \Phi}{\partial r} = 0. \qquad (4.31)$$

Where, Φ is the dependent variable representing the axial and radial velocity components of the gas phase and the enthalpy of both gas and solid phase. The gas inlet conditions are defined in the region of the tuyere, specifying a mass flow rate as

$$\left.\begin{aligned} &\frac{\partial}{\partial r}\,(r_g \rho_g \underline{V}_g) = \beta \\ &\frac{\partial^2 V_g}{\partial r^2} = 0 \\ &\frac{\partial^2 h_g}{\partial r^2} = 0 \\ &V_g = -\beta/\rho_g \quad ; \quad W_g = 0 \quad ; \quad h_g = c_g T_g^{in} \end{aligned}\right\} \qquad (4.32)$$

setting the boundary condition to a mass flow via convection only, ie. assuming zero diffusion.

The mass outflow condition for the gas is specified in connection with the external pressure, and sets the mass outflow proportional to the pressure gradient over the boundary. Thus the outflow conditions are set as

$$\left.\begin{aligned} &\frac{\partial}{\partial z}\,(r_g \rho_g \underline{V}_g) = \gamma(p_{ext} - p) \\ &\frac{\partial^2 h_g}{\partial z^2} = 0 \end{aligned}\right\} \qquad (4.33)$$

where γ is a constant representing a resistance to flow and thus setting the proportionality of mass flow to pressure gradient. This constant is calculated from the relationship of Ergun's original equation, equation (4.5), assuming the viscous resistance negligible. As the values of density and particle properties vary along the outlet boundary, the value of γ is set to a constant by averaging variables at this boundary, thus the boundary resistance is calculated as

$$\gamma = \frac{\bar{\rho}_g}{\bar{f}_z dz} \tag{4.34}$$

As the solids velocities are determined by potential flow and the solution of stream functions, the boundary conditions are expressed in terms of stream functions which are in turn derivatives of the inlet velocities.

At the previously defined axis of symmetry, the stream boundary condition is defined as

$$\Psi(0,z) = 0 \tag{4.35}$$

so as to ensure a no flow condition. The solids inlet is from the furnace top, thus specifying a condition for the stream function, at $z=z_{top}$, as

$$\Psi(r,z_{top}) = \lambda\left[\frac{r}{R}\right]^2 \tag{4.36}$$

where

$$\lambda = -\frac{W_s^{in} R^2}{2} \tag{4.37}$$

and where R is the radial distance at the furnace top.

The solids outflow is assumed through the tuyere, so as to simulate the combustion of coke in the raceway region and introduce some of the effects of the stagnant coke region at the furnace central base. Thus the solids motion towards the base is also in a radial direction, as is the case in practice. A no flow condition is set at the furnace base, to amplify the effects on the solids motion in the vicinity of the tuyere, thus the remaining conditions for the base and furnace wall are:

$$\Psi(r,0) = 0 \qquad (4.38)$$

and at $r=r_{wall}$

$$\Psi(r_{wall},z) = \begin{cases} \lambda & , \text{ above tuyere} \\ 0 & , \text{ below tuyere} \end{cases} \qquad (4.39)$$

The condition at the tuyere is set by equation (4.39), thus specifying the solids outflow and preserving continuity of mass flow in the furnace system.

For the solids phase, a mass inflow condition is prescribed to enable the setting of the energy inlet boundary condition. (This mass inflow condition is not used in the solution of the solids velocities). The energy condition is thus defined as

$$\left.\begin{aligned} &\frac{\partial}{\partial z}\,(r_s \rho_s \underline{V}_s) = \omega \\ &\frac{\partial^2 h_s}{\partial z^2} = 0 \\ &h_s = c_s T_s^{in} \end{aligned}\right\} \qquad (4.40)$$

Wall friction is calculated at the verticle sections of the furnace boundary by adding, to the gas momentum equation (2.3), a shear stress per volume, where the shear stress is defined by

$$\tau = - \mu_g \frac{\partial W_g}{\partial r} \qquad (4.41)$$

and only active on the gas velocity parallel to the wall. Throughout the furnace wall boundary a condition of no heat loss is specified, setting up the condition

$$\frac{\partial \Phi}{\partial r} = 0 \qquad (4.42)$$

where Φ is the dependent variable representing the enthalpy of both the gas and solid phase.

CHAPTER 5

SOLUTION PROCEDURE

5.1 Introduction

In this chapter the numerical integration scheme is presented for the solution of the set of differential equations which constitute the mathematical model. The equations to be solved, which are presented in chapter 4, are non-linear, highly coupled and partial differential, with first and second derivatives in two coordinate directions.

For the numerical solution, the blast furnace is discretised into a finite number of four-sided 'control volumes'. The control volumes are of uniform dimensions, however, as the coordinate system is polar cylindrical the control volumes possess a 'volume' dependent on the radial position. The assumption of two dimensions sets the azimuthal angle to 1 radian and thus sets up a volume for the solution in a two dimensional plane. Algebraic finite difference equations are derived for each cell by their integration, observing both physical realism and continuity over each integrating control volume. The finite difference equations are solved by an iterative procedure.

The solution procedure employed is based on the PHOENICS computer program, see Spalding (1981) and Markatos et al (1982). The algorithm implemented to solve the equations is effectively SIMPLEST, see Spalding (1980a) and Spalding (1980b), which is an improved version of the more commonly known SIMPLE, as explained in section 5.4.1. The actual algorithm implemented is an enhanced SIMPLEST, extended to a two phase procedure to deal with a problem of the type considered. A comprehensive discussion as to the reasons for the improved algorithm is given in chapter 8, together with an explanation of its implementation.

5.2 Finite Difference Grid

The finite difference grid has a number of control volumes (control cells) in the r and z directions, respectively. The distribution of grid cells, shown in Figure (5.1), is uniform in the r and z directions. Boundaries are included in the grid to simulate the furnace shape; though these seem crude in the upper part of the furnace, the step boundaries are smoothed off by the inclusion of porosities in the areas and volumes of the relevant control volumes.

The storage location of all the variables, except the velocity components, are at the centre of each control volume, as illustrated by Figure (5.2), and denoted by the node point P. The r-direction neighbours are points E and W, while N and S are the z-direction neighbours. The velocity components are located at the faces of the main control volume (Figure (5.2)), and as a result the control volume surrounding each velocity component will be staggered ahead of the relevant main control volumes, see Figure (5.3).

The advantages of displacing the velocity components are: the velocities are placed between the pressures which derive them; and the velocities are directly available for the calculation of the convective fluxes across the boundaries of the control volumes for each node. The disadvantage is the need for special consideration of the velocity containing control volumes which are displaced.

5.3 Finite Difference equations

5.3.1 The general transport equation

This can be expressed as

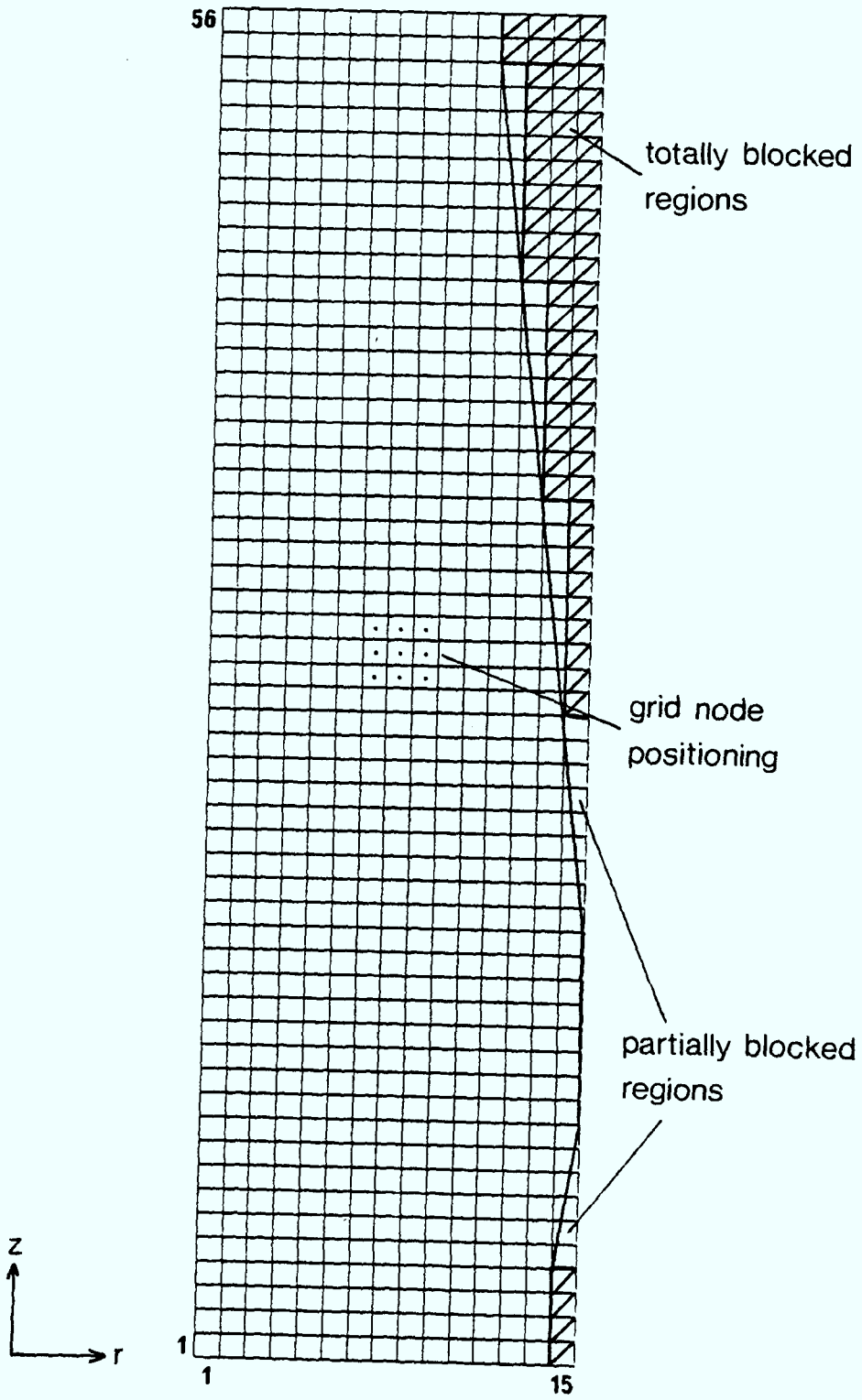

Figure 5.1: Finite difference grid used

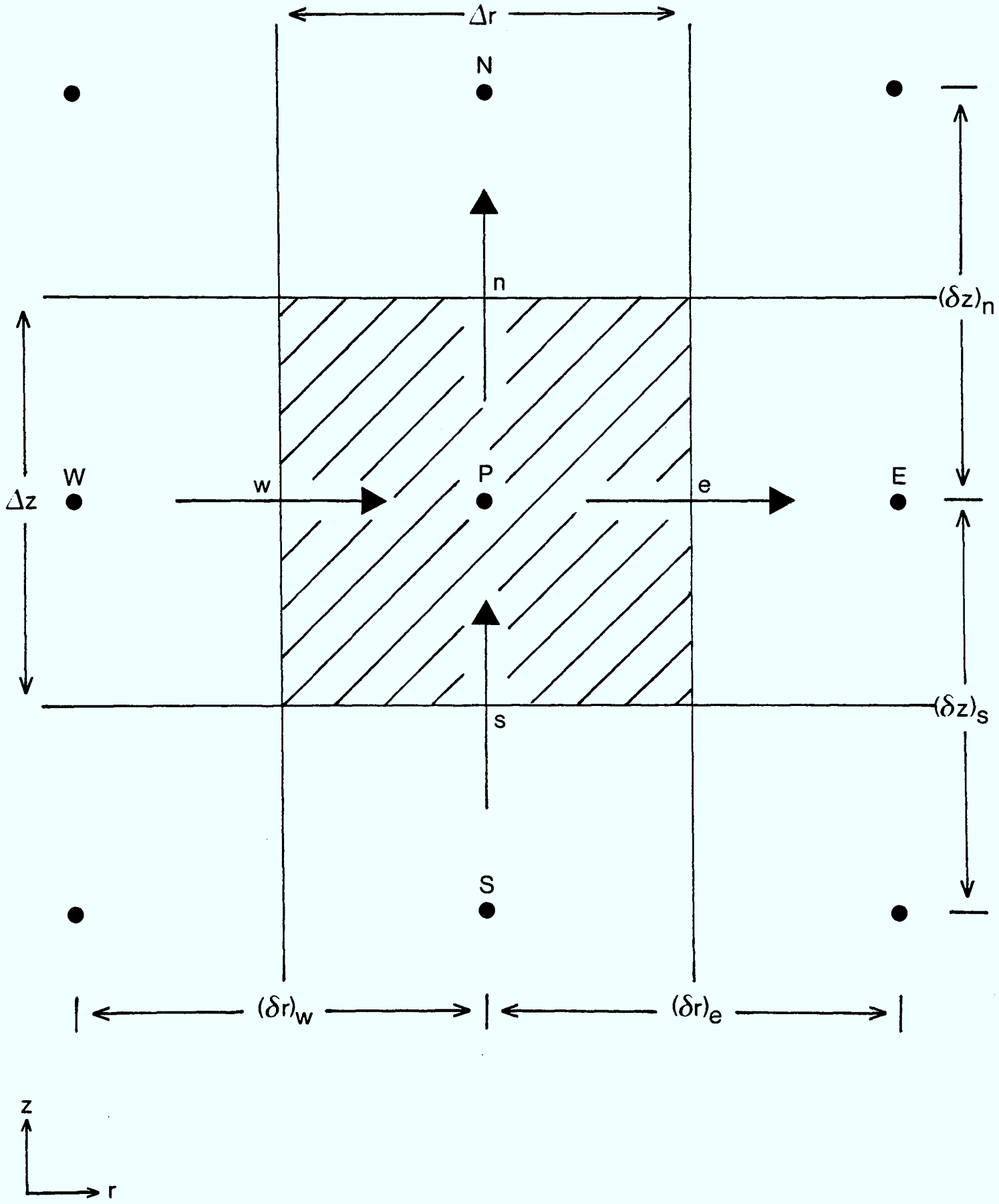

Figure 5.2: Main control volume for portion of grid

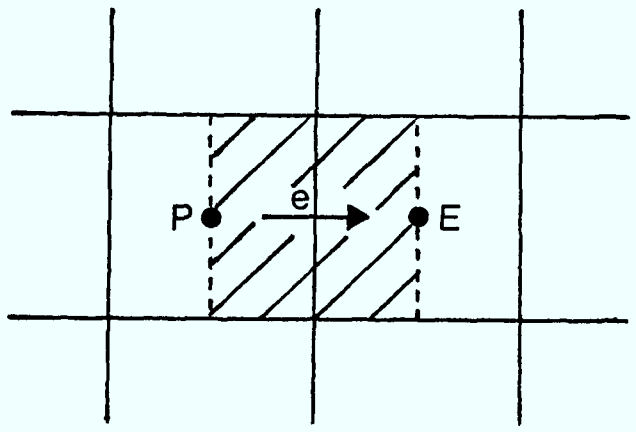

(a) V velocity

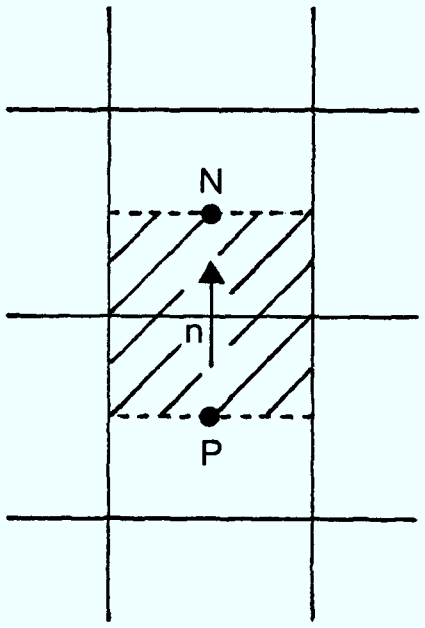

(b) W velocity

Figure 5.3: Staggered control volumes for velocity components

$$\mathrm{div}(r_i\rho_i\underline{V}_i\phi - r_i\Gamma_\phi\ \mathrm{grad}\phi) = S_\phi \qquad (5.1)$$

where the subscript i denotes either gas or solids phase and Γ_ϕ is the transport coefficient for the dependent variable ϕ.

The finite difference equation, related to equation (5.1), is obtained by integrating over the main control volume (Figure (5.2)) for the scalar quantities (ie. h) and over the relevant velocity control volume (Figure (5.3)) for each of the velocity components (ie. V and W).

Integration of equation (5.1) over the main control volume gives:

$$\iiint_V \mathrm{div}(r_i\rho_i\underline{V}_i\phi - r_i\Gamma_\phi\ \mathrm{grad}\phi)dV = \iiint_V S_\phi\ dV. \qquad (5.2)$$

The triple integrals of equation (5.2) are used as the control volume has a "real" volume despite working with only the axial and radial directions.

By the divergence theorem of Gauss, equation (5.2) can be written as

$$\iint_A (r_i\rho_i\underline{V}_i\phi - r_i\Gamma_\phi\ \mathrm{grad}\phi)d\underline{A} = \iiint_V S_\phi\ dV. \qquad (5.3)$$

Discretising over the main control volume, noting that the volume has no flux in the circumferential direction, equation (5.3) becomes

$$(r_i\rho_i V_i\phi - r_i\Gamma_\phi \frac{\partial\phi}{\partial r})_e A_e - (r_i\rho_i V_i\phi - r_i\Gamma_\phi \frac{\partial\phi}{\partial r})_w A_w$$

$$+ (r_i\rho_i W_i\phi - r_i\Gamma_\phi \frac{\partial\phi}{\partial z})_n A_n - (r_i\rho_i W_i\phi - r_i\Gamma_\phi \frac{\partial\phi}{\partial z})_s A_s = V_C\, S_{\phi_P}. \quad (5.4)$$

On describing the partial derivative terms with a piece-wise linear profile, equation (5.4) becomes

$$(r_i\rho_i V_i)_e A_e\phi_e - (r_i\rho_i V_i)_w A_w\phi_w + (r_i\rho_i W_i)_n A_n\phi_n - (r_i\rho_i W_i)_s A_s\phi_s$$

$$+ (r_i\Gamma_\phi)_w \left[\frac{\phi_P-\phi_W}{(\delta r)_w}\right] A_w - (r_i\Gamma_\phi)_e \left[\frac{\phi_E-\phi_P}{(\delta r)_e}\right] A_e + (r_i\Gamma_\phi)_s \left[\frac{\phi_P-\phi_S}{(\delta z)_s}\right] A_s$$

$$- (r_i\Gamma_\phi)_n \left[\frac{\phi_N-\phi_P}{(\delta z)_n}\right] A_n = V_C\, S_{\phi_P}. \quad (5.5)$$

To arrange the equation more compactly, two new symbols F and D, are defined as follows:

$$F \equiv r_i\rho_i U_i A, \qquad D \equiv \frac{r_i\Gamma_\phi A}{\delta *}$$

where F indicates the strength of the convection (or flow), while D is the diffusion conductance. It should be noted that, whereas D always remains positive, F can take either positive or negative values depending on the direction of the fluid flow.

The discretised equation (5.5) can now be written as

$$F_e\Phi_e - F_w\Phi_w + F_n\Phi_n - F_s\Phi_s$$

$$+ D_w[\Phi_P-\Phi_W] - D_e[\Phi_E-\Phi_P] + D_s[\Phi_P-\Phi_S] - D_n[\Phi_N-\Phi_P] = V_C S_{\Phi_P}. \quad (5.6)$$

The values of Φ at the control volume faces are obtained by the upwind difference scheme, which states: The value of Φ at an interface is equal to the value of Φ at the grid point on the upwind side of the face. Therefore the control face values of Φ are represented as

$$F_e\,\Phi_e = \Phi_P[\![F_e,o]\!] - \Phi_E[\![-F_e,0]\!] \quad (5.7a)$$

$$F_w\,\Phi_w = \Phi_W[\![F_w,0]\!] - \Phi_P[\![-F_w,0]\!] \quad (5.7b)$$

$$F_n\,\Phi_n = \Phi_P[\![F_n,0]\!] - \Phi_N[\![-F_n,0]\!] \quad (5.7c)$$

$$F_s\,\Phi_s = \Phi_S[\![F_s,0]\!] - \Phi_P[\![-F_s,0]\!] \quad (5.7d)$$

The volumetric integration of the souce term S_Φ has been expressed as

$$\iiint_V S_\Phi \, dV = V_C \, S_{\Phi_P} \quad (5.8)$$

This is generally expressed in "linearised" form, see Patankar (1980), as

$$S_{\Phi_P} = S^C_{\Phi_P} + S^P_{\Phi_P}\,\Phi_P. \quad (5.9)$$

Substituting the upwind difference form of the Φ_e, Φ_w, Φ_n and Φ_s, equation (5.7), and the linearised source term, equation (5.9), into

the discretised equation (5.6), yields the discretisation equation based on the general differential equation (5.1):

$$(A_P - S^P_{\Phi_P} V_C)\ \Phi_P = A_E\Phi_E + A_W\Phi_W + A_N\Phi_N + A_S\Phi_S + S^C_{\Phi_P}\ V_C \qquad (5.10)$$

where

$$A_E = D_e + [\![-F_e, 0]\!] \qquad (5.11a)$$

$$A_W = D_w + [\![F_w, 0]\!] \qquad (5.11b)$$

$$A_N = D_n + [\![-F_n, 0]\!] \qquad (5.11c)$$

$$A_S = D_s + [\![F_s, 0]\!] \qquad (5.11d)$$

$$A_P = A_E + A_W + A_N + A_S. \qquad (5.11e)$$

(It must be noted that on the RHS of equation (5.11e) there is an extra term $(F_e - F_w + F_n - F_s)$. This term however, with the assumption of no mass transfer, is equal to zero to comply with continuity).

The flow rates and conductances are defined as

$$F_e = (r_i \rho_i V_i)_e A_e \qquad D_e = \frac{(r_i \Gamma_\Phi)_e A_e}{(\delta r)_e} \qquad (5.12a)$$

$$F_w = (r_i \rho_i V_i)_w A_w \qquad D_w = \frac{(r_i \Gamma_\Phi)_w A_w}{(\delta r)_w} \qquad (5.12b)$$

$$F_n = (r_i \rho_i W_i)_n A_n \qquad D_n = \frac{(r_i \Gamma_\Phi)_n A_n}{(\delta z)_n} \qquad (5.12c)$$

$$F_s = (r_i \rho_i W_i)_s A_s \qquad D_s = \frac{(r_i \Gamma_\Phi)_s A_s}{(\delta z)_s} \qquad (5.12d)$$

Finally it should be pointed out that because of the arrangement of the control volume, interpolation is often necessary to evaluate quantities at the required locations.

The volume fractions and densities at the faces of the control volume are calculated by linear interpolation between the nodal values on either side of these faces. However, the diffusion coefficients at the cell faces are computed as the harmonic mean of the nodal values, eg.

$$(\Gamma_\phi)_e = 2/(1/(\Gamma_\phi)_E + 1/(\Gamma_\phi)_P). \qquad (5.13)$$

As the velocities are stored at the cell faces then no interpolation is necessary, thus highlighting the advantage of staggered grids.

5.3.2 The momentum equation

The momentum equation for the gas essentially uses the same formulation as equation (5.10). However, due to the staggered control volumes for the velocity components (Figure (5.3)), the calculation of the diffusion coefficient and mass flow rate at the faces would require an appropriate interpolation. Therefore the coefficients in equation (5.10) would require altering.

When integrating the momentum equation over an appropriate control volume, the source term sees a new term describing the pressure gradient, thus an added term to the RHS of the integrated transport equation would be

$$-\iiint_V \text{gradp}\ dV. \qquad (5.14)$$

Thus the corresponding finite difference equations for the V_g and W_g independent variables are

$$(A_P - S^P_{V_P})(V_g)_e = \sum_i A_i (V_g)_i + S^C_{V_P} V_C + (p_P - p_E)A_e \qquad (5.15)$$

$$(A_P - S^P_{W_P})(W_g)_n = \sum_i A_i (W_g)_i + S^C_{W_P} V_C + (p_P - p_N)A_n \qquad (5.16)$$

where i takes the values E,W,N and S to identify the neighbouring staggered velocities.

5.3.3 The continuity equation

The continuity equation (4.1) is integrated over the main control volume of Figure (5.2) in the same manner as the general transport equation. Therefore integration gives

$$\iiint_V \mathrm{div}(r_g \rho_g \underline{V}_g)\, dV = 0 \qquad (5.17)$$

which discretises to the form

$$(r_g \rho_g V_g)_e A_e - (r_g \rho_g V_g)_w A_w + (r_g \rho_g W_g)_n A_n - (r_g \rho_g W_g)_s A_s = 0. \qquad (5.18)$$

Again it must be noted that appropriate interpolation is required at the cell faces, as explained in section 5.3.1. The discretised form of the continuity equation (5.18) is used in the generation of the pressure correction equation as is explained in the solution of the finite difference equations, section 5.4.1.

5.4 Solution of Finite Difference Equations

The set of finite difference equations described in section 5.3 is solved by an iterative procedure, which is an improved version of the more commonly known SIMPLE algorithm, known as SIMPLEST (see Spalding (1980a) and Spalding (1980b)). The SIMPLE algorithm is

well documented by Patankar (1980) so only a brief outline of SIMPLEST will be presented here. The actual modified algorithm, to deal with the two phases, will not be presented here but in chapter 8, together with explanations as to why existing two phase algorithms proved inadequate. The basic SIMPLEST algorithm is presented here so as to lay down the fundamentals of the method.

5.4.1 SIMPLEST algorithm

In SIMPLE the momentum equations used for the solution of the velocity components are those described by equations (5.15) and (5.16). In these equations the coefficients A_E, A_W, A_N and A_S contain contributions of convection and diffusion. The SIMPLEST algorithm takes the convection contribution from the neighbouring coefficients and adds them to the source term $S^C_{\phi_P} V_C$ thus leaving the coefficients A_E to A_S containing only diffusion contributions.

The resulting momentum equation discretisations are of the same form as equations (5.15) and (5.16) with the coefficients and source terms adjusted.

These momentum equations are solved when the pressure field is given some estimated value, p^*. Unless the correct pressure field is employed the resulting velocity field will not satisfy continuity and thus be denoted by an intermediate velocity field, V_g^* and W_g^*. This velocity results from the solution of the following equations:

$$(A_P - S^P_{V_P})(V_g)^*_e = \sum_i A_i (V_g)^*_i + S^C_{V_P} V_C + (p^*_P - p^*_E) A_e \qquad (5.19)$$

$$(A_P - S^P_{W_P})(W_g)^*_n = \sum_i A_i (W_g)^*_i + S^C_{W_P} V_C + (p^*_P - p^*_N) A_n . \qquad (5.20)$$

The next step is to improve the guessed pressure, p^*, by some pressure correction, p', such that the correct pressure is expressed as

$$p = p^* + p' . \tag{5.21}$$

The velocity is to be corrected, as a result of the pressure correction, in a similar manner,

$$V_g = V_g^* + V_g' \tag{5.22}$$

$$W_g = W_g^* + W_g' . \tag{5.23}$$

On subtracting equations (5.19) and (5.20) from equations (5.15) and (5.16), respectively, an expression is obtained for the velocity correction which is as follows:

$$(V_g)_e' = (p_P'-p_E')A_e/(A_P-S_{V_P}^P) \tag{5.24}$$

$$(W_g)_n' = (p_P'-p_N')A_n/(A_P-S_{W_P}^P) . \tag{5.25}$$

Note the exclusion of the $\sum_i A_i(*)_i'$ terms from equations (5.24) and (5.25), which has been fully discussed by Patankar (1980).

These expressions for the velocity corrections can now be used to construct correction formulae for the velocity components, these being:

$$(V_g)_e = (V_g)_e^* + (p_P'-p_E')A_e/(A_P-S_{V_P}^P) \tag{5.26}$$

$$(W_g)_n = (W_g)_n^* + (p_P'-p_N')A_n/(A_p-S_{WP}^P). \qquad (5.27)$$

Lastly, a pressure correction equation is to be derived from the continuity discretisation equation (5.18) so as to solve for the p' values. Substituting the correction equations (eg. equations (5.26) and (5.27)) for all the velocity components in the continuity equation (5.18), yields the pressure correction equation for p' :

$$A_P p' = A_E p_E' + A_W p_W' + A_N p_N' + A_S p_S' + b \qquad (5.28)$$

where

$$A_E = A_e^2(r_g\rho_g)_e/(A_p-S_{VP}^P) \qquad (5.29a)$$

$$A_W = A_w^2(r_g\rho_g)_w/(A_p-S_{VP}^P) \qquad (5.29b)$$

$$A_N = A_n^2(r_g\rho_g)_n/(A_p-S_{WP}^P) \qquad (5.29c)$$

$$A_S = A_s^2(r_g\rho_g)_s/(A_p-S_{WP}^P) \qquad (5.29d)$$

$$A_P = A_E + A_W + A_N + A_S \qquad (5.29e)$$

$$b = (r_g\rho_g)_w A_w (V_g)_w^* - (r_g\rho_g)_e A_e (V_g)_e^* + (r_g\rho_g)_s A_s (W_g)_s^* - (r_g\rho_g)_n A_n (W_g)_n^*. \qquad (5.29f)$$

The equations to be used in the SIMPLEST algorithm have been described above, the order of operation summarised as follows:

i) Guess the starting pressure field p^*

ii) Solve the momentum equations (eg. equations (5.19) and (5.20) to obtain $(V_g)^*$ and $(W_g)^*$.

iii) Solve the pressure correction equation (5.28).

iv) Calculate new pressure p from equation (5.21).

v) Calculate new velocity components V_g, W_g from equations (5.26) and (5.27).

vi) Solve the discretisation equation (5.10) for the enthalpies, h.

vii) Use the new pressure p as a starting pressure p^* and return to step ii) until convergence is obtained.

This method, in the form of the SIMPLE algorithm is described extensively by Patankar (1980).

5.4.2 Algebraic set of finite difference equations

The algebraic set of finite difference equations for each variable are solved by an iterative procedure in which the set of 'z-slabs' are repeatedly scanned in the positive z direction. The term 'z-slab' refers to the vector of nodes in the radial direction, at a particular axial location.

The finite difference equations for V_g and W_g are solved by the Jacobi point-by-point procedure. Thus, Φ_P is updated, for all nodes of the solution field, from:

$$\Phi_P = (\sum_i A_i\Phi_i + b)/(A_P - S^P_{\Phi_P}) \qquad (5.30)$$

where b contains the source term $S^C_{\Phi_P}$ and the contribution from the pressure gradient. The Φ_i values are the previously calculated values from the last "sweep".

The finite difference equations for h_g and h_s, (ie the energy conservation equations) are solved slab-by-slab by means of a slab-wise linear solver. The linear solver used is a simplified derivative of Stone's Strongly Implicit Method (Smith (1978)). Due

to the solution domain being in the axial and radial directions only, the implementation of Stone's Method reduces to the tridiagonal matrix algorithm.

The finite difference equation for the pressure correction (equation (5.28)) are also solved by means of the simplified Stone's Method. However, while the equations for h_g and h_s were solved slab-by-slab, the pressure correction is solved at the end of a complete axial direction sweep, (ie. a 'whole-field' solution).

5.4.3 Boundary conditions

All boundary conditions are inserted as sources or sinks of one or more variables. These are represented by linear expressions of the form:

$$S_\Phi = C_\Phi(V_\Phi - \Phi_P) \qquad (5.31)$$

where C_Φ and V_Φ are the 'coefficient' and 'value' for the variable Φ. When the boundary condition involves mass inflow or outflow, so that a source or sink of mass is present, the above source expression becomes:

$$\dot{m} = C_m(V_m - p_P). \qquad (5.32)$$

In equation (5.32), V_m has the physical significance of an external pressure; and C_m that of the reciprocal of a flow resistance between the external pressure and the internal grid node. The values for these constants are derived and set down in section 4.3.6.

When mass inflow is present, the source term for all other variables for the phase in question, automatically include the effects of the

inflow, thus defining the linear source expression as

$$S_\Phi = (C_\Phi + [\![0, \dot{m}]\!])(V_\Phi - \Phi_P). \qquad (5.33)$$

C_Φ therefore defines the effects of the diffusive transport for the inflow condition.

These source terms are added to the relevant finite difference equations, and due to their linear form give a finite difference equation of the form:

$$\Phi_P = \frac{(\sum_i A_i \Phi_i + S^C_{\Phi_P}) + (C_\Phi + [\![0, \dot{m}]\!])V_\Phi}{(A_P - S^P_{\Phi P}) + (C_\Phi + [\![0, \dot{m}]\!])} . \qquad (5.34)$$

5.5 Stream Functions

The solids potential flow is solved via equations (4.15), (4.16) and (4.18), as described in section 4.2.3. The manner in which they are discretised over a main control volume is somewhat similar to that laid down in section 5.3, while the solution of the resultant finite difference equation is via Successive Over-Relaxation (S.O.R.). Changes are made to the finite difference grid nodal locations to ease the coupling of gas and solid solutions.

5.5.1 Finite difference grid

The finite difference grid used for the stream functions is the same for the energy transport and gas equations as laid down in section (5.2) and illustrated in Figure (5.1). However, the grid node locations are positioned at the points of intersection of the grid lines, as illustrated by Figure (5.4).

Due to the relationships of equations (4.15) and (4.16),

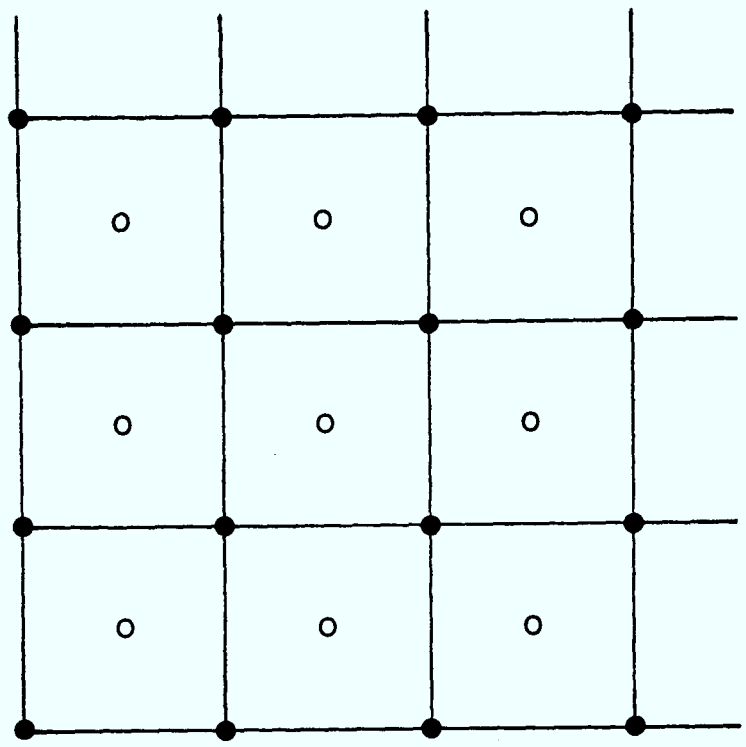

o grid node locations for all discretised equations except stream functions

● grid node locations for stream functions

Figure 5.4: Grid node locations

discretising over the stream function grid gives the required axial and radial solid velocities in the required location, (ie. staggered on the main cell faces). Also, on setting the boundary conditions the grid points at the boundaries are set to the desired values, thus the discretisation equation needs no special treatment.

5.5.2 Finite difference equations

The equation to be discretised is that for the potential flow of the solids, as set down by equation (4.18). The equation is integrated over a control volume, illustrated by Figure (5.5), to yield the finite difference equation. Therefore integrating gives

$$\iiint_V \left[\frac{\partial}{\partial r}\left[\frac{1}{r}\frac{\partial \Psi}{\partial r}\right] + \frac{1}{r}\frac{\partial^2 \Psi}{\partial z^2}\right] dV = 0. \qquad (5.35)$$

The elemental volume dV is given by

$$dV = r\, d\Theta\, dr\, dz \qquad (5.36)$$

which transforms the integral, over the same control volume, to

$$\int_z^{z+\Delta z}\int_r^{r+\Delta r}\int_o^1 \left[\frac{\partial}{\partial r}\left[\frac{1}{r}\frac{\partial \Psi}{\partial r}\right] + \frac{1}{r}\frac{\partial^2 \Psi}{\partial z^2}\right] r\, d\Theta\, dr\, dz = 0. \qquad (5.37)$$

The third integral for Θ, between $\Theta=0$ to $\Theta=1$, is included due to the control volume having an "actual" volume corresponding to a circumferential distance, of angle $\Theta=1$ radian.

Evaluating the integral equation (5.37), gives

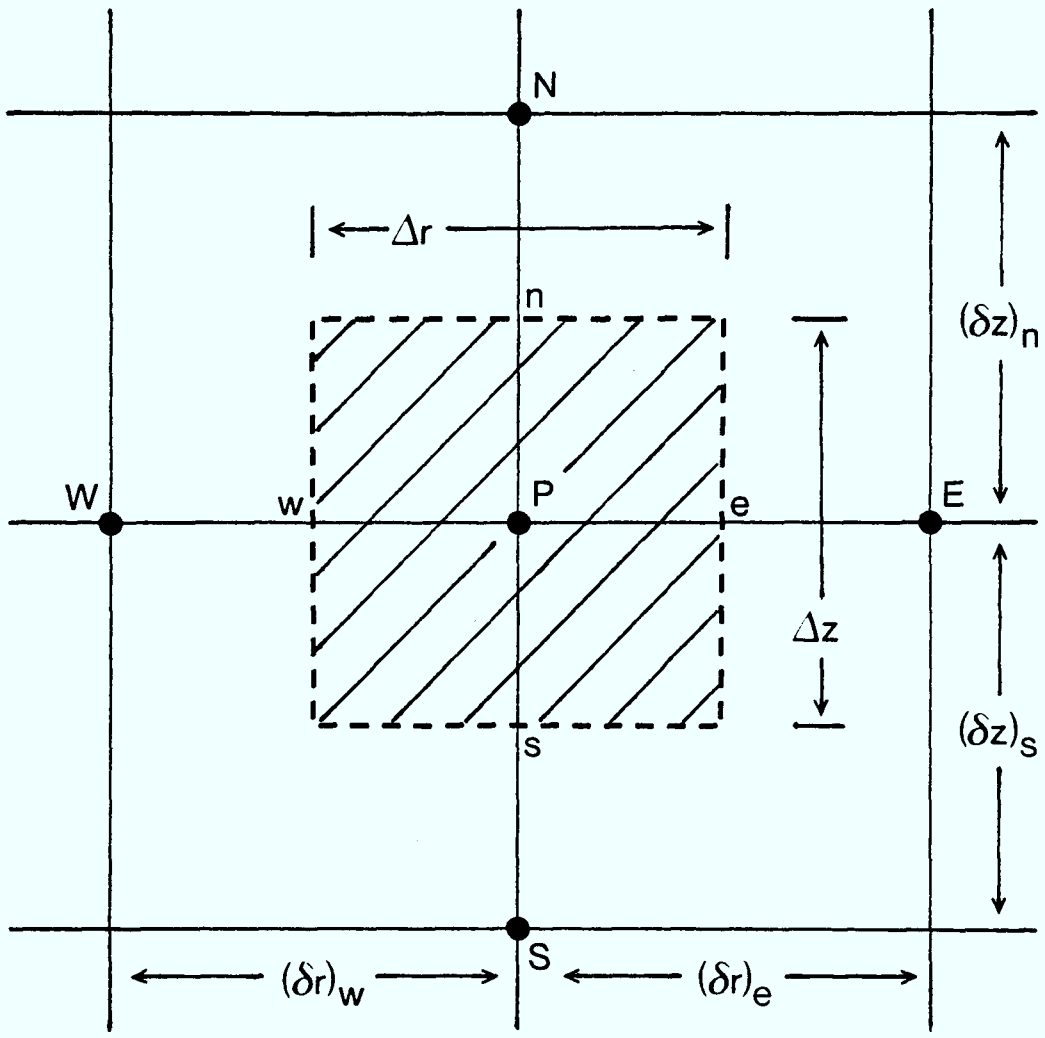

Figure 5.5: Control volume for stream function grid

$$\left[\frac{\partial\Psi}{\partial z}\right]\Delta r - \left[\frac{\partial\Psi}{\partial r}\right]_{z+\Delta z}\Delta r + \left[\frac{\partial\Psi}{\partial r}\right]_{z}\Delta z - \left[\frac{\partial\Psi}{\partial r}\right]_{r+\Delta r}\Delta z - \Delta z\int_{r}^{r+\Delta r}\left[\frac{1}{r}\frac{\partial\Psi}{\partial r}\right] dr = 0. \qquad (5.38)$$

The notation for equation (5.38) can be changed to coincide with that used in Figure (5.5), yielding

$$\left[\frac{\partial\Psi}{\partial z}\right]_{n}\Delta r - \left[\frac{\partial\Psi}{\partial z}\right]_{s}\Delta r + \left[\frac{\partial\Psi}{\partial r}\right]_{e}\Delta z - \left[\frac{\partial\Psi}{\partial r}\right]_{w}\Delta z - \Delta z\int_{w}^{e}\left[\frac{1}{r}\frac{\partial\Psi}{\partial r}\right] dr = 0. \qquad (5.39)$$

The remaining integral of equation (5.39) can be approximated by the average of the east and west control volume face values, yielding

$$\left[\frac{\partial\Psi}{\partial z}\right]_{n}\Delta r - \left[\frac{\partial\Psi}{\partial z}\right]_{s}\Delta r + \left[\frac{\partial\Psi}{\partial r}\right]_{e}\Delta z - \left[\frac{\partial\Psi}{\partial r}\right]_{w}\Delta z - \Delta z\left\{\frac{\left[\frac{1}{r}\frac{\partial\Psi}{\partial r}\right]_{e} + \left[\frac{1}{r}\frac{\partial\Psi}{\partial r}\right]_{w}}{2}\right\}\Delta r = 0. \qquad (5.40)$$

Discretising the partial derivatives, with a piece-wise linear profile, gives

$$\frac{(\Psi_N-\Psi_P)}{(\delta z)_n}\Delta r - \frac{(\Psi_P-\Psi_S)}{(\delta z)_s}\Delta r + \frac{(\Psi_E-\Psi_P)}{(\delta r)_e}\Delta z - \frac{(\Psi_P-\Psi_W)}{(\delta r)_w}\Delta z$$

$$- \frac{\Delta z\Delta r}{2}\left\{\frac{(\Psi_E-\Psi_P)}{r_e(\delta r)_e} + \frac{(\Psi_P-\Psi_W)}{r_w(\delta r)_w}\right\} = 0 \qquad (5.41)$$

which can then be written in the form,

$$A_P\,\Psi_P = A_E\,\Psi_E + A_W\,\Psi_W + A_N\,\Psi_N + A_S\,\Psi_S \qquad (5.42)$$

where

$$A_E = \Delta z(2r_e-\Delta r)/(2r_e(\delta r)_e) \tag{5.43a}$$

$$A_W = \Delta z(2r_w+\Delta r)/(2r_w(\delta r)_w) \tag{5.43b}$$

$$A_N = \Delta r/(\delta z)_n \tag{5.43c}$$

$$A_S = \Delta r/(\delta z)_s \tag{5.43d}$$

$$A_P = A_E+A_W+A_N+A_S \tag{5.43e}$$

The Successive Over-Relaxation procedure is used to solve equation (5.42) to obtain a solution field of the stream function Ψ, which is then used to obtain the axial and radial velocity components of the solids velocity. These are obtained by the discretisation of equations (4.15) and (4.16) over the stream function solution field, giving

$$(W_s)_{i,j} = -\frac{1}{r_{i,j}}\frac{(\Psi_{I+1,J+1}-\Psi_{I,J+1})}{(\delta r)_{i,j}} \tag{5.44}$$

$$(V_s)_{i,j} = \frac{1}{r_{I+1,J}}\frac{(\Psi_{I+1,J+1}-\Psi_{I+1,J})}{(\delta z)_{i,j}} \tag{5.45}$$

where the i,j,I and J subscripts are illustrated in Figure (5.6).

.

5.5.3 Solution of finite difference equations

The finite difference equation for the stream functions is solved by the iterative procedure known as Successive Over-Relaxation (S.O.R.). Applying this method to the finite difference equation (5.42) yields the solution algorithm,

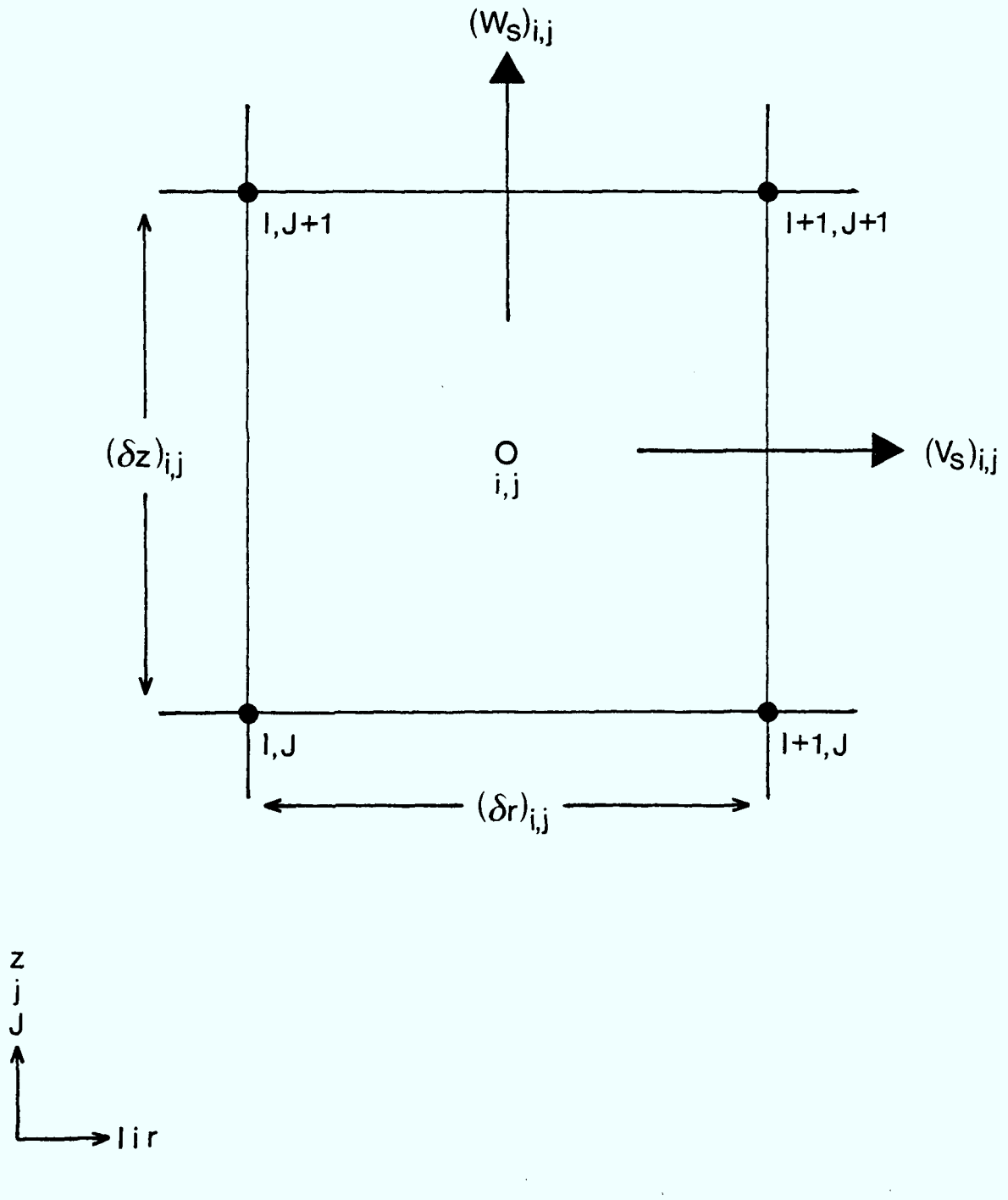

Figure 5.6: Relationship between scalar grid and stream function grid

$$\Psi_P^{(K+1)} = \Psi_P^{(K)} + \bar{\omega} \left[\frac{A_E\Psi_E + A_W\Psi_W + A_N\Psi_N + A_S\Psi_S - A_P\Psi_P^{(K)}}{A_P} \right] \qquad (5.46)$$

where the Ψ_i values in the relaxation factor are the most recently calculated values. The optimum value for $\bar{\omega}$, so as to aid convergence, was found to be $\bar{\omega}=1\cdot8$.

5.6 Solution Sequence for Complete Model

The main finite difference equations and solution algorithms have been discussed extensively in this chapter for all the solved for variables. The complete solution sequence is outlined in the form of a flow chart in Figures (5.7) to Figures (5.11), and from this it is clear how the SIMPLEST algorithm is manipulated in the complete solution.

The stream function solution field is obtained at the start of a solution on the first sweep and stored for the rest of the procedure. This does not need to be recalculated due to the assumption of potential flow specifying a fixed solids density, as explained in section 4.2.3, and thus no coupling with the energy equations.

At the start of each slab solution the particulate properties are accessed to correspond with the relevant zone (see Figure (5.9)); the properties accessed being: effective particle diameter; voidage; and volumetric ratio, of both ore and coke.

In the slab solution for the enthalpy and velocity, Figure (5.10), the sources for each solved variable are added, in the form set down in section 5.4.3, before that variable is solved for along the

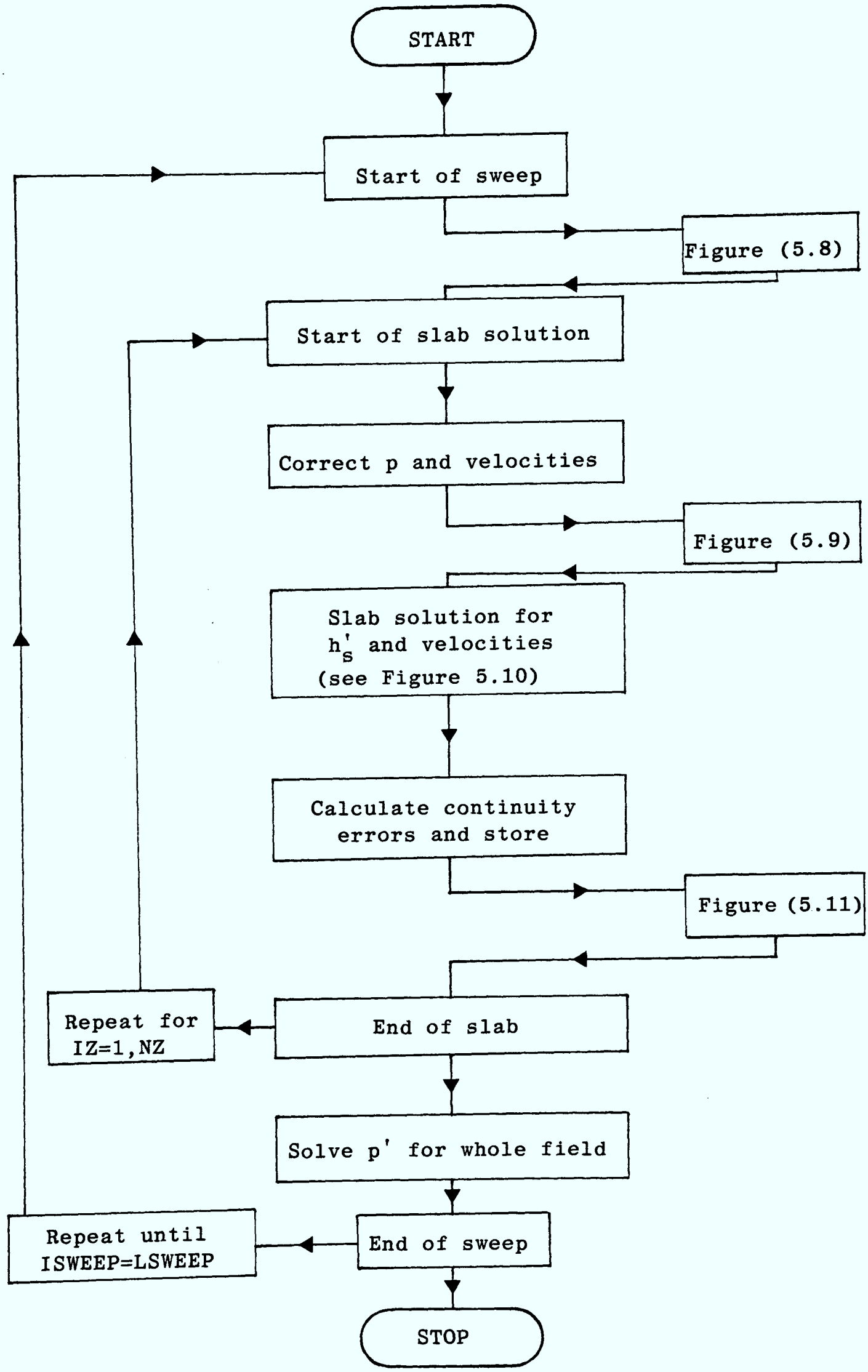

Figure 5.7: Solution sequence flow chart

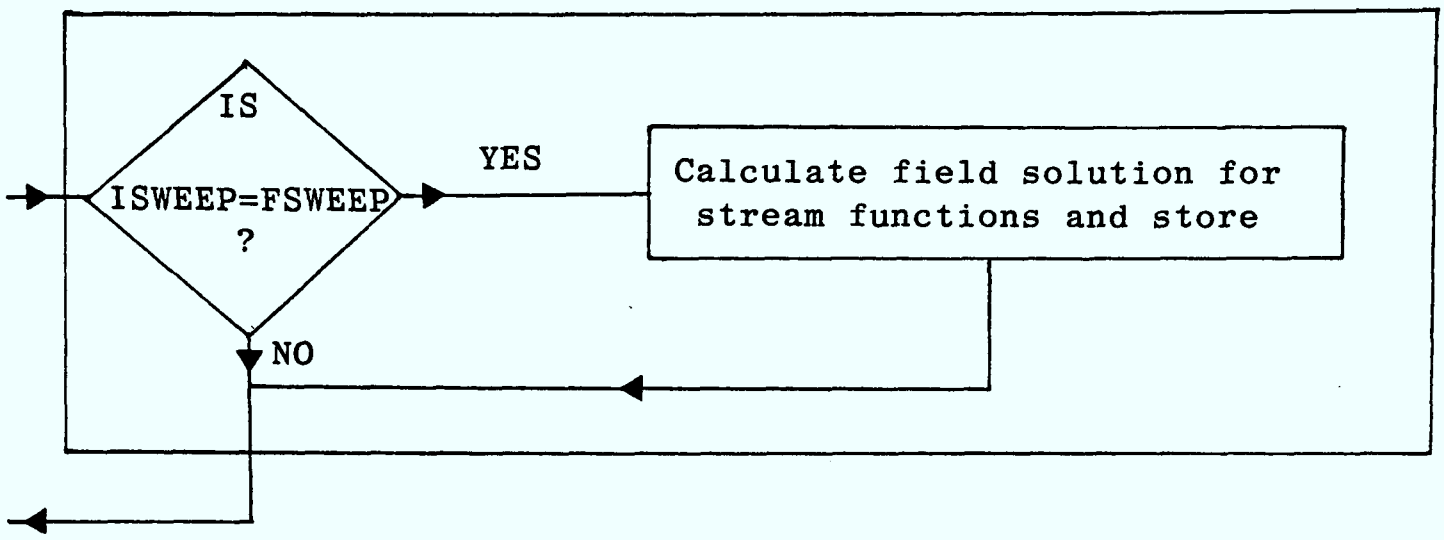

Figure 5.8: Stream function flow chart

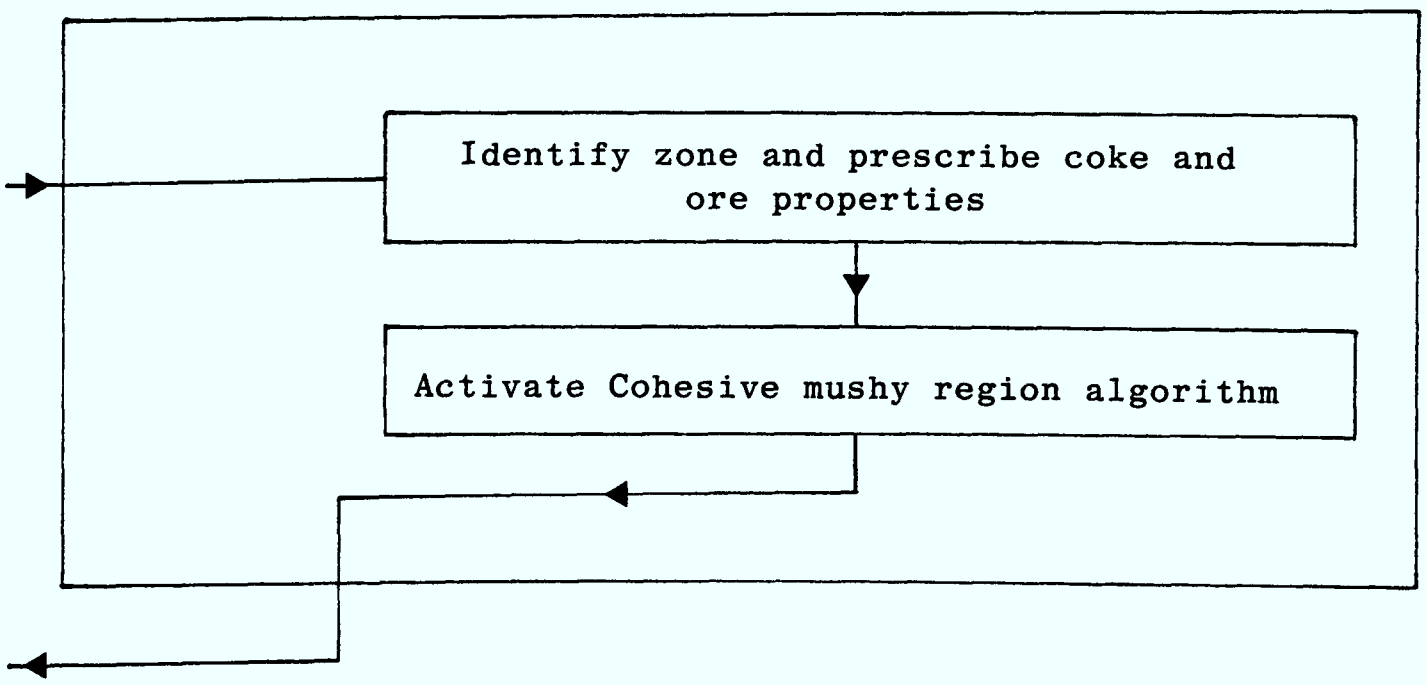

Figure 5.9: Zones properties flow chart

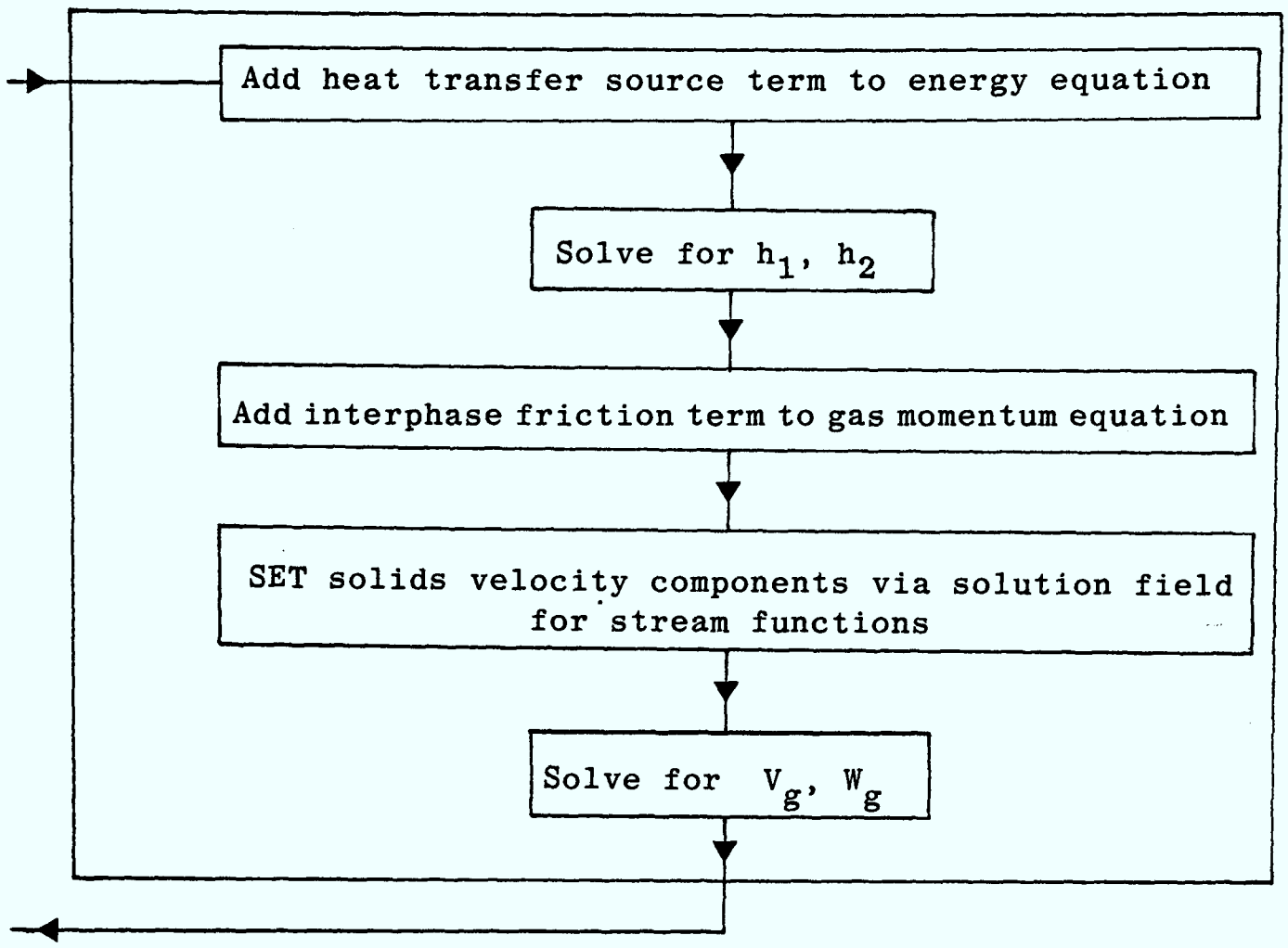

Figure 5.10: Slab solution sequence flow chart

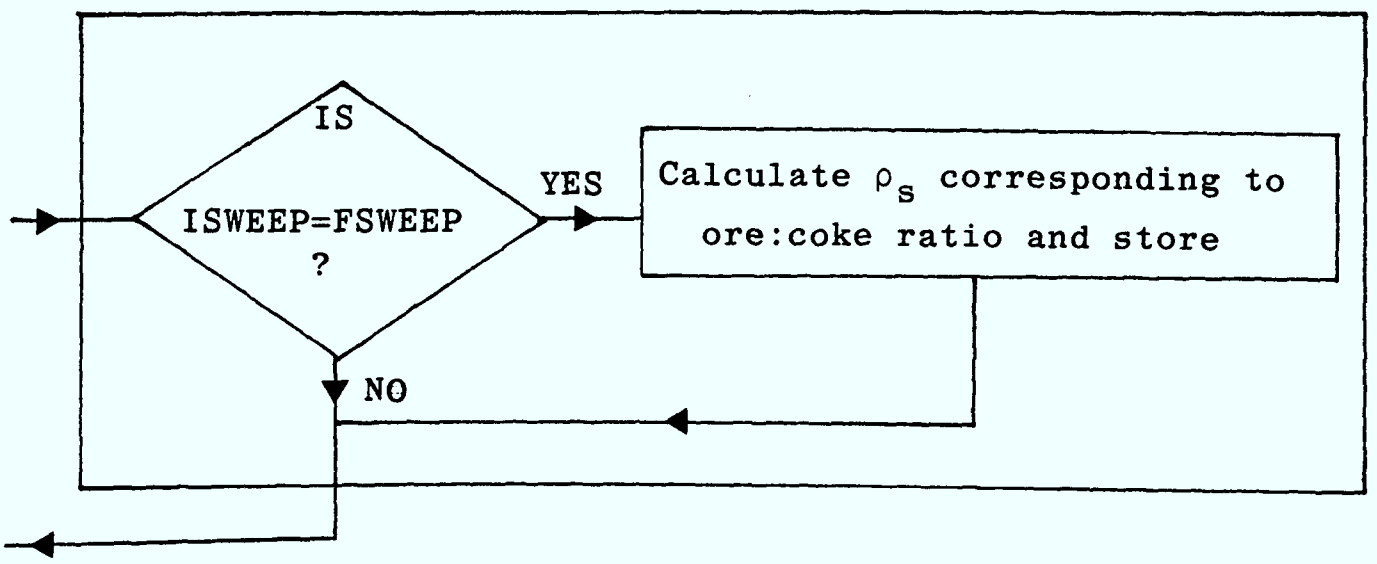

Figure 5.11: Calculation of ρ_s flow chart

particular axial location. At this stage of the algorithm the solid velocity components are set.

The variable solids density, ρ_s, is set up only once, at the first sweep for each slab. The setting of ρ_s at the end of the first solution sweep is for the purposes of programming convenience. The flow chart for this is given in Figure (5.11).

CHAPTER 6

MODEL VALIDATION

6.1 Introduction

A mathematical model of an extremely complex process such as the iron blast furnace involves approximations and empirical laws and cannot be firmly based on proven physical laws. As a consequence, the validation of such a model is an important step in assessing its viability to represent the process realistically.

Ideal validation of a blast furnace model would involve the acquisition of results, such as measurements of pressure, gas velocity and temperature, from a blast furnace operation, under known conditions. In practice however, measurements in the hostile furnace enviroment are so difficult that it renders such an approach impractical, not to mention the requirement of accessability. Fortunately, a lot of work has been carried out by other authors in collecting operating data and performing comparisons against the changes due to furnace characteristics.

Two such sources of information were used in the validation of the current research. Firstly, work carried out by Tashiro et al (1980) successfuly predicted furnace conditions; therefore, by predicting changes a qualitative comparison was attained. The second study was an experimental analogue set up by McIntee and Robertson (1981); this provided a sound basis for a quantitative comparison against the mathematical model. In these validations it is desirable to use data which has been obtained via accurate simulation. For this to be possible the experiments performed must reflect accurately the process operation. The two studies used, successfully simulated melting ore and coke gasification while operating in the confines of an accurately scaled version of an existing furnace, and so provide a sound basis for comparison.

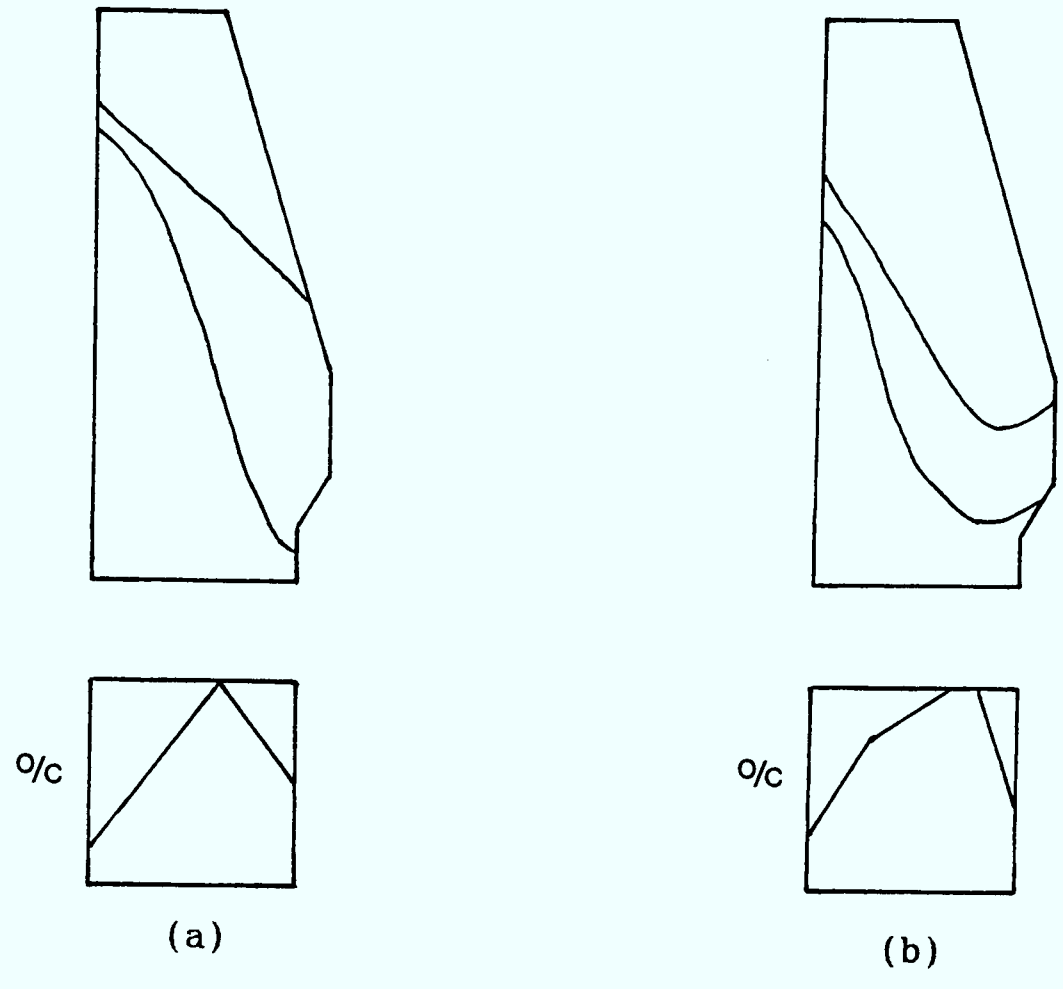

Figure 6.1: A summary of measured ore:coke profiles via Tashiro et al

shape, the inverted U shape and the W shape. The experimental results agreed qualitatively with the empirical results of actual blast furnace operation, therefore the use of these results as a basis for comparison appears justifiable.

6.2.1 Operating conditions

For the comparison against the analysis of Tashiro et al, the operating conditions of the mathematical model has to be those of a large blast furnace. Due to the size of furnace and availability of data it was decided to simulate conditions of the British Steel Corporation Redcar furnace.

The main operating conditions for the standard case are given in Table (6.1). The solids (burden) throughput rate are calculated from the hot metal production rate and the standard case loading rates given in Table (4.2). The standard charging pattern is shown in Figure (4.3) while the voidage and particle properties are laid down in Table (4.1). In all the results presented a layer angle of 30°, measured from the centre out, is assumed, unless otherwise specified. Furnace dimensions are given in Figure (4.1) and these correspond, to within reasonable accuracy to the BSC furnace at Redcar.

Grid refinement took place, on the standard case, and a mesh size of 15×56 across the solution domain was considered acceptable, thereby generating a grid size of ½m×½m. The decision for acceptance of a particular grid was based on the variation of a solution, between a grid size and one finer. The solution variation was observed via the temperature profiles, pressure contours and gas distribution.

Top pressure	=	$1{\cdot}0\times10^{5}$	$kg/m/s^{2}$
Blast temperature (RAFT)	=	2200	°C
Burden temperature	=	15	°C
Lower temp. limit - cohesive zone	=	927	°C
Upper temp. limit - cohesive zone	=	1127	°C
Solid specific heat	=	$1{\cdot}0467$	kJ/kg/K
Gas specific heat	=	$1{\cdot}176491$	kJ/kg/K
Heat transfer coefficient	=	$4{\cdot}1868\times10^{-3}$	$kJ/m^{2}/s/K$
Latent heat of melting	=	$1{\cdot}8422\times10^{2}$	kJ/kg
Thermal conductivity of gas	=	$6{\cdot}754\times10^{-5}$	kJ/m/s/K
Gas mass flowrate	=	$147{\cdot}88$	kg/s
Hot metal production rate	=	8058	T/24hr (iron)

Table 6.1: Standard case operating conditions

All the runs were performed on a Prime 750, and each run on a 15×56 mesh took approximately 10^3 sweeps to converge. The cost of these runs were expensive in terms of CPU (central processing unit) time, as the 10^3 sweeps needed approximately 2×10^4 CPU seconds (5·56 hours). As the Prime 750 was operated on a time sharing system, this meant that the actual run time was a few days.

Together with the standard case run, the charging patterns were changed to observe how well the model reflected the behaviour discussed by Tashiro et al, these patterns are shown in Figure (6.2). The variations were chosen to show the desired effects on the furnace in response to a particular ore:coke ratio change, while observing the 1:1 ore:coke volumetric ratio.

6.2.2 Results

For the standard case, the gas and solids temperature distribution are shown in Figure (6.3), these results show interesting characteristic features. From the shape of the cohesive zone, it is clear that the gas has been diverted to flow through the central region of the furnace, where the ore fraction is lowest, and correspondingly, the resistance to flow is lowest. At the furnace periphery the ore:coke ratio is high, causing the cohesive zone to take the form of the inverted letter U, the low ratio at the furnace centre also contributing.

Three variations to the ore:coke layer profile were carried out, to illustrate the effects on cohesive zone shape (as reported by Tashiro et al), and these are shown in Figure (6.2). The temperature contours resulting in the use of charging pattern Figure (6.2a) are given by Figure (6.4). Due to the excess drop in the

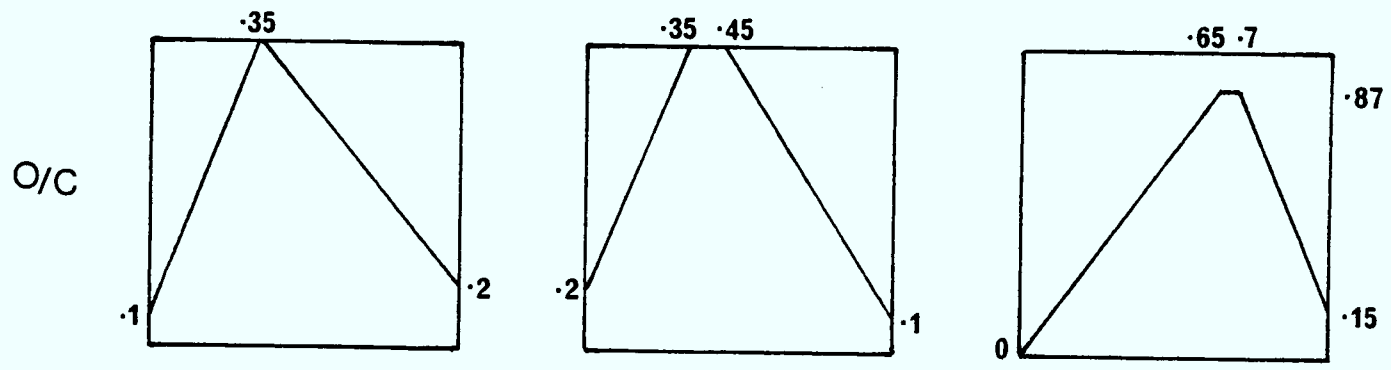

(a) (b) (c)

Figure 6.2: Variations to charging pattern

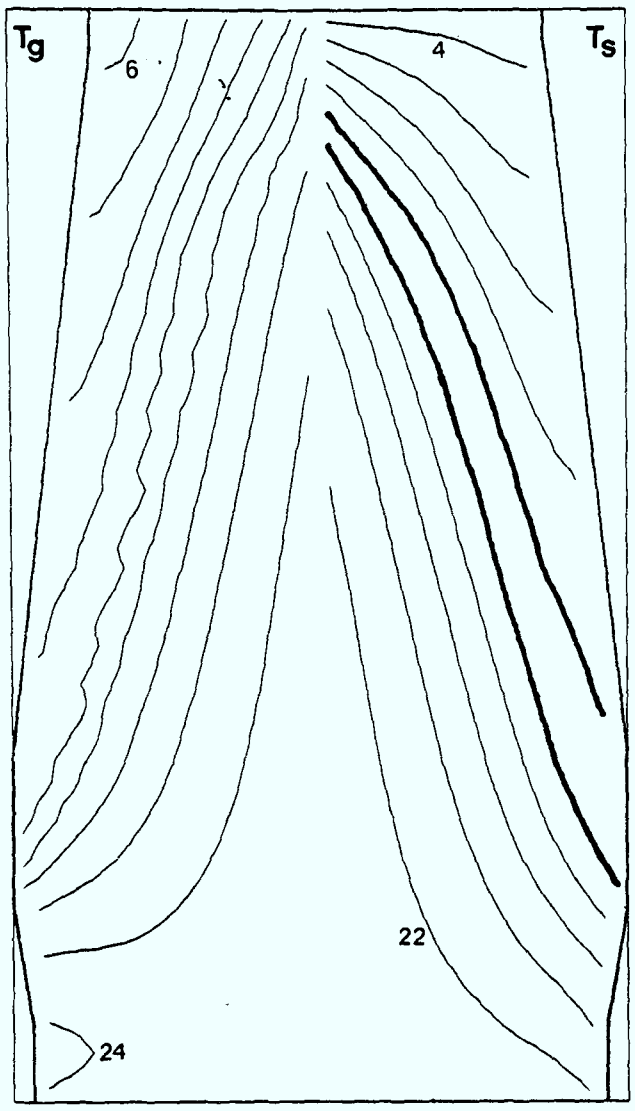

Figure 6.3: Temperature contours(10^2K) standard profile

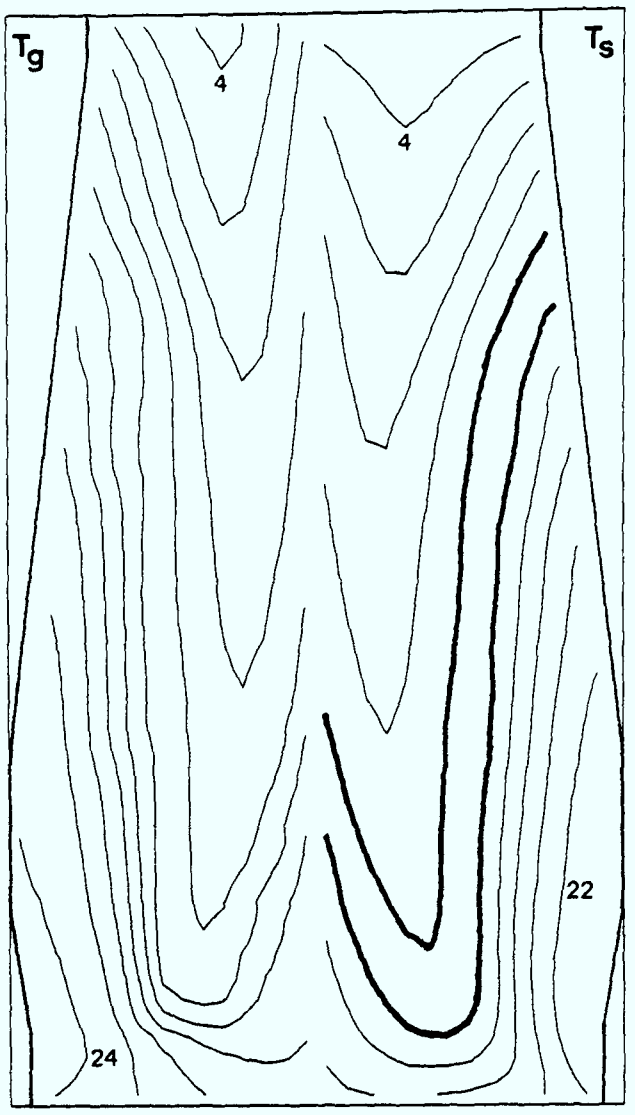

Figure 6.4: Temperature contours(10^2K) profile a

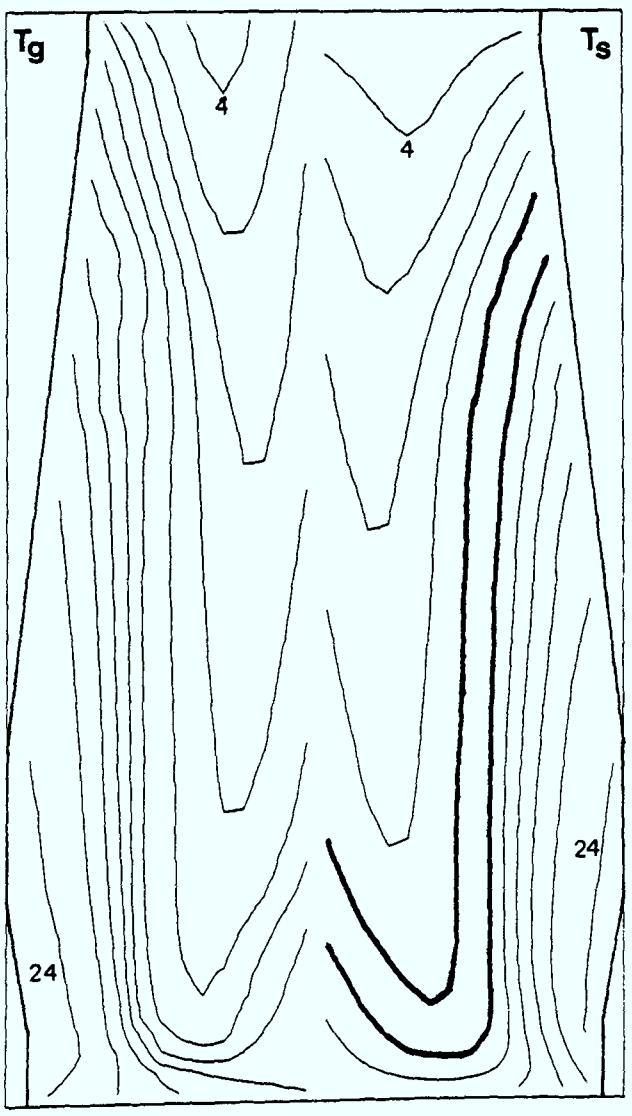

Figure 6.5: Temperature contours(10^2K) profile b

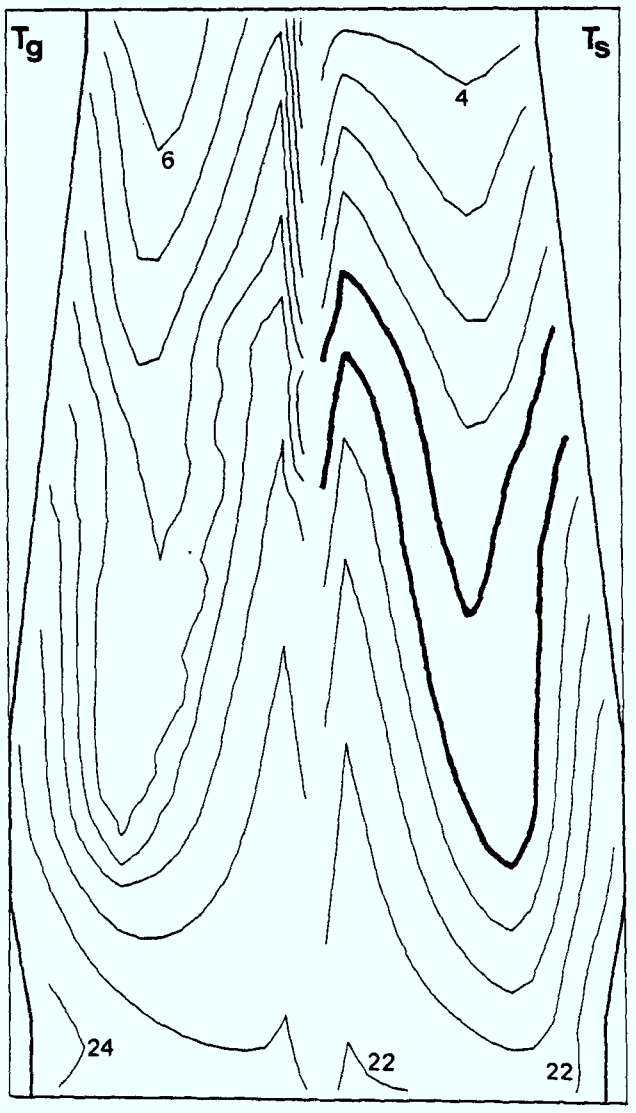

Figure 6.6: Temperature contours(10^2K) profile c

ore:coke ratio on the furnace periphery, and the high ore fraction midway between the furnace centre and wall, the cohesive zone has formed a W shape. Similarly the charging patterns of Figure (6.2b) and Figure (6.2c) induce temperature profiles as shown in Figure (6.5) and Figure (6.6) respectively. In all the three cases, of Figure (6.2), the W shape cohesive zone has been induced due to the diversion of flow through the regions of least resistance. Clearly a high mid-way ore fraction combined with a low ore fraction at the periphery of the furnace causes the geometry of the cohesive zone to be W shaped.

On comparing the ore:coke ratios, at the furnace centre, of Figures (6.2a,b,c), it is apparent that decreasing the ore fraction causes the centre of the cohesive zone to rise, as illustrated by Figures (6.4), (6.5) and (6.6). Similarly, on comparing the ratios of Figure (6.2a) and (6.2b), a decrease in the ore fraction at the furnace wall causes the cohesive zone, again, to rise at this location.

The direct link between burden resistance and cohesive zone shape is further illustrated by the analysis of the mid-way location. Figure (6.6) shows an overall high cohesive zone, and this is caused by the presence of a reasonable coke fraction across the whole radius of the furnace. The height of the mid-way section varies, as shown in the temperature contours, in retrospect to the varying mid-way ore fractions. An increase in the mid-way ore fraction therefore causes a decrease in the respective cohesive zone location.

The results given above indicate that the model reflects the observed experimental evidence of Tashiro et al, and consequently

gives confidence in the accuracy of the model. It is concluded, in conjunction with those of Tashiro et al, that changes in the ore:coke profile can produce quite dramatic changes in the cohesive zone shape.

6.3 Quantitative Comparison

The development of a physical analogue of a large blast furnace was performed by McIntee and Robertson (1981) at the British Steel Corporation laboratories. The experiment was developed with the aim of providing information to be used in the validation of a previously developed mathematical model (Cross et al (1981)).

The model was based on a section of a large blast furnace such as that at Redcar, and built to a scale of 1/20. The burden consisted of layers of naphthalene particles representing coke, and wax particles representing ore; this could be made to behave like a blast furnace by passing air, heated to about 65°C, in at the model tuyeres. The importance of this model was the attempt to simulate both ore melting and coke gasification. A large number of pressure tappings were mounted on one flat face of the model and it was arranged to make temperature measurements also, at this face. The simulated hot blast was fed to six tuyeres by way of a section of bustle main and was monitored by a flow meter, pressure tapping and resistance thermometer installed in the bustle main.

It must be noted that, in the comparison of the analogue to predicted pressures, the data for the analogue values has been corrected for the following reason. As shown in Figure (6.7), the pressure values are given as a fraction of the total pressure drop in the furnace. The original analogue data shows a pressure drop of

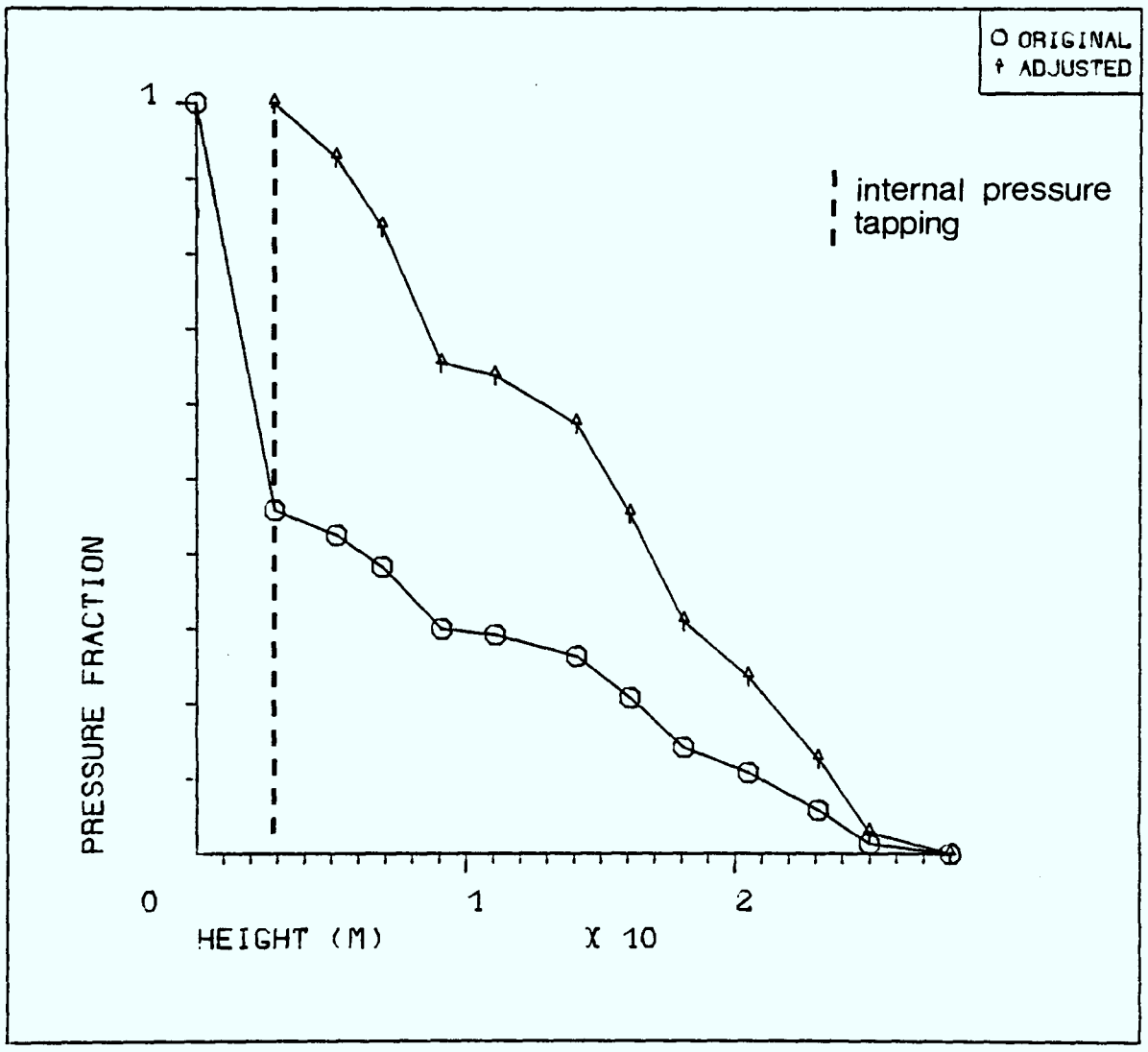

Figure 6.7: Original and Corrected analogue pressures

over 50%, of the total drop, at the lower end of the furnace model. The wax melting zone covered a large portion of the analogue and it is believed that this sharp pressure drop is caused by the interface at the wax melting region. The molten wax fills the voids in the napthalene bed and thus greatly increases the pressure at this interface. These views are supported by the experiments carried out by Szekely and Poveromo (1977), and Szekely and Propster (1979a). The mathematical model does not predict this melting region interfacial pressure drop well, but does however, predict the overall pressure gradient satisfactorily. Therefore, the rest of the data from the pressure tappings is scaled between 0 and 1, where, the total drop is represented by that from the first internal measurement, in the cohesive zone, to the furnace top. The new data is represented in relation to the old in Figure (6.7). This way comparison can be made between the performance of the model against the analogue in, and above, the cohesive zone.

6.3.1 Operating conditions

The experimental analogue, set up by McIntee and Robertson, is a scaled version of the Redcar furnace, and uses materials to simulate those used in operation.

The mathematical model was run to simulate the analogue and thereby required the setting of the parameters appropriate to the analogue test run. Table (6.2) gives the values of the parameters appropriate to the analogue test. These values overwrite those set down in the standard case, as discussed in section 6.2.1. The charging pattern is independent of radial position and set constant, according to the solids volumetric ratios, while the voidage and particle properties are laid down in Table (6.3), and the layer

Top pressure	=	$1{\cdot}0\times10^{5}$	$kg/m/s^2$
Blast temperature	=	66	°C
Solids charge temperature	=	55	°C
Wax softening temperature	=	59	°C
Wax melting temperature	=	62	°C
Solids specific heat	=	1·88406	kJ/kg/K
Gas specific heat	=	1·00483	kJ/kg/K
Heat transfer coefficient	=	$1{\cdot}0625\times10^{-4}$	$kJ/m^2/s/K$
Wax latent heat	=	196·7796	kJ/kg
Thermal conductivity of gas	=	$6{\cdot}754\times10^{-5}$	kJ/m/s/K
Gas mass flowrate	=	$6{\cdot}034\times10^{-2}$	kg/s
Solid mass flowrate	=	$5{\cdot}833\times10^{-4}$	kg/s
volumetric ratios	=	(40% wax	
		(60% naphthalene	
Wax density (true)	=	780	kg/m^3
Naphthalene density (true)	=	1152	kg/m^3

Table 6.2: Parameters appropriate to analogue test run.

Zone	Material	Voidage	Effective particle diameter (m)
stack	wax	0·5	0·01
	naphthalene	0·4	0·019
cohesive	wax	0·1	0·01
	naphthalene	0·4	0·019
active	wax	0·4	0·019
	naphthalene	0·4	0·019

Table 6.3: Experimental analogue particle properties

angle is set to 0°. Furnace dimensions are a 1/20 scale of the original Redcar dimensions, as set in Figure (4.1).

6.3.2 Results

In determining the values of the parameters, for the analogue test, the convective heat transfer coefficient was unknown, and therefore McIntee and Robertson used a guessed value. As a result, the heat transfer coefficient for the mathematical model was estimated after a number of runs to achieve an accurate temperature profile.

The question arose, by the authors, as to whether the temperature measurements from the analogue should be regarded as gas or solids temperatures. Their conclusion was that while the analogue temperature sensors should measure gas temperatures, provision must be given to the solids, particularly in the wax melting zone. In the test run the analogue appeared to be predominantly melting zone, as a result, the measurements were compared with solids temperatures predicted by the mathematical model. The results of the temperature profiles, for both the analogue and model, are shown in Figure (6.8). The analogue temperature at the tuyere level shows a value of 66°C, and as the temperature sensor at this point would be more likely to measure the gas temperature (due to the melting zone not being as low as the tuyere level), this value was used as the blast temperature. (The latter point has been mentioned due to the authors specifying a gas input temperature of 65°C).

As shown in Figure (6.8), the cohesive zone has been marked in the range 59-62°C, and the model successfully predicts the changes in temperature gradient in accordance with the cohesive zone. In the analogue report, the authors were unsure of the true softening and

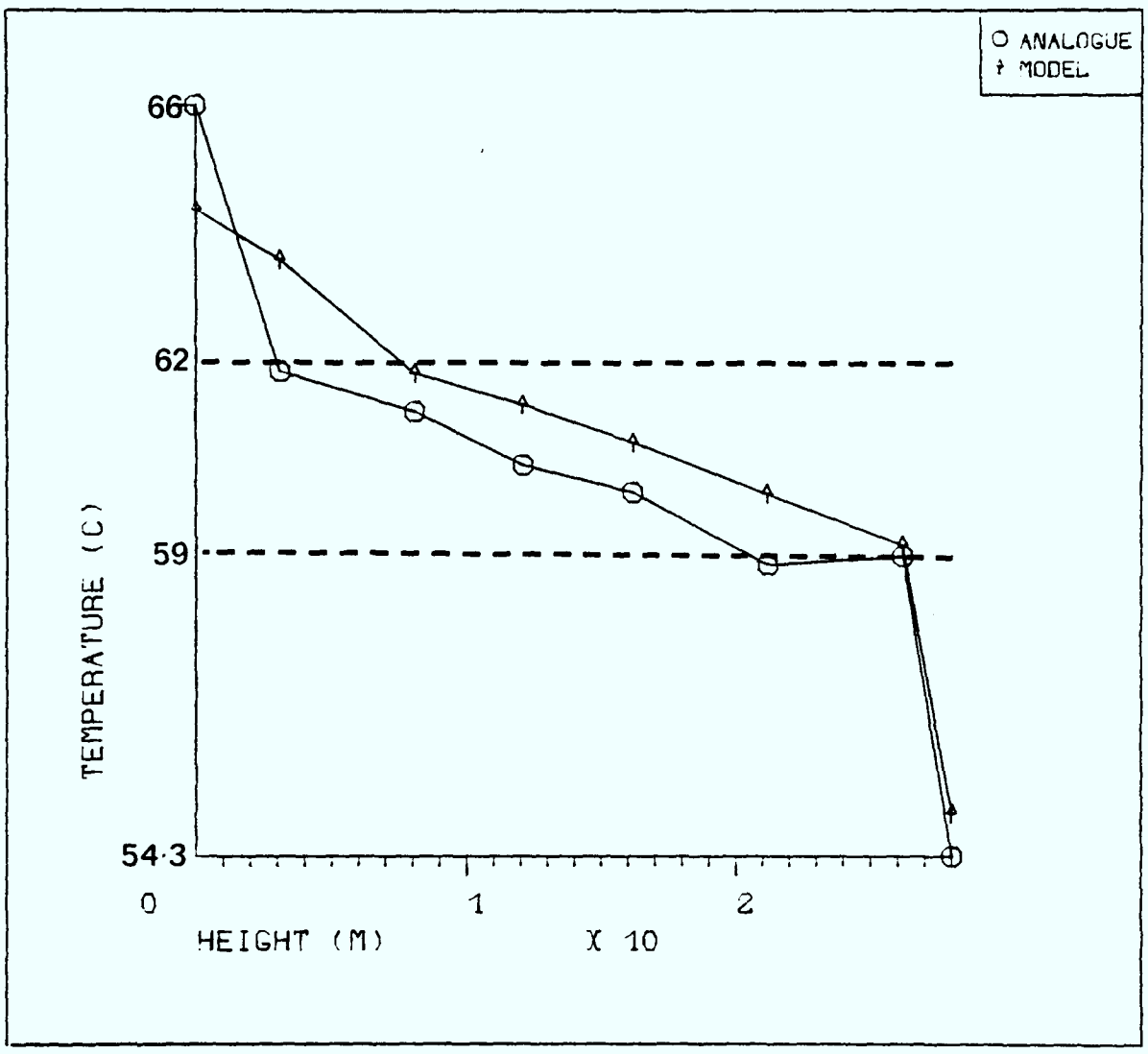

Figure 6.8: Temperature profiles

melting temperatures of the wax which led to uncertainty as to the range of the cohesive zone. On inspection of the analogue temperature profile, Figure (6.8), it is apparent that the temperature range is at least 59-62°C, consequently, this is the range used in the mathematical model. At the tuyere level it is observed that the model underpredicts the temperature, this is not the case. The analogue sensor at this point is more likely to be measuring the gas temperature, for reasons adumbrated earlier, whereas the model profile is presenting a predicted solids temperature, thus accounting for the discrepancy.

Figure (6.9) shows the pressure gradient for the analogue and predicted model. The model profile is a reasonable fit to the analogue, though more importantly the presence of the cohesive zone can be identified. Towards the simulated top of the furnace the softening region boudary can be associated with the sudden change in gradient of the profile. While towards the tuyere level, the melting region boundary is identified by the marked shallowing of the profile gradient. Figure (6.9) therefore shows an acceptable comparison between pressure gradients, which agree with the location of the cohesive zone also illustrated by the temperature profiles of Figure (6.8). To compare this more closely, Figure (6.10) compares the pressure gradient predicted by the model against the analogue temperature profile, where the dashed lines highlight the softening and melting regions. It is clearer now that the predicted pressure gradient reflects the positioning of the cohesive zone.

A more dramatic pressure gradient is not observed as it must be remembered that in the analogue, and predicted model, the cohesive zone spreads over most of the furnace. As a result, the sudden

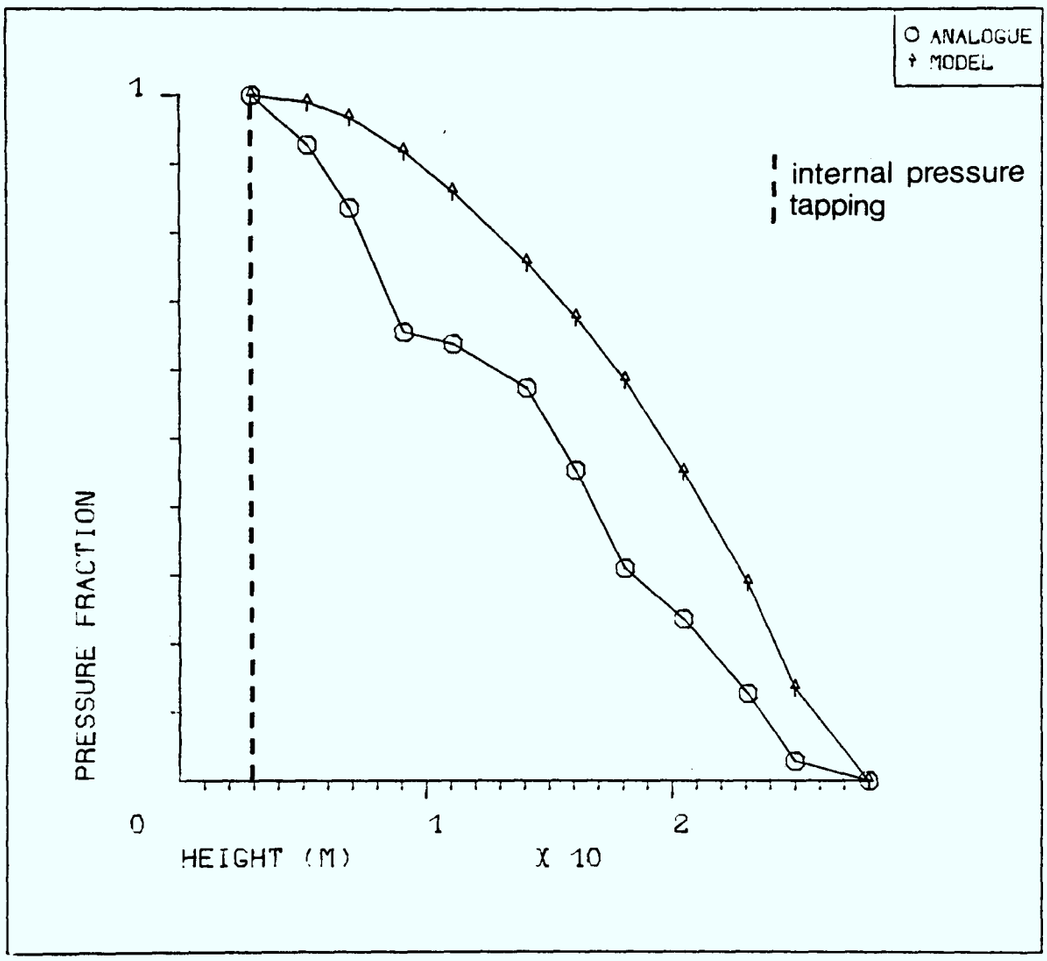

Figure 6.9: Pressure profiles

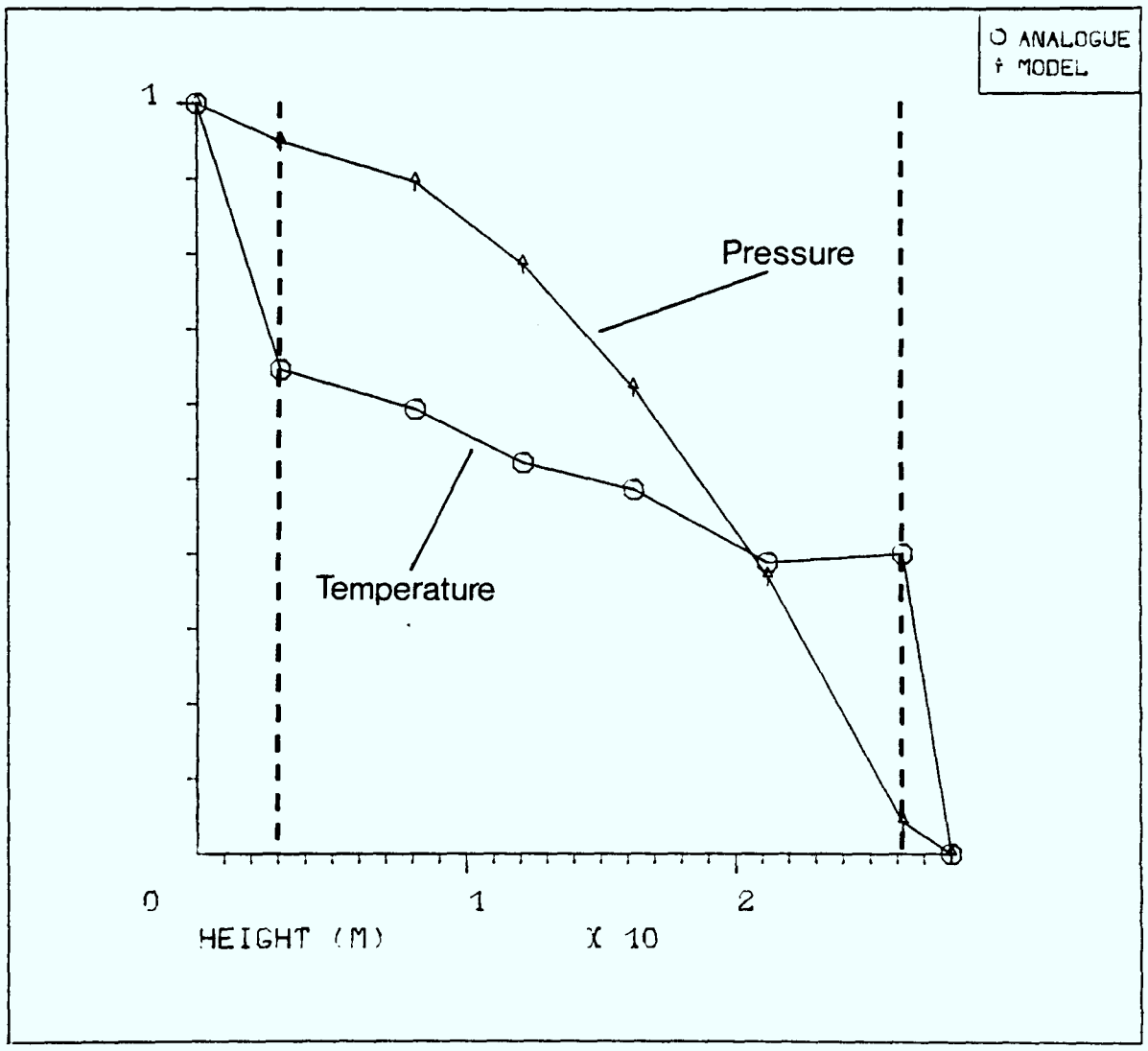

Figure 6.10: Analogue temperature vs model pressure

pressure changes above and below the cohesive zone will not be as noticeable.

6.4 Conclusion

The successful validation of the current model has been carried out against two highly appropriate studies. Tashiro et al performed an experiment to confirm the behavioural characteristics of a large blast furnace; while, McIntee and Robertson carried out quantitative studies on an analogue of an existing furnace for the purposes of model validation.

The current model predicted the same characteristic changes due to profiles of burden distribution, as outlined by Tashiro et al, forming the main U and W cohesive zone shapes. Similar conclusions were drawn as to the specific causes of shape change, leading to the further conclusion that confidence may be given to the accuracy of the model. The model further provided an acceptable fit to the analogue results of McIntee and Robertson, thereby giving stronger evidence of the suitablity for prediction of process features in a large blast furnace.

CHAPTER 7

MATHEMATICAL MODEL RESULTS

7.1 Introduction

Having developed the mathematical model of some aspects of the blast furnace, as described in chapter 4, it was then used to study the effects of various changes of furnace properties.

The ore:coke charging profile was varied to show the significance on furnace behaviour, and the results were used in the validation of the model in section 6.2. Other effects, of importance to the research, was the role of the raceway on the gas distribution throughout the furnace. The importance of modelling the 'deadman' was reported, while showing a similar behaviour to the raceway in terms of affecting gas distribution. Other parameters were then varied, such as charging angle and blast rate to show their stable behaviour to fluctuations.

The temperature distribution contours for the changes in ore:coke charging profiles are given in chapter 6, however for clarity and reading continuity they will be presented again. The explanation of the results however will be a summary of that given in chapter 6 together with discussion of the related pressure profiles, yet unseen.

It must be pointed out that no streamlines or velocity contours are presented; the reasons for which now follow. As stressed in the research aims, the geometry and position of the cohesive zone is a major factor in determining the furnace gas distribution, thereby being highly significant in the control of the iron blast furnace. As a result the temperature contours of both the gas and solids are presented. The pressure contours are also given so as to enable the determination of the changes of resistance together with the flow

directions of the gas. On comparing both contour plots, it is clear how the gas distributes and affects the cohesive zone geometry. It is therefore considered unnecessary to also present velocity and streamline plots as the gas distribution and cohesive zone geometry are the major factors under consideration and they have already been identified by the presented contours.

7.2 Ore:Coke Profile

The results to the changes in the ore:coke profile are given in the validation of the mathematical model, chapter 6. However a summary will be presented together with an additional discussion on the gas distribution.

Results were obtained for each of the charging patterns of Figure (6.2) together with the standard profile of Figure (4.3). The temperature contours for the standard profile and changes (a),(b) and (c) are given in Figures (7.1) to (7.4) respectively. The high ore:coke ratio at the furnace wall, for the standard case, causes the inverted U cohesive zone to take shape. In the various profiles of Figure (6.2), the ratio at the wall drops dramatically causing the cohesive zone to take on the W shape. A decrease in the ore:coke ratio, at either the furnace centre or periphery results in an increase in the cohesive zone position at the respective location (ie. centre or periphery).

Pressure contours for the standard charging profile and varying profiles (a),(b) and (c) are given in Figures (7.5) to (7.8) respectively. From these, together with the ore:coke ratios, the gas distribution can be determined. For the standard ore:coke profile, the low central ratio, together with the relatively high

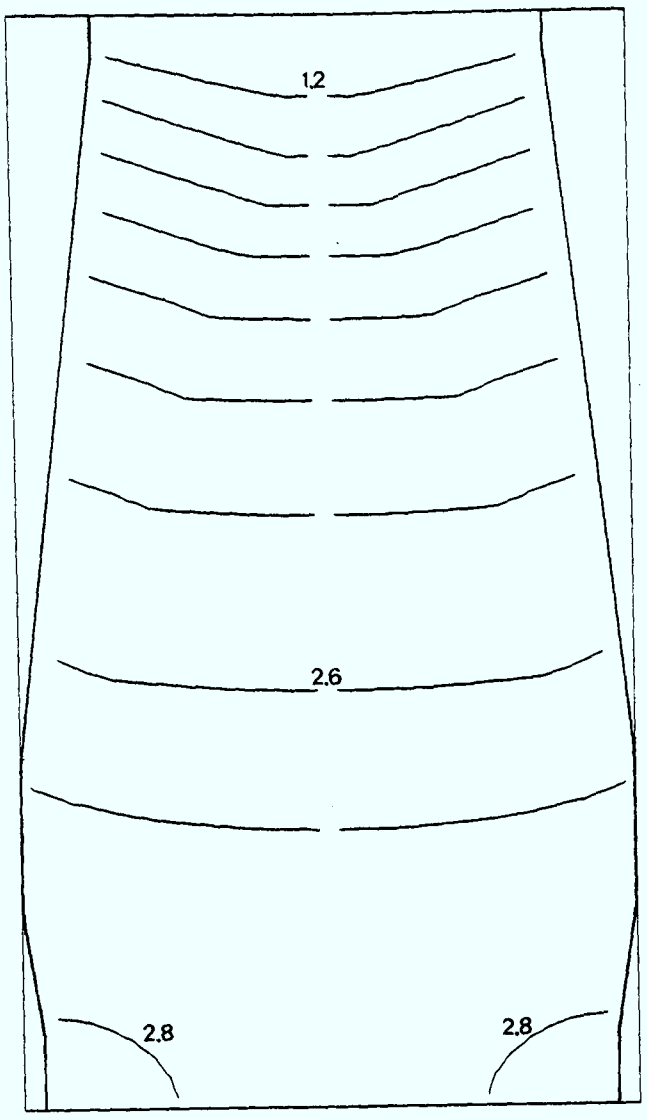

Figure 7.5: Pressure contours(bars)
standard profile

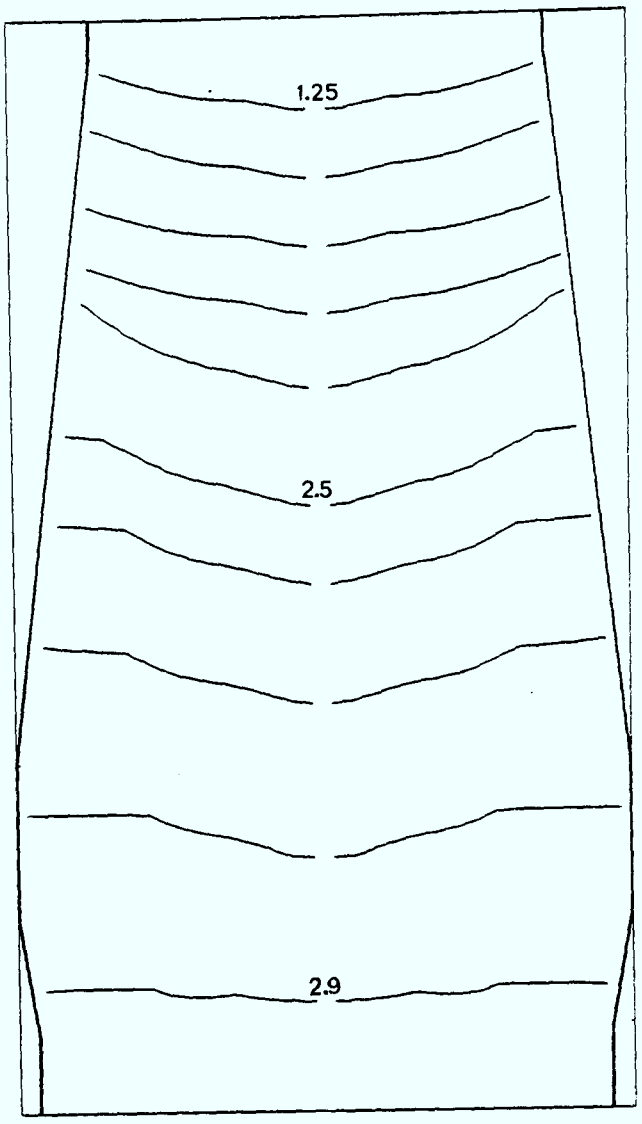

Figure 7.6: Pressure contours(bars)
profile a

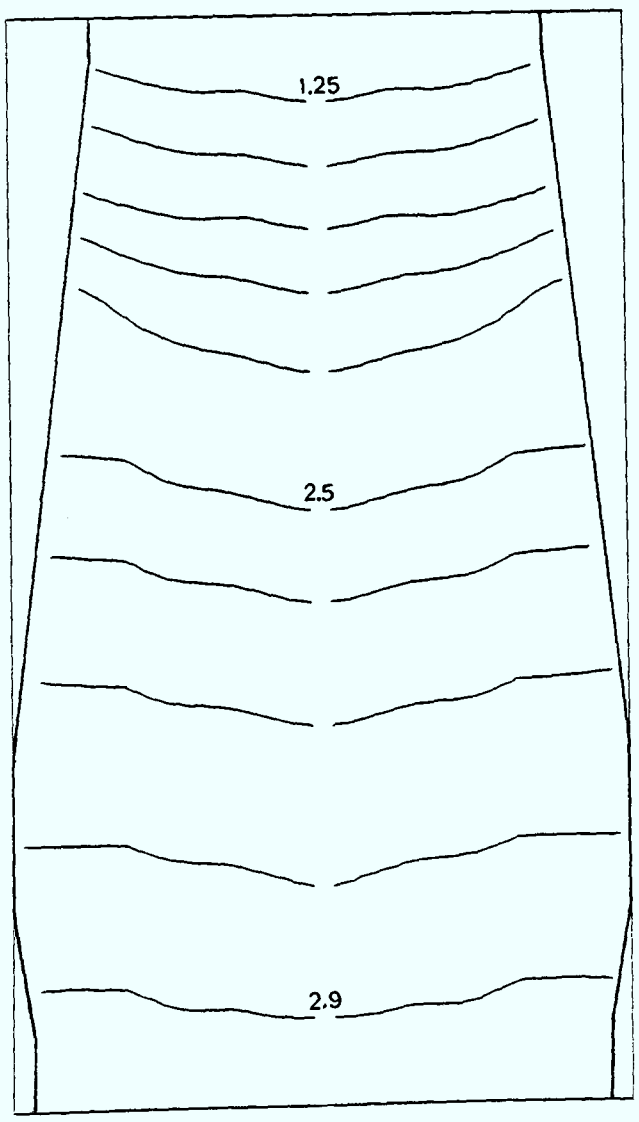

Figure 7.7: Pressure contours(bars)
profile b

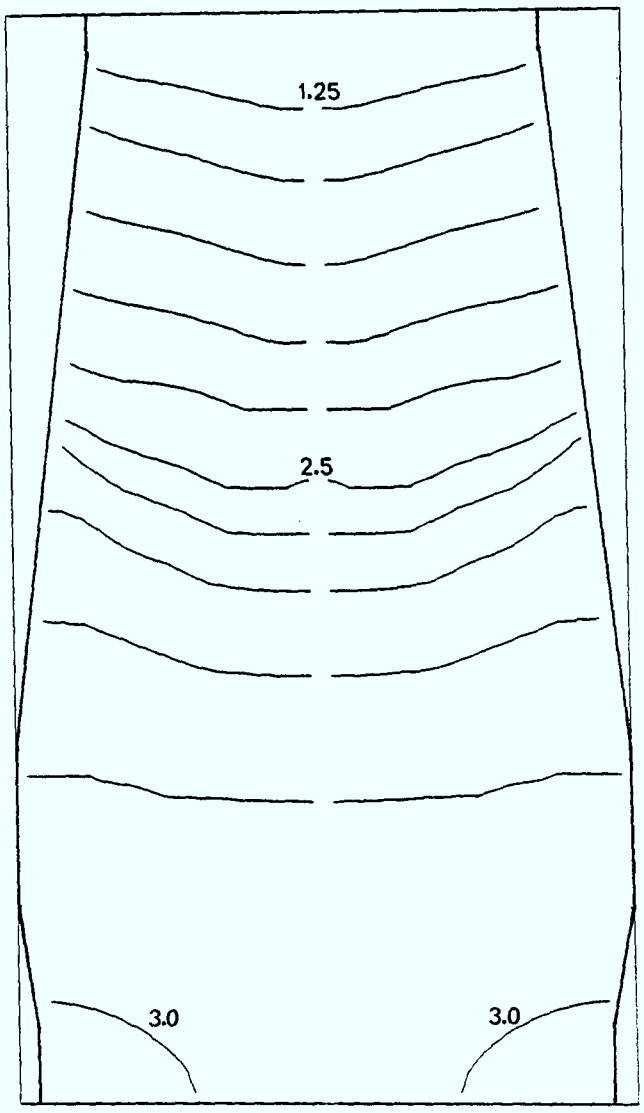

Figure 7.8: Pressure contours(bars)
profile c

peripheral ratio, produces higher resistance to flow at the walls. This causes the gas to flow predominantly up the centre of the furnace, illustrated by the radial pressure gradients of Figure (7.5). The pressure contours also illustrate the fairly even gas distribution in the active coke zone (ie. below the cohesive zone). Above the cohesive zone, in the stack, the solids properties are for both ore and coke, therefore the resistances are set by the ore:coke profile such that the distribution of gas is towards the furnace centre.

Both profiles (a) and (b) cause a W shaped cohesive zone due to the low ore:coke ratio at the furnace periphery, as does profile (c). The gas distribution for the cases (a) and (b) are relatively clear to see from their pressure contours, Figures (7.6) and (7.7). In contrast to the standard case the gas distribution is initially opposite. The flat radial pressure gradients at the periphery, below the cohesive zone, show the flow to be distributed evenly up along the walls, consistent with an even resistance. The radial gradients at the furnace centre line show the flow to be travelling towards the centre as it crosses the cohesive zone. It continues this flow direction on entering the stack due to a combination of the ore:coke profile and charging angle prescribing the directional resistances.

The gas distribution for profile (c) is not so obvious, however, on careful inspection of the pressure contours of Figure (7.8) together with the location of the cohesive zone, illustrated in Figure (7.4), the distribution becomes apparent. The relatively flat radial pressure gradients show the flow to be travelling, with an even profile, either side of the cohesive zone (ie. along the centre and

periphery regions). The flow, on crossing the cohesive zone, ascends the furnace distributing towards the furnace centre.

The strong gas distribution, in all the ore:coke profiles, towards the furnace centre is mainly due to the low ore:coke ratio at this location once in the stack region. This is a result of the regions resistances being directly dependent on the above ratio and charging angle.

7.3 Raceway Shapes

Having identified the importance of the charging profile it was of interest to the current research to identify the role of the raceway. The implementation of an existing raceway model would be too involved a step to take. It was also believed that due to the complex nature of such a model, the reasons for various effects on the furnace process would be difficult to isolate directly. It became apparent, therefore, that what was needed was basic raceway shapes whereby causes could easily be identified. As a result two basic shapes were used, as shown in Figure (7.9); shape A was used to show the effects of raceway penetration and shape B the effect of vertical growth. These two basic changes were chosen, as the work to date on raceway formation has shown great importance on depth and height. The two geometries are implemented against the standard ore:coke profile and profiles (a),(b) and (c).

The first set of results were generated with raceway A. This was achieved by setting the volume fraction of gas very high. The temperature contours for; the standard, (a),(b) and (c) profiles are shown in Figures (7.10) to (7.13) respectively, together with their corresponding pressure contours in Figures (7.14) to (7.17)

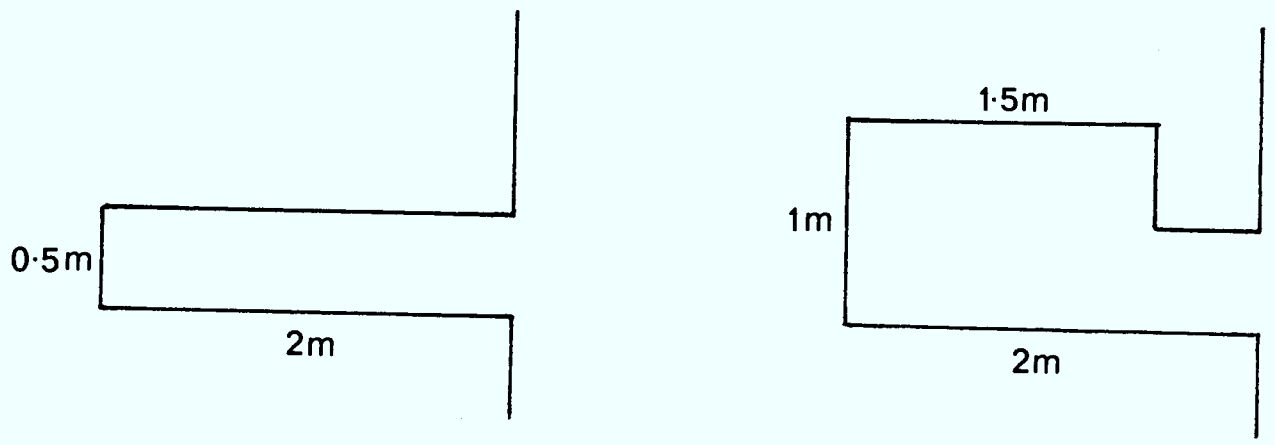

Figure 7.9 Assumed raceway geometries

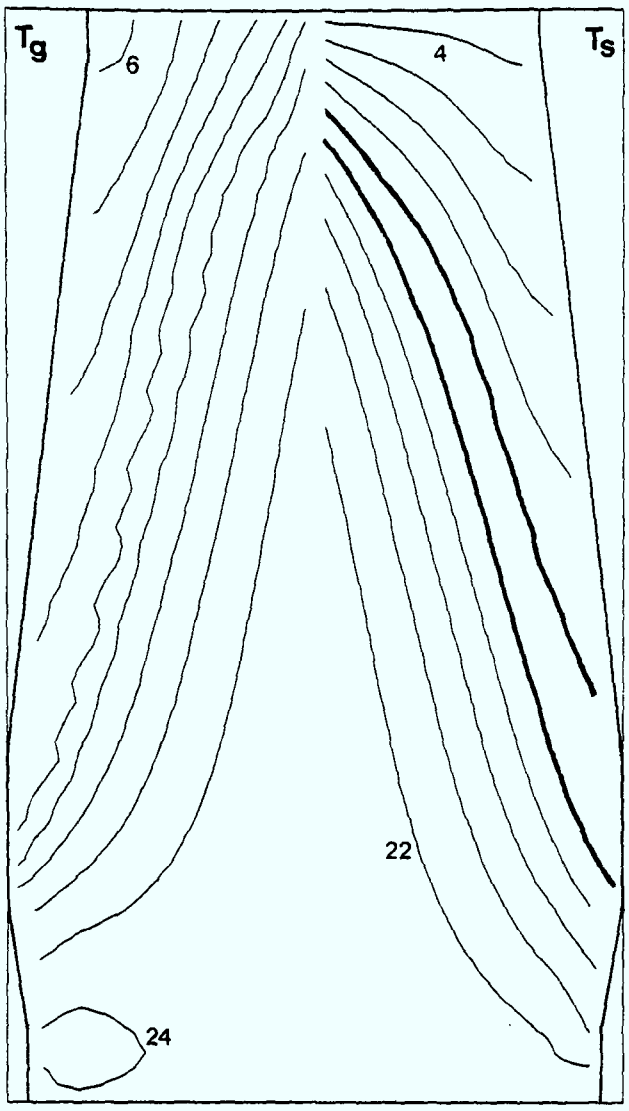

Figure 7.10: Temperature contours(10^2K) raceway A: std. profile

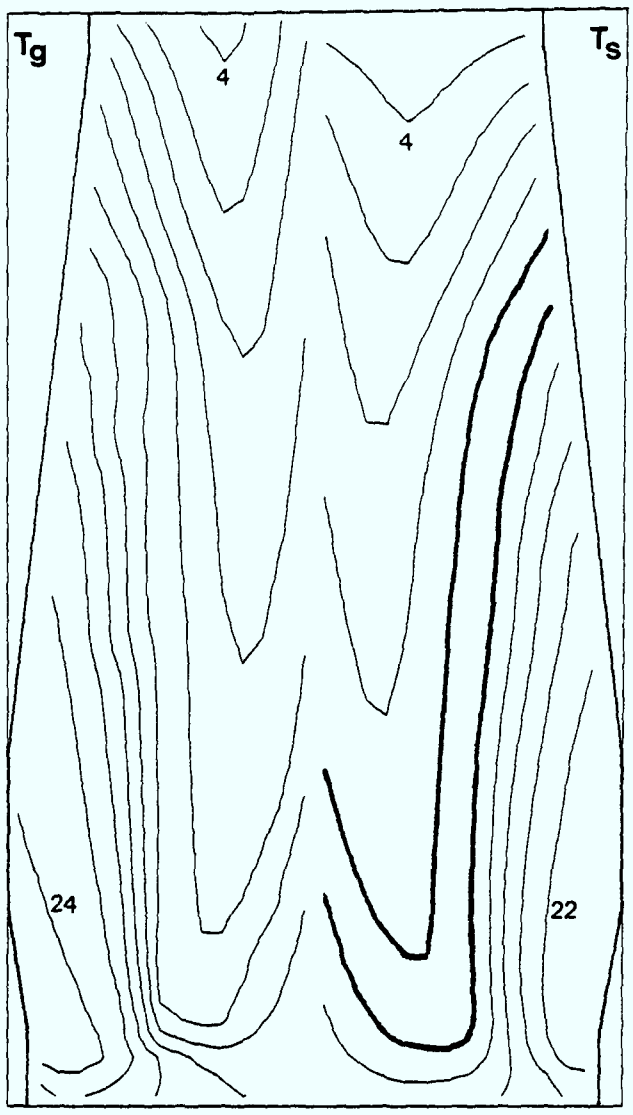

Figure 7.11: Temperature contours(10^2K) raceway A: profile a

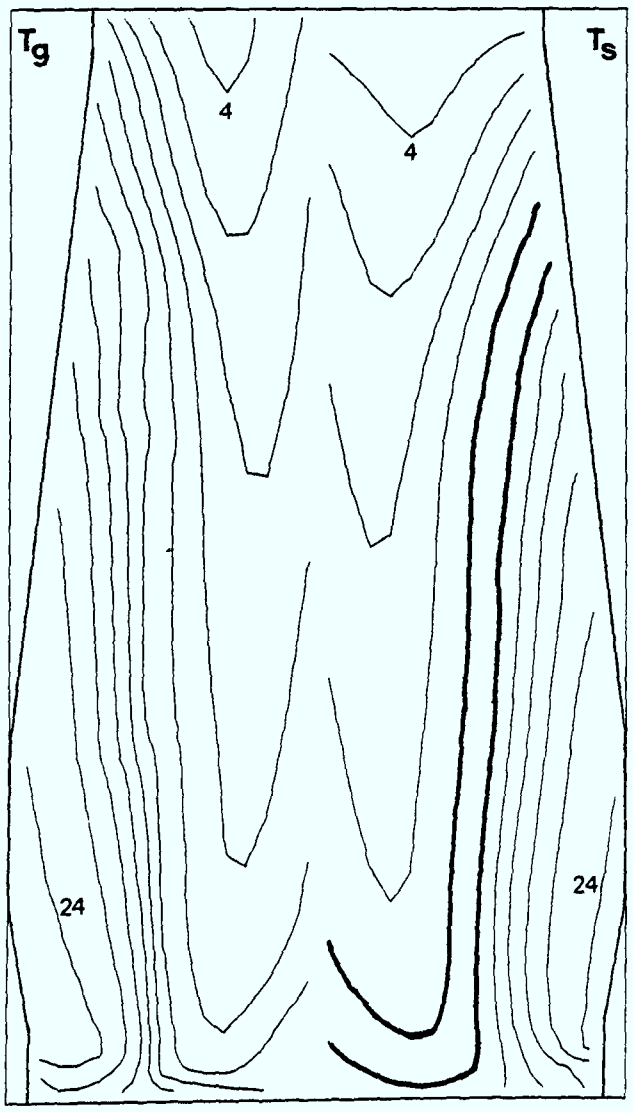

Figure 7.12: Temperature contours(10^2K) raceway A: profile b

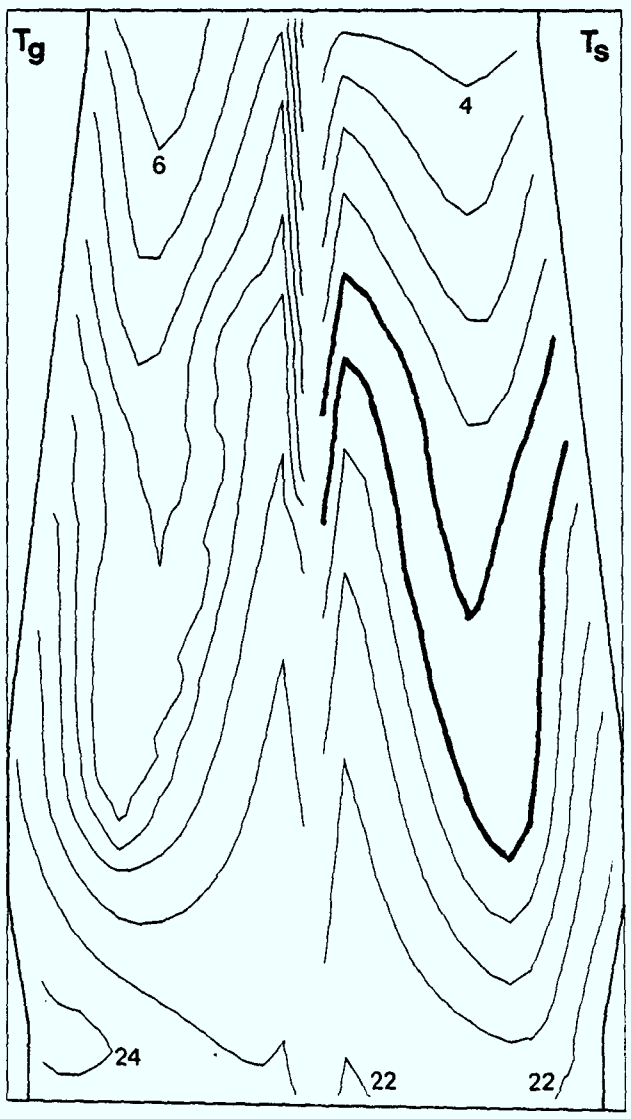

Figure 7.13: Temperature contours(10^2K) raceway A: profile c

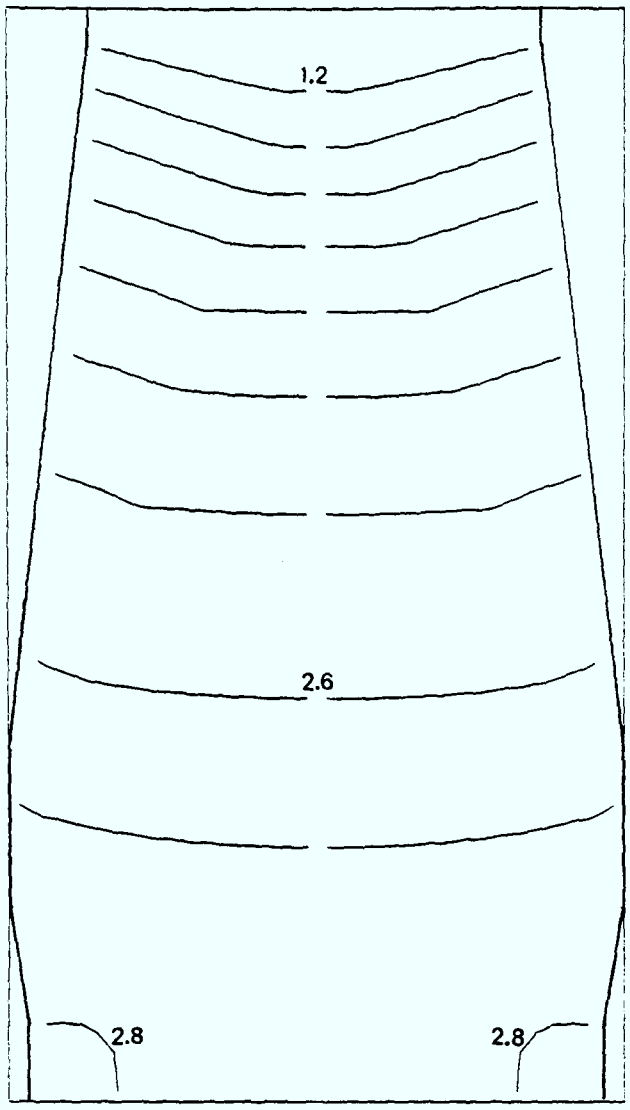

Figure 7.14: Pressure contours(bars) raceway A: std. profile

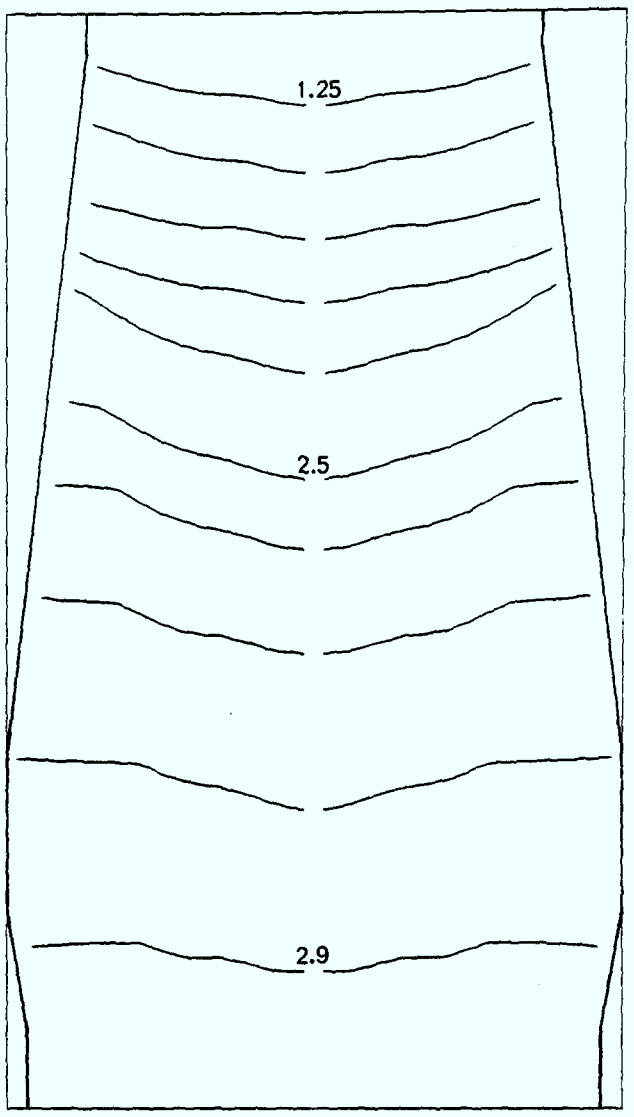

Figure 7.15: Pressure contours(bars) raceway A: profile a

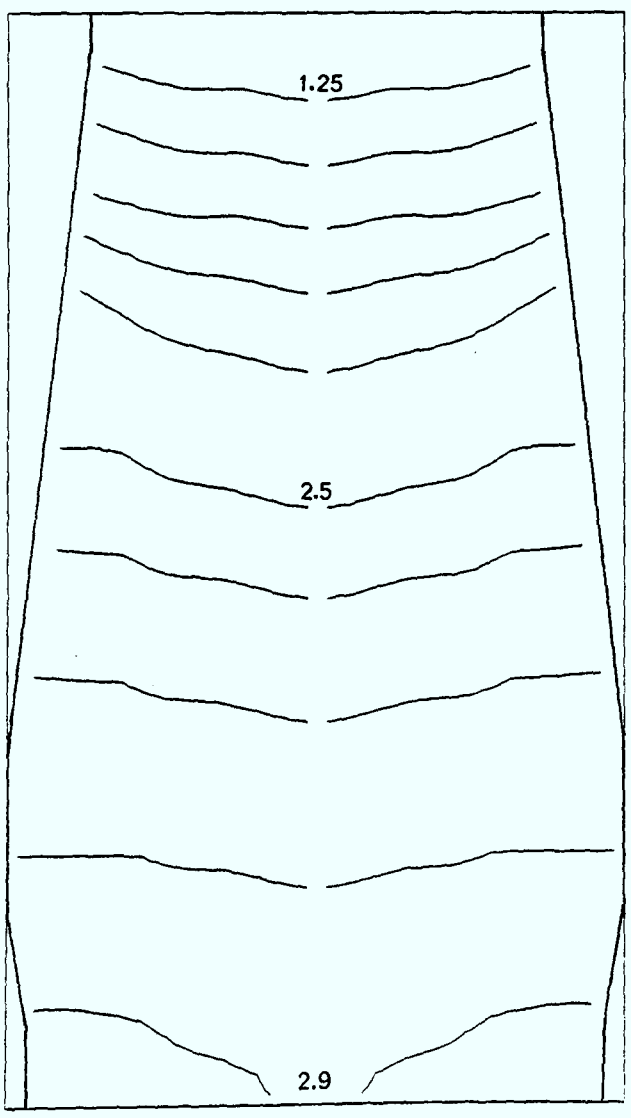

Figure 7.16: Pressure contours(bars) raceway A: profile b

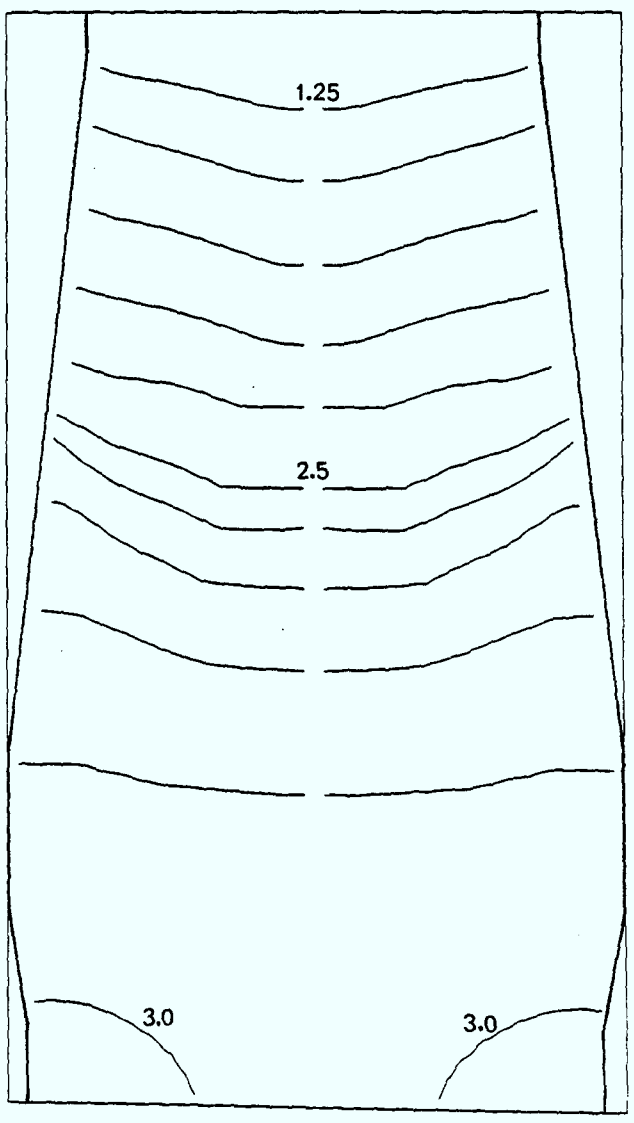

Figure 7.17: Pressure contours(bars) raceway A: profile c

respectively. In the case of the standard profile the changes to the geometry of the cohesive zone are negligible, as can be seen by comparing the contours of Figure (7.1) and Figure (7.10). On comparing the pressure contours of Figure (7.5) and Figure (7.14) it is clear that the gas distributes throughout the furnace in a similar manner. The steeper radial pressure gradient in the immediate vicinity of the raceway shows the presence of the raceway shape A. The overall drop in the axial gradient is accounted for by the reduced resistance to flow. The presence of the raceway reduces the resistance by a small amount and this is reflected by a fairly small reduction in the axial pressure gradient. This effect can be seen in all the cases with raceway shape A, as illustrated by the pressure contours.

In the case of the ore:coke profile (c), the addition of a raceway had a similar effect as in the standard profile case. The position of the cohesive zone altered by a negligible factor, as can be seen by comparing Figure (7.4) with Figure (7.13). Also, the expected changes in the pressure were observed, whereby the radial gradient increased in the vicinity of the raceway and the axial gradient across the furnace increased. The slight increase in the axial pressure gradient is caused by the small increase in the cohesive zone volume at the centre of the furnace, both changes being regarded as negligible.

Both the standard case and profile (c) change very little when adding a raceway. This is caused by the large active coke zone enabling a rapid distribution of gas and therefore reducing the effects of raceway penetration on the cohesive zone.

In the case of the ore:coke profiles (a) and (b), the position of the cohesive zone changes by a small but significant amount. With profile (a), as seen in Figure (7.11) compared to Figure (7.2), the cohesive zone position is lowered along the midway to central portion. The overall axial pressure gradient increases due to an increase in the packed bed resistance. This is caused by the increased volume of stack zone and reduction of active coke, the former having a higher resistance to flow. With profile (b) the cohesive zone is observed to lower axially and shift slightly towards the furnace centre. This gives rise to a decrease in the axial pressure gradient, particularly in the lower part of the furnace. The cause of the pressure decrease is the shifting of the cohesive zone towards the furnace centre, therefore reducing the cohesive volume and resultantly the resistance to flow.

It must be noted that, although the cohesive zone movement was described as a decrease, it should more correctly be described as an elongation. While the lower part of the cohesive zone did descend, the cohesive region at the furnace periphery retained its position. With a lower central region of the cohesive zone, the flow distribution is increased along the periphery due to the increased resistance to radial flow. With the flow distribution towards the furnace wall, the thermal energy transfer is reduced in the lower central regions thus lowering the cohesive position.

On reflection of the results, using raceway shape A, the significant point to note is the minor effect of raceway penetration on the cohesive zone's position. When the active coke zone is fairly large, thereby positioning the cohesive zone high in the furnace, the effects of raceway penetration are negligible. It must be noted

that each model run was performed from the same starting position, which itself was totally different to any results obtained. This eliminated the possibility of a previous set of results influencing the next run to at an inaccurate solution.

The second set of results were generated with raceway shape B. This raceway was designed to perform an initial study on the effects of growth in the vertical direction, on the complete furnace system. Again, the set of results involved varying the ore:coke charging profile as in the set of results with raceway A. The temperature contours for; the standard, (a),(b) and (c) profiles are shown in Figures (7.18) to (7.21) respectively, together with their respective pressure contours in Figures (7.22) to (7.25). In keeping with the conclusions made above, the cohesive zone position did not change in the cases with the standard and (c) profiles. This can be observed by their temperature contours, shown in Figures (7.18) and (7.21), when compared to the corresponding contours of the previous runs. No change in the flow distribution is confirmed by the pressure contours of Figures (7.22) and (7.25), again when compared to the corresponding contours of previous runs.

The results for profiles (a) and (b) did show a change from the previous sets of runs (ie. no raceway shape and raceway A). The effect of raceway A was to encourage a greater flow distribution along the furnace periphery; the addition of height to the raceway (ie shape B) has accentuated this effect thereby strengthening conclusions. The temperature contours for profiles (a) and (b), with the second shape, are shown in Figures (7.19) and (7.20). The preferential flow towards the walls reduces the thermal energy transfer in the lower central regions, as shown in the temperature

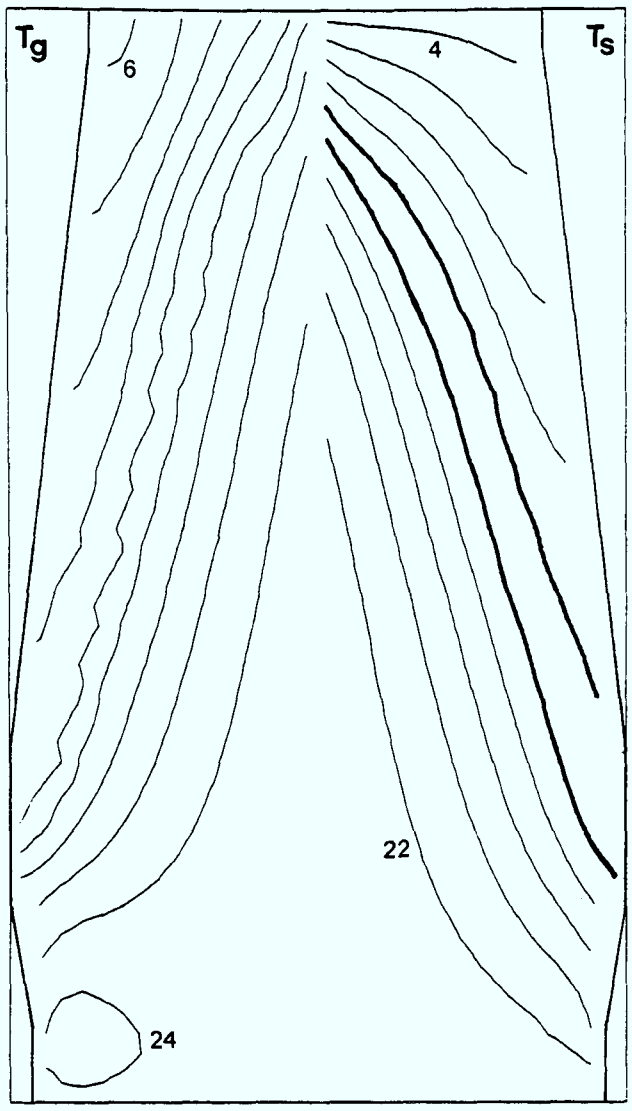

Figure 7.18: Temperature contours(10^2K) raceway B: std. profile

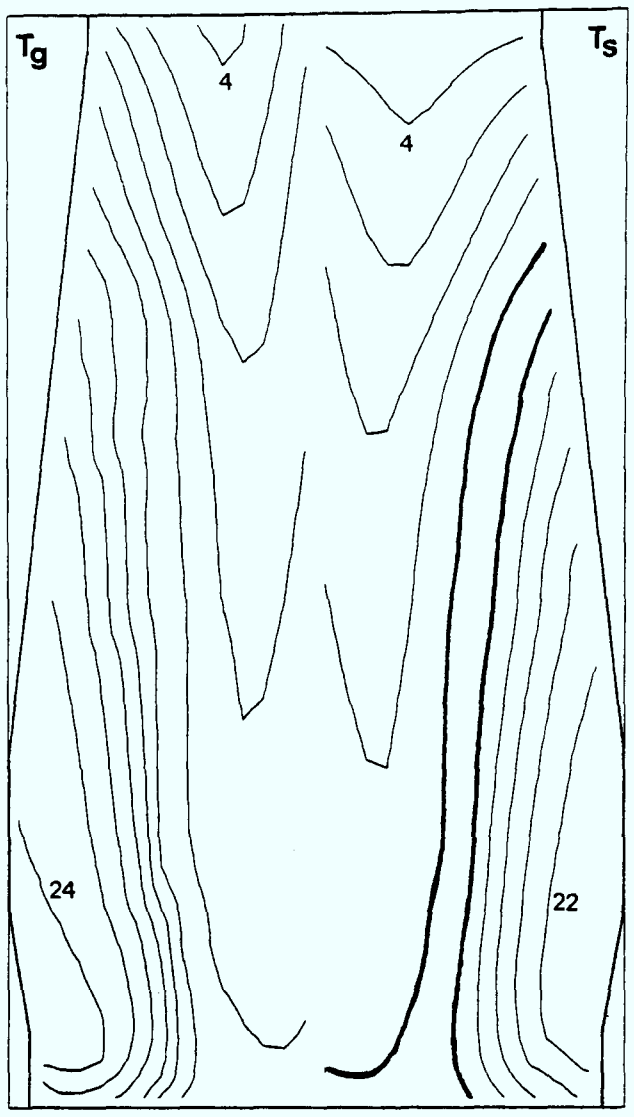

Figure 7.19: Temperature contours(10^2K) raceway B: profile a

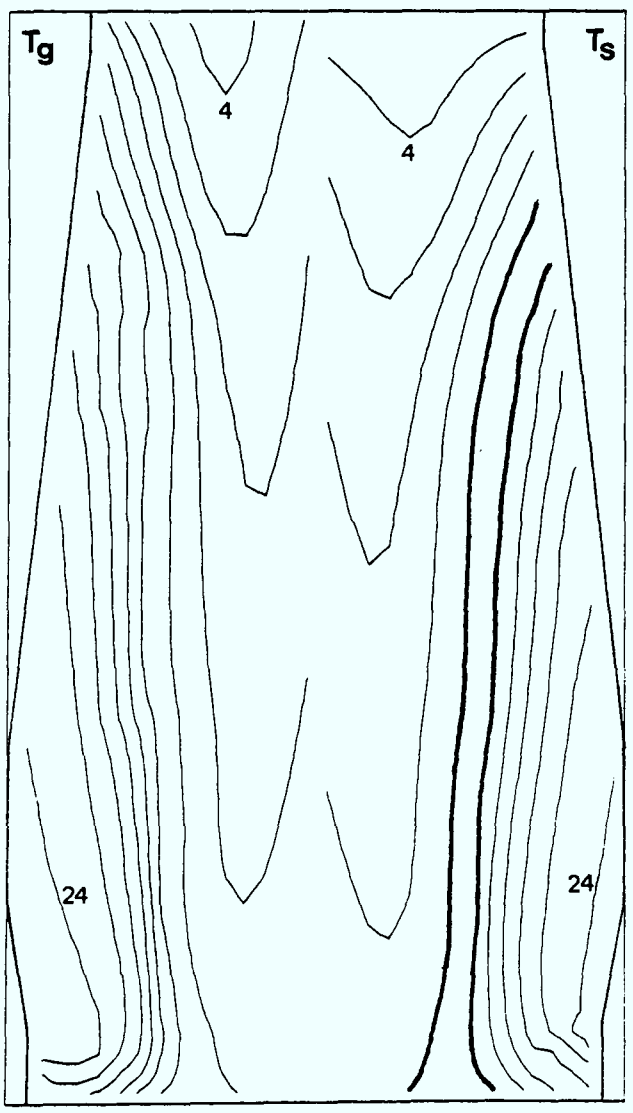

Figure 7.20: Temperature contours(10^2K) raceway B: profile b

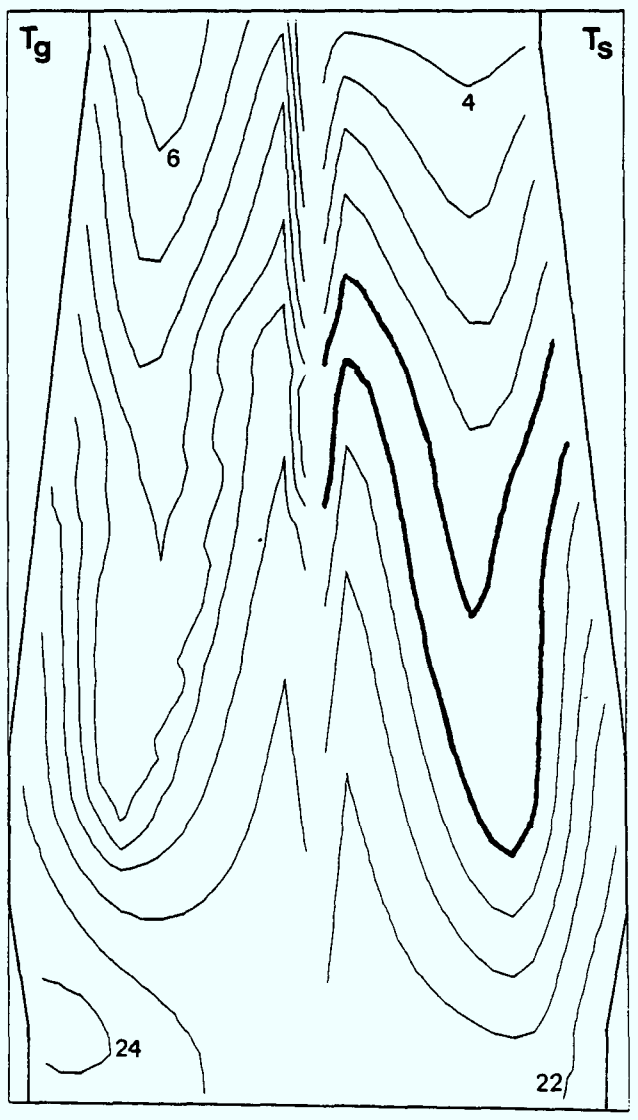

Figure 7.21: Temperature contours(10^2K) raceway B: profile c

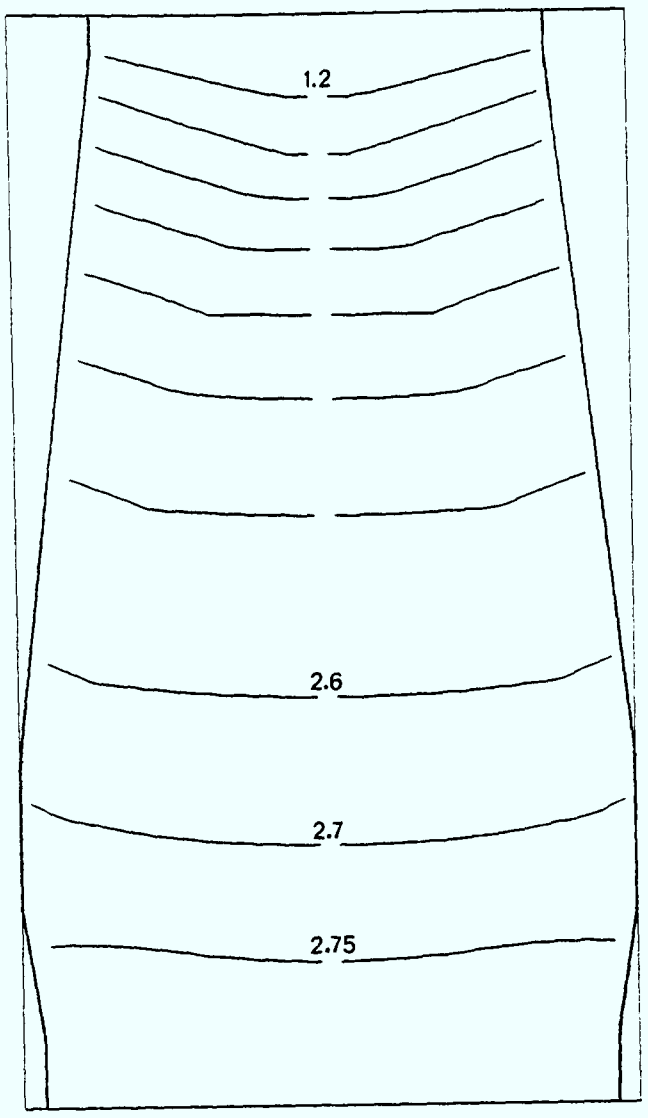

Figure 7.22: Pressure contours(bars)
raceway B: std. profile

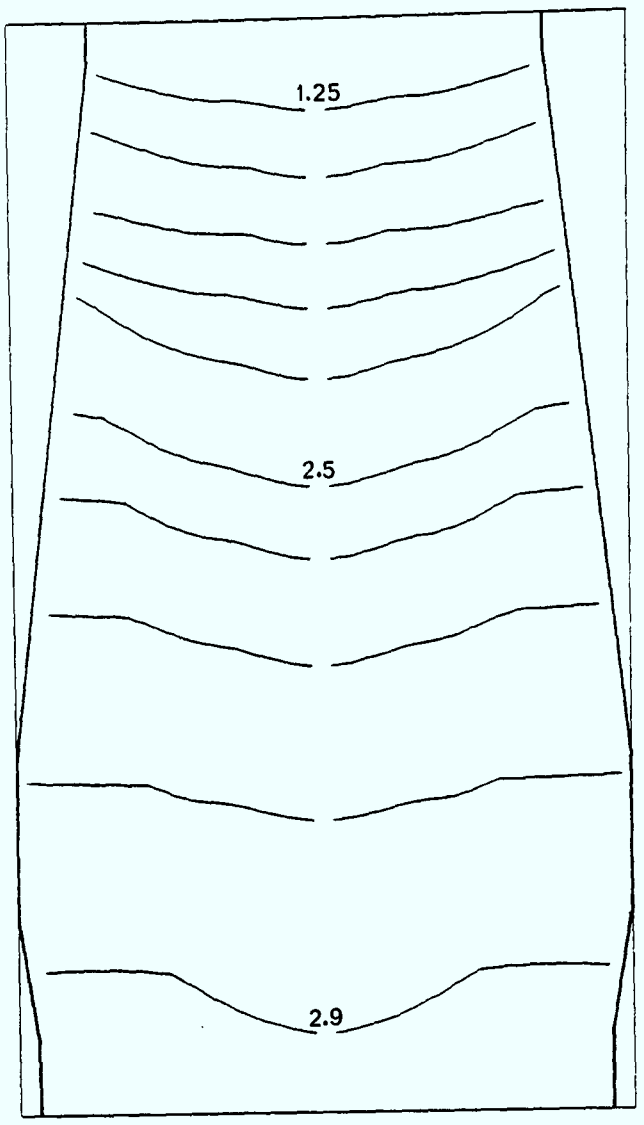

Figure 7.23: Pressure contours(bars)
raceway B: profile a

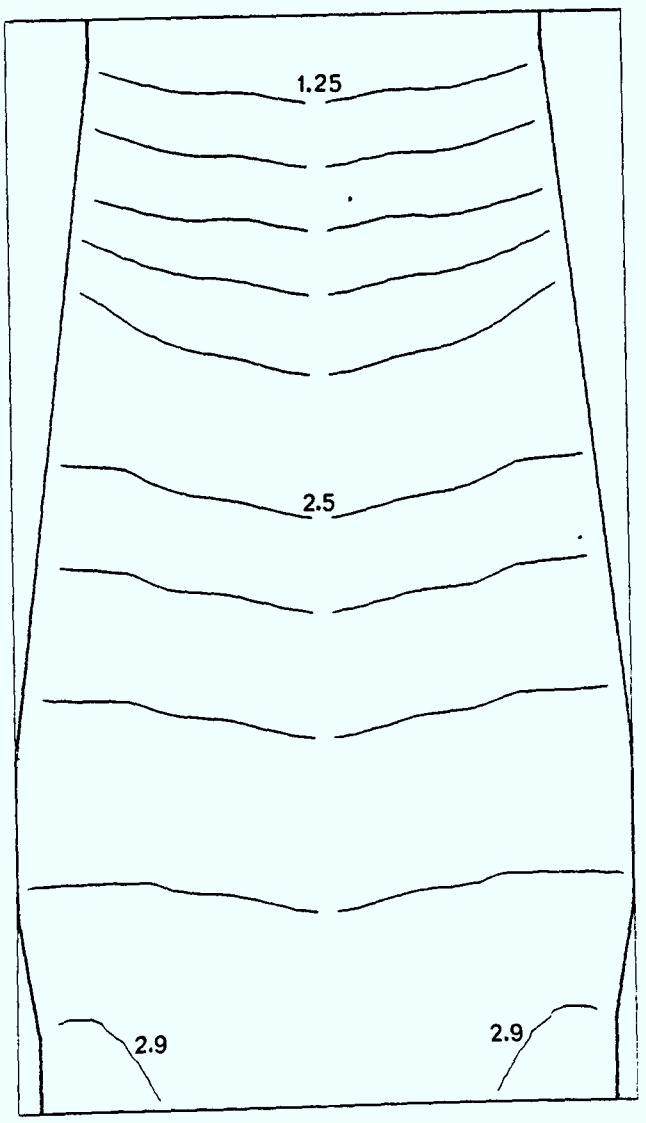

Figure 7.24: Pressure contours(bars)
raceway B: profile b

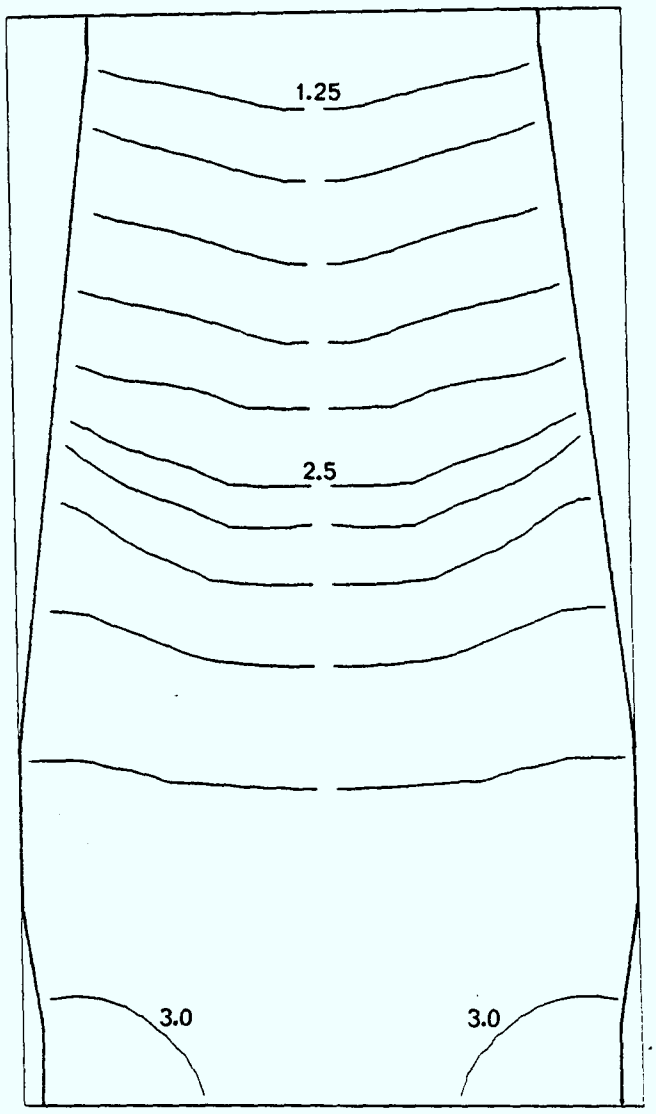

Figure 7.25: Pressure contours(bars)
raceway B: profile c

contours. The changed cohesive zone shape has induced a higher resistance in front of the raceway which assists a vertical flow distribution. Both corresponding pressure gradients, in the axial direction (shown in Figures (7.23) and (7.24)), are reduced due to the effective reduction in cohesive volume reducing resistance to flow.

The two sets of runs, comparing raceway shapes A and B against no raceway, have brought to light important facts about the role of the raceway. The results fell into two categories: those where the cohesive mass was located in the vicinity of the raceway, and those where the aforementioned vicinity was largely active coke. Profiles (a) and (b) provided the former results and the standard and (c) profiles provided the latter. It is clear from these results that the raceway shape only affects the gas distribution in the local vicinity.

7.4 Charging Angle and Blast Rate

The importance of resistance to gas flow has been made clear by the results of ore:coke profile changes. As the resistances are calculated in directional components, it was of interest to see if a change in the directional resistances affected the behaviour of the raceway role in the furnace. These changes were brought about by altering the charging angle and observing the effects.

It was of secondary importance to confirm predictive changes in furnace behaviour, for the sake of reassurance that the mathematical model behaved accordingly. This was achieved with a number of runs where a single blast rate change was exercised on both raceway shapes against two profiles each. Not only were these runs

performed to assist the models validity but also to show the sensitivity of the location of the cohesive zone to the gas blast rate.

7.4.1 Charging angle

The changes to charging angle were performed via two sets of runs. The standard charging angle used so far has been 30°, therefore it was decided to use two angles, 50% above and below the standard. This yielded the two test sets of 45° and 15°. It must be noted that the 45° angle exceeds the optimum charging angle and was therefore only used to test for expected changes in the model rather than test for physical properties. The temperature and pressure contours for the various combinations of angle, profile and raceway shape are given by the figure numbers laid down in Table (7.1).

The angle of inclination of the charged burden plays a dominant role in the directional resistances to flow. This can be seen in the mathematical model, in equation (4.10), where the matrix $\underline{\underline{H}}$, of relationship (4.11), is highly sensitive to angle. On identifying that in the furnace, the resistance along a layer, f_x, is smaller than that across layers, f_y, it can be seen on analysis of the matrix $\underline{\underline{H}}$ that a decrease in angle should increase the axial pressure gradient and decrease the radial gradient. Similarly an angle increase should have the opposite effects on the axial and radial gradients. Results were compared against those of section 7.3.

The first set of results, decreasing the loading angle to 15°, had this expected effect. The pressure contours of the two raceways

	Profile	Contour	Raceway A	Raceway B
15°	std.	temp.	(7·26)	(7·28)
charging		pressure	(7·30)	(7·32)
angle				
	a	temp.	(7·27)	(7·29)
		pressure	(7·31)	(7·33)
45°	std.	temp.	(7·34)	(7·36)
charging		pressure	(7·38)	(7·40)
angle				
	a	temp.	(7·35)	(7·37)
		pressure	(7·39)	(7·41)

Table 7.1: Figure numbers corresponding to analysis of charging angle.

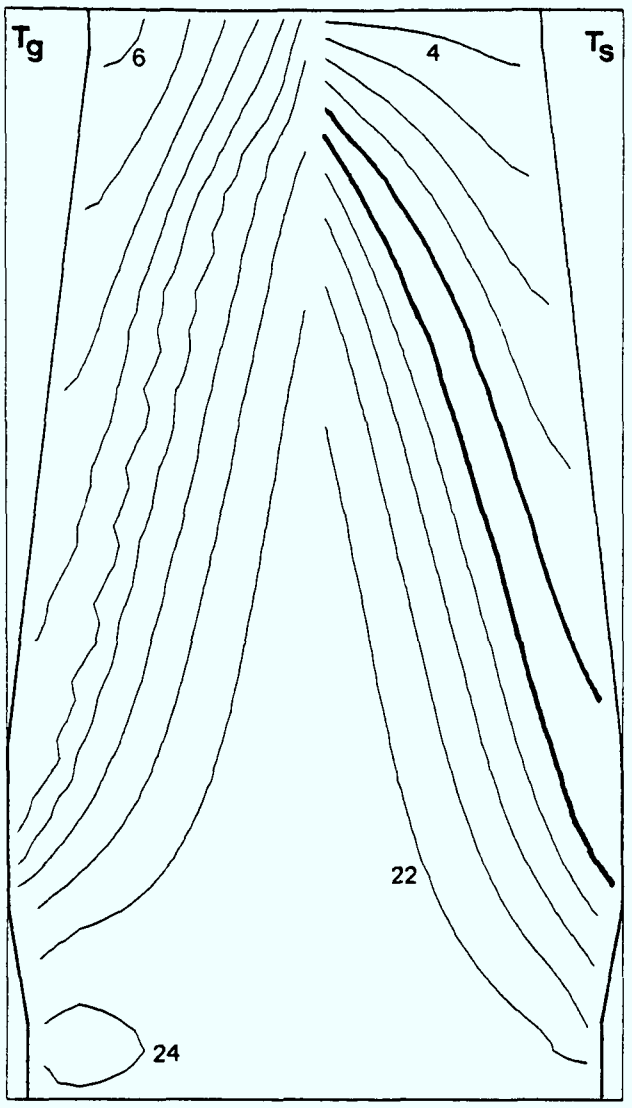

Figure 7.26: Temperature contours(10^2K)
15°:rwA: std. profile

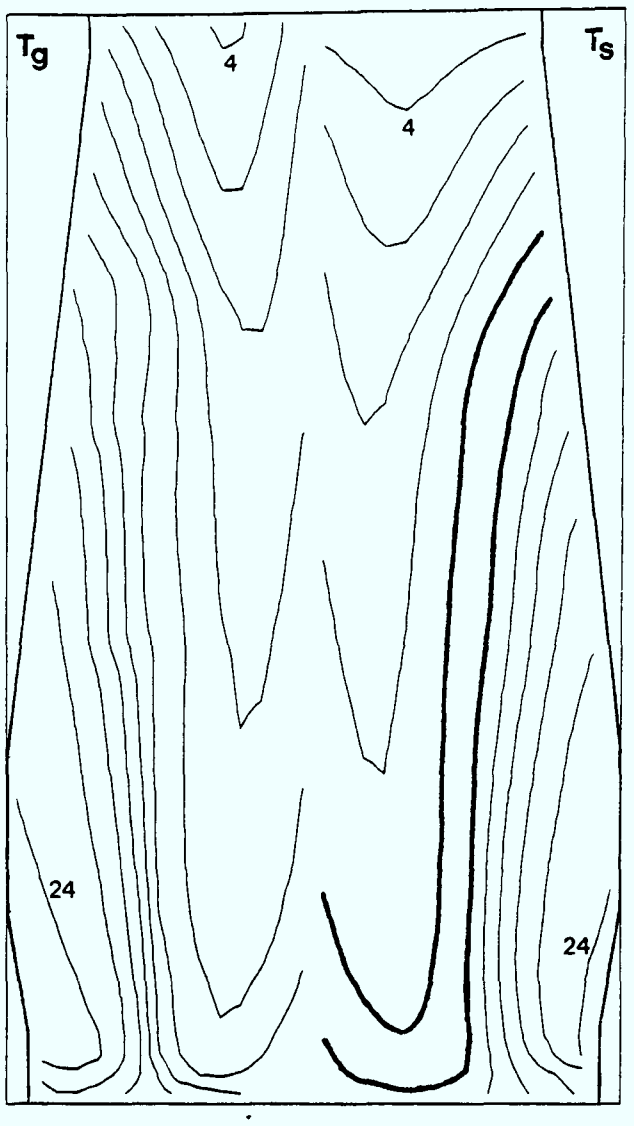

Figure 7.27: Temperature contours(10^2K)
15°:rwA: profile a

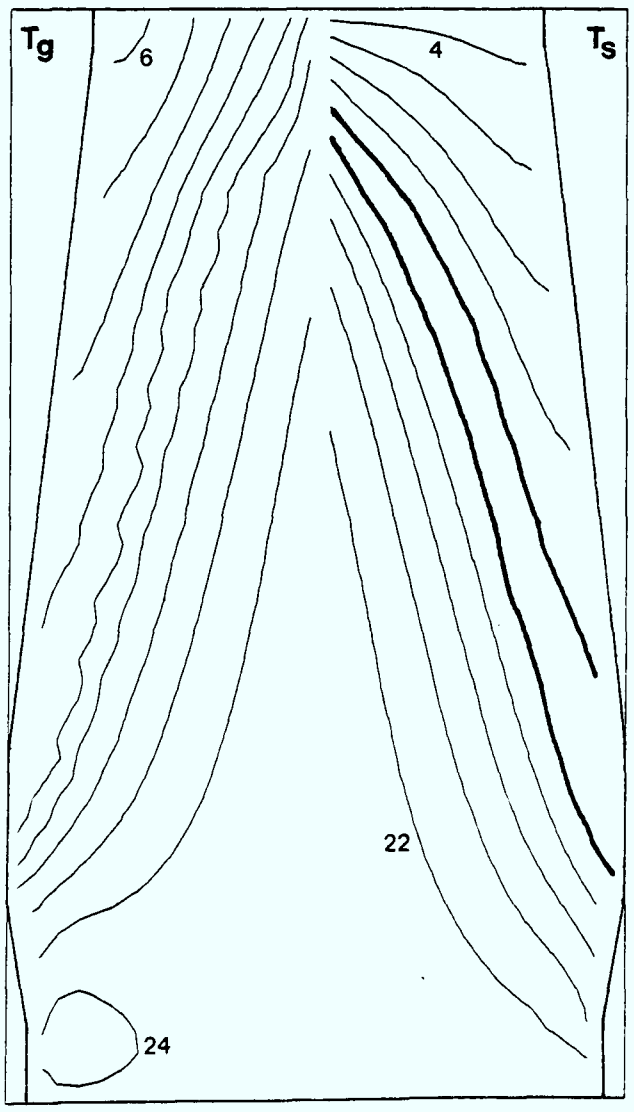

Figure 7.28: Temperature contours(10^2K)
15°:rwB: std. profile

Figure 7.29: Temperature contours(10^2K)
15°:rwB: profile a

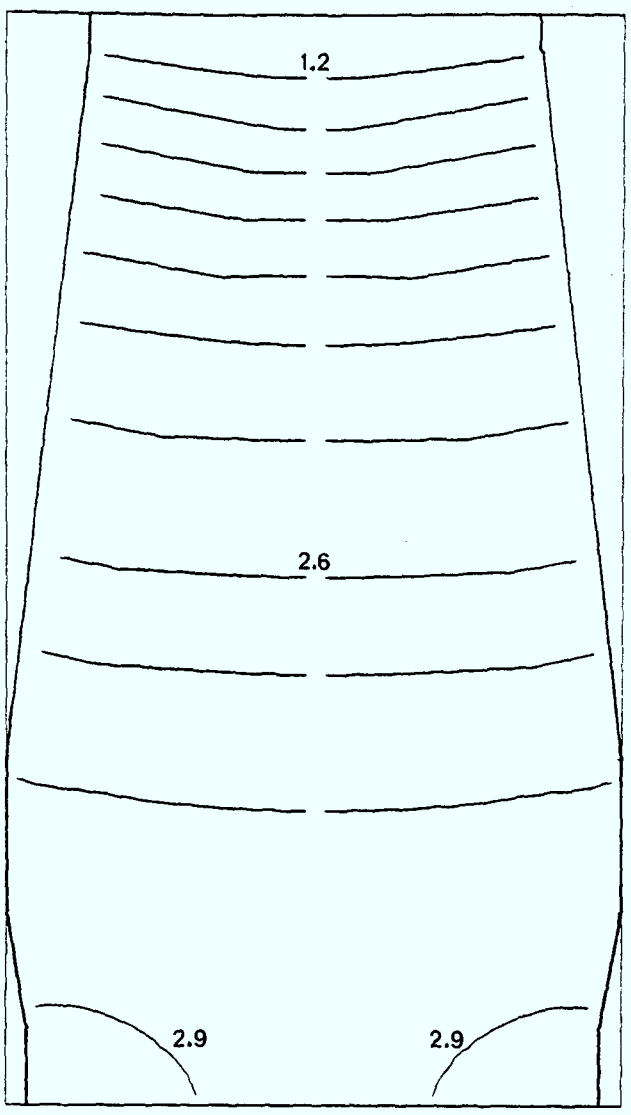

Figure 7.30: Pressure contours(bars)
15°:rwA: std. profile

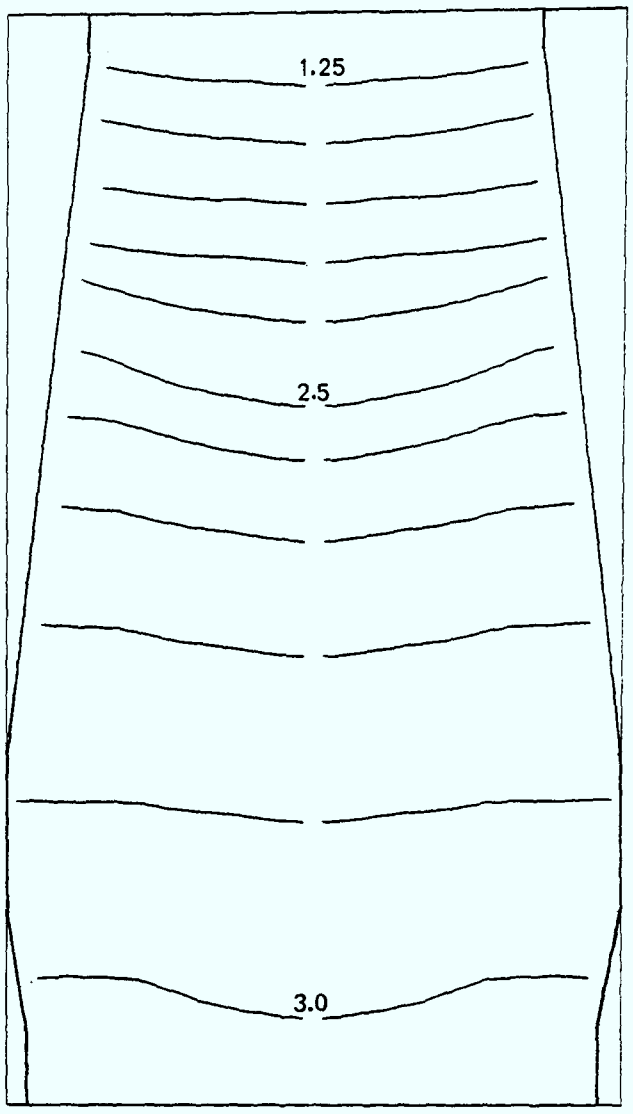

Figure 7.31: Pressure contours(bars)
15°:rwA: profile a

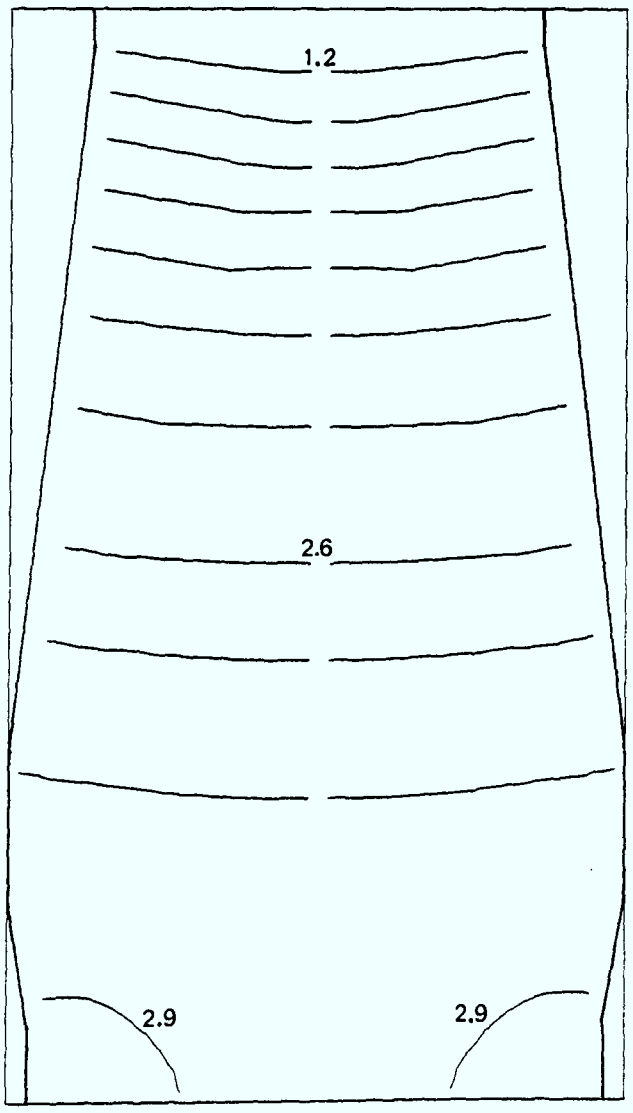

Figure 7.32: Pressure contours(bars)
15°:rwB: std. profile

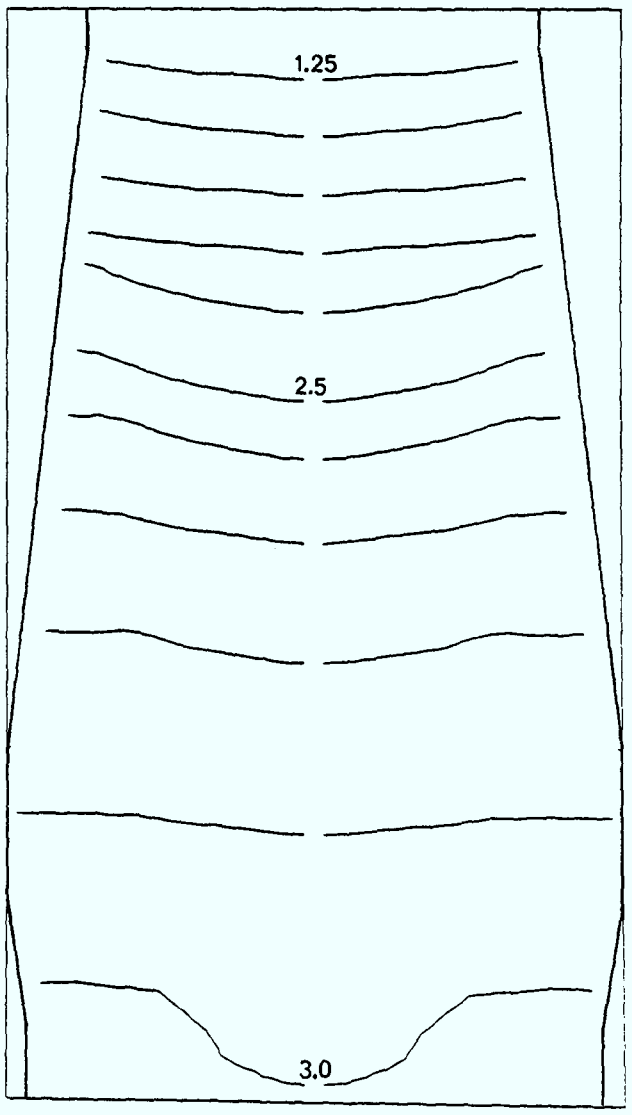

Figure 7.33: Pressure contours(bars)
15°:rwB: profile a

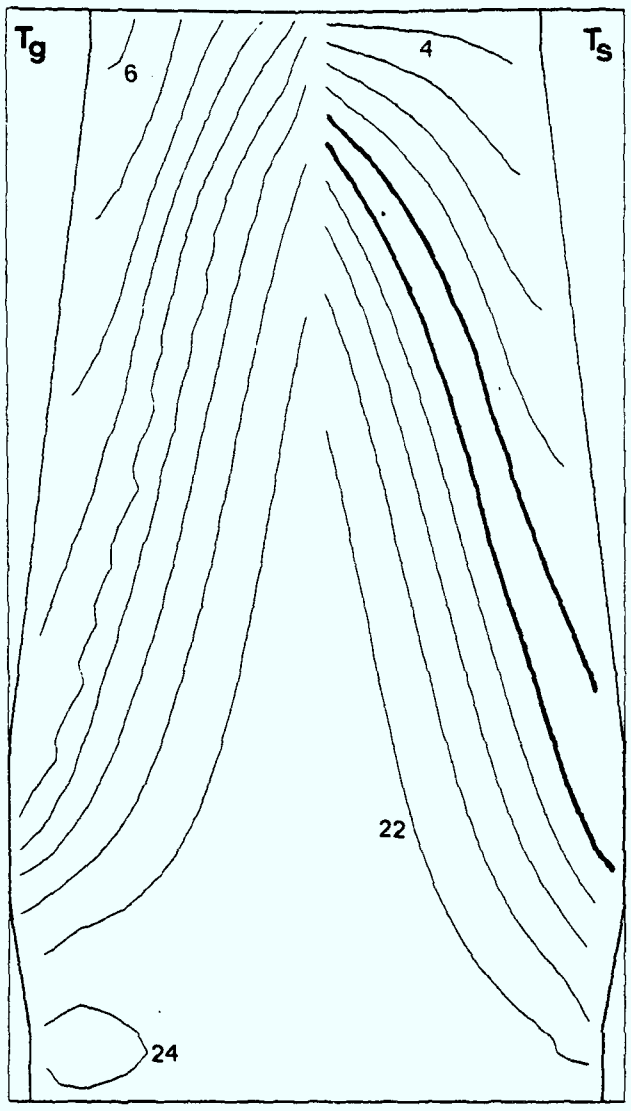

Figure 7.34: Temperature contours(10^2K)
45°:rwA: std. profile

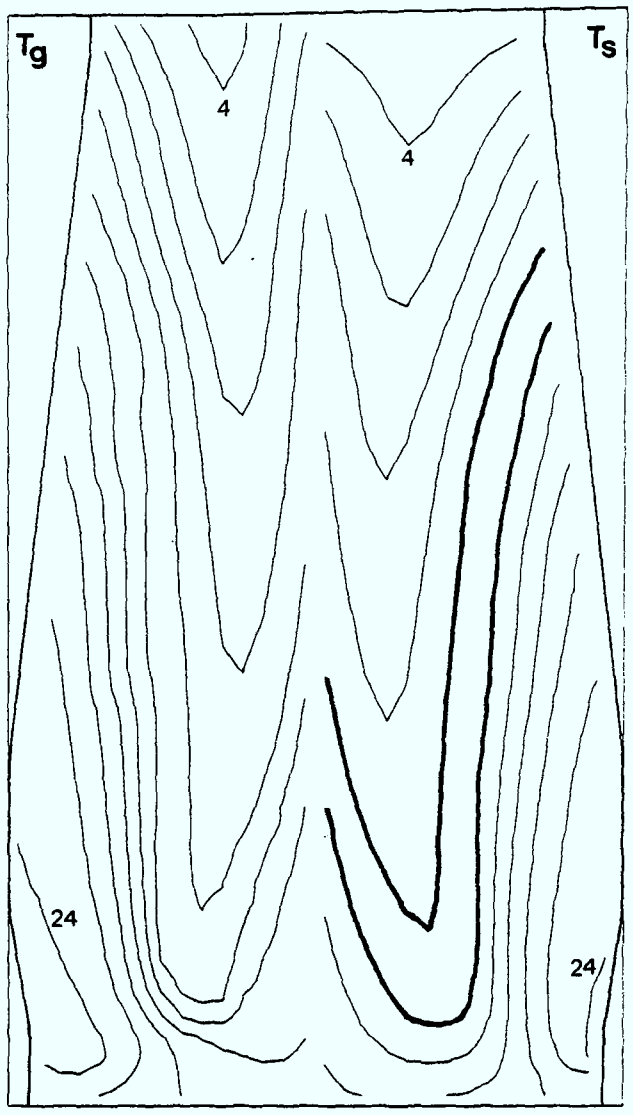

Figure 7.35: Temperature contours(10^2K)
45°:rwA: profile a

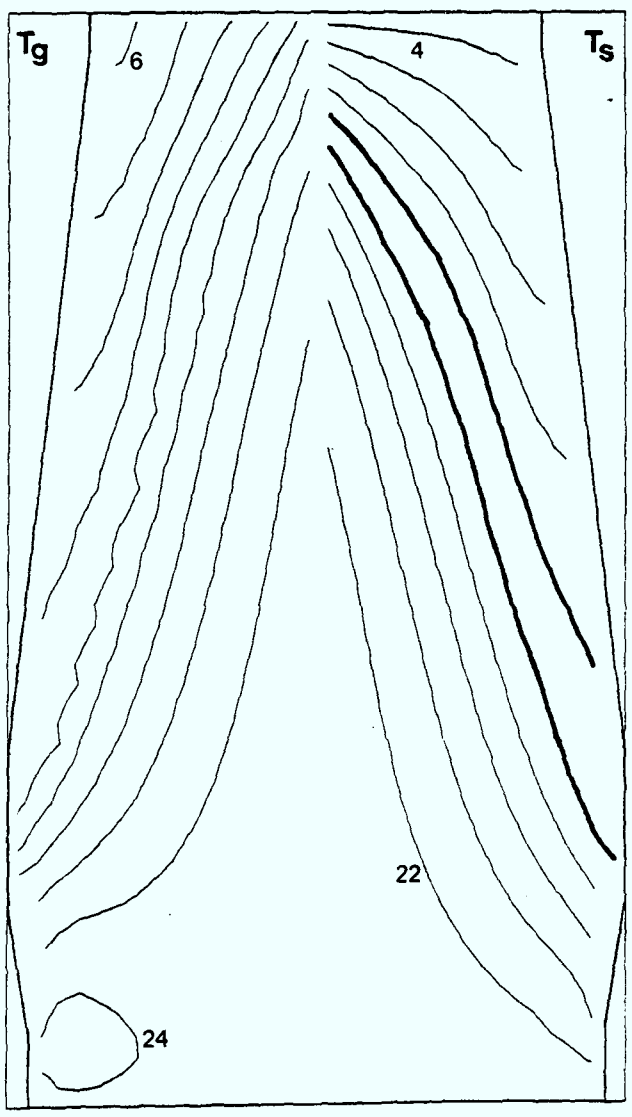

Figure 7.36: Temperature contours(10^2K)
45°:rwB: std. profile

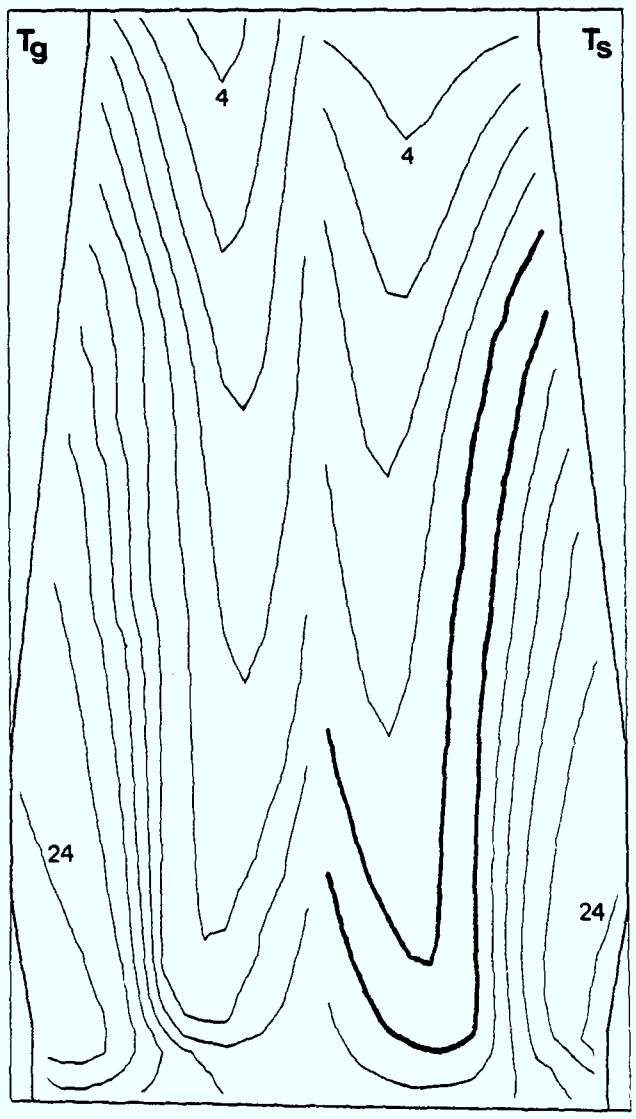

Figure 7.37: Temperature contours(10^2K)
45°:rwB: profile a

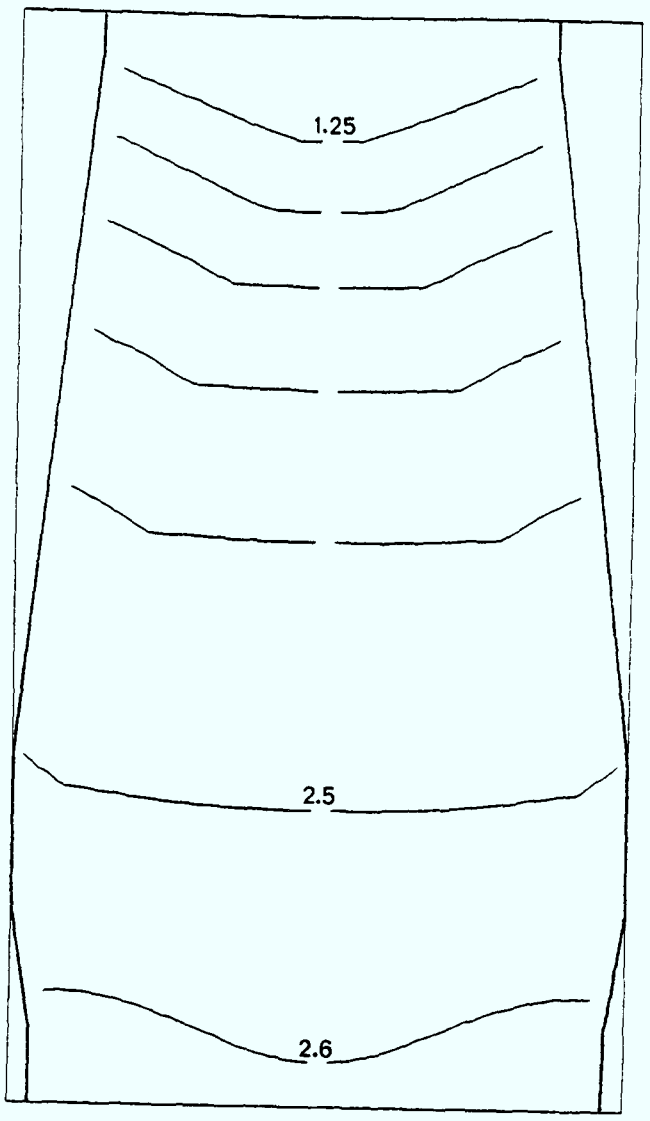

Figure 7.38: Pressure contours(bars)
45°:rwA: std. profile

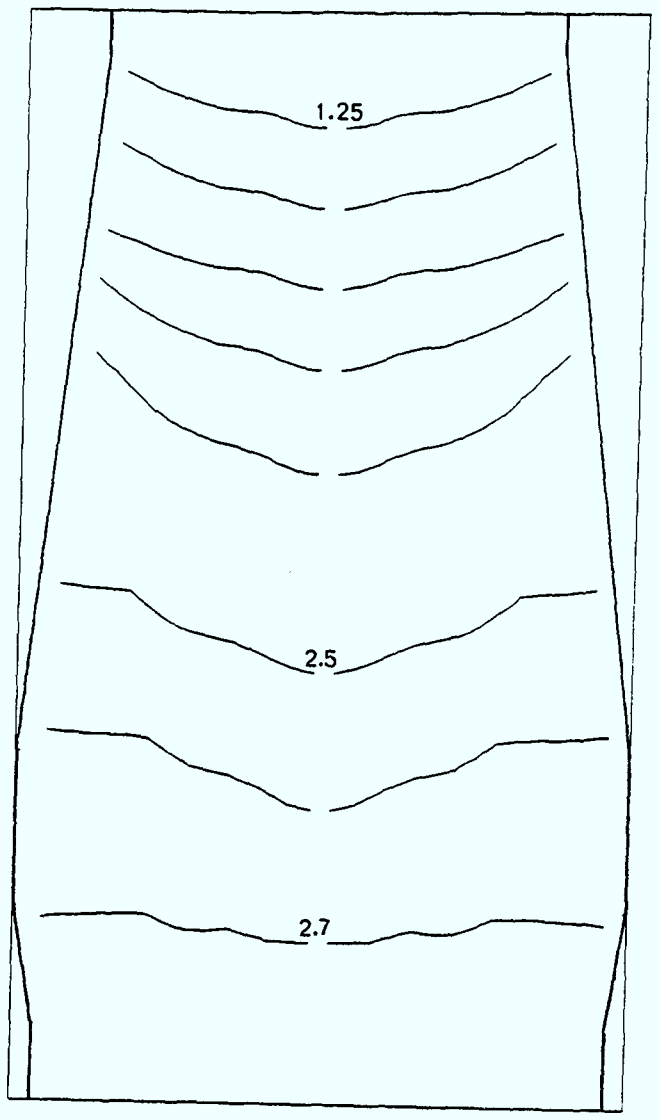

Figure 7.39: Pressure contours(bars)
45°:rwA: profile a

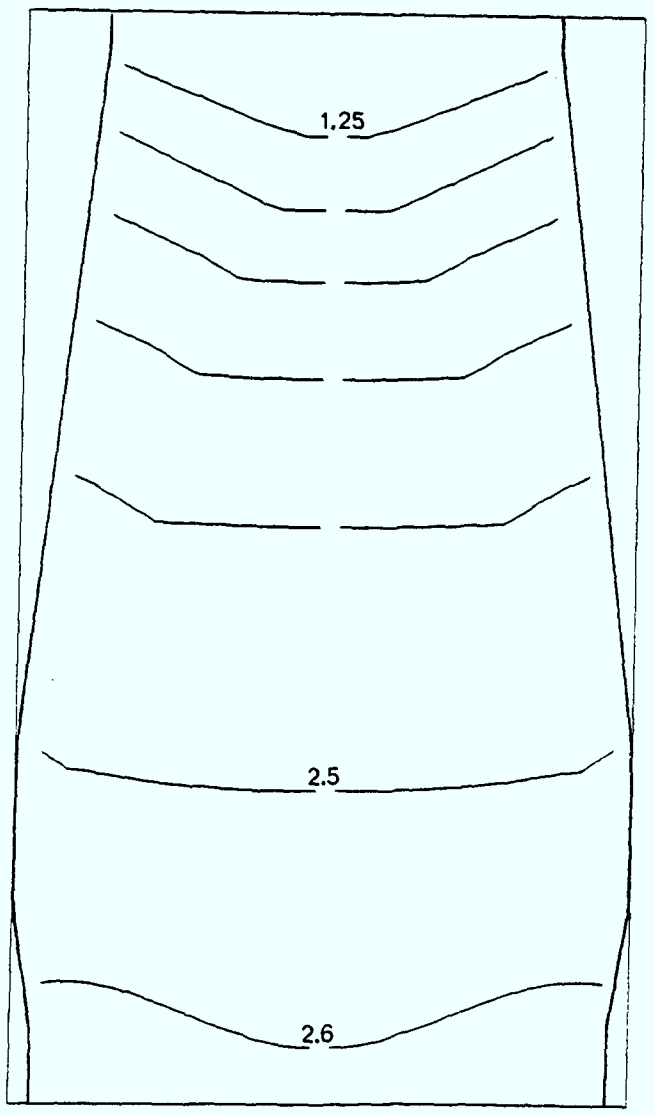

Figure 7.40: Pressure contours(bars)
45°:rwB: std. profile

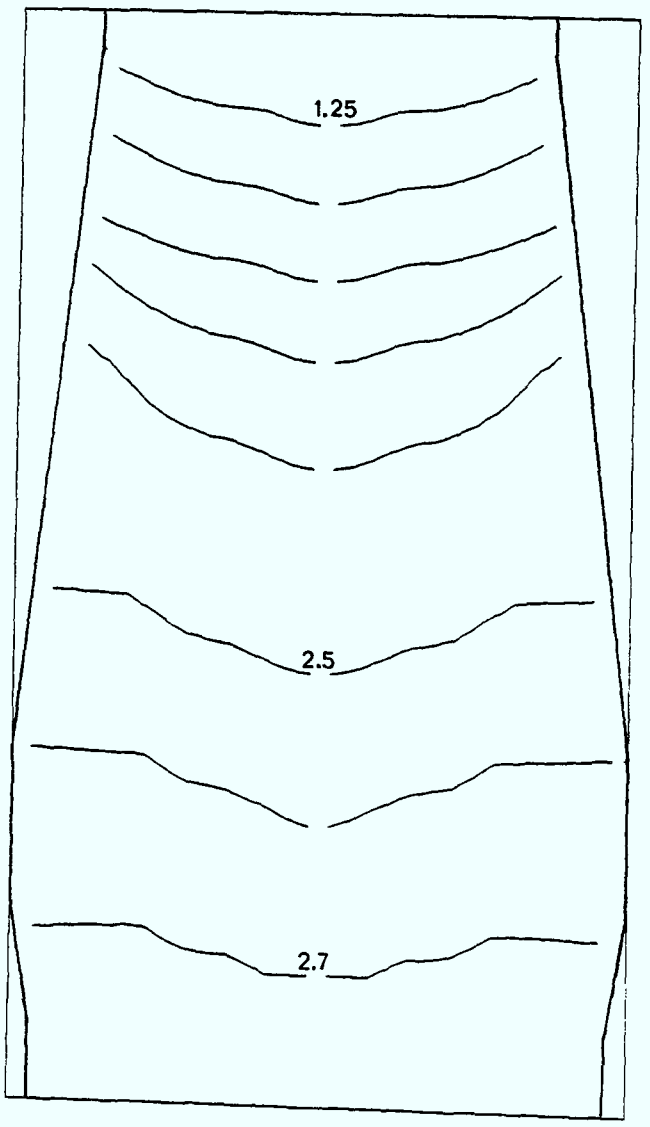

Figure 7.41: Pressure contours(bars)
45°:rwB: profile a

7.4.2 Blast rate

The gas blast rate was altered, by a reduction of 20%, to confirm the mathematical model behaved in a predicted manner. With this reduction in blast, four tests were performed by changing raceway shape and ore:coke charging profile. The figure numbers corresponding to the temperature and pressure contours for the two raceways and profiles are given in Table (7.2). Comparison is made with the results of section 7.3.

As expected the cohesive zones in all the runs were significantly lower in the furnace. This is clearly due to the reduced blast lowering the thermal energy transfer to the solids. The temperature contours of the runs, Figures (7.42) to (7.45), demonstrate the new cohesive position. Also due to the reduced blast, an obvious result is the significant decrease in the axial pressure gradient. The radial gradient however remaining approximately the same in the stack zone due to the unchanged charging angle. The pressure contours, as laid down in Table (7.2), are shown in Figures (7.46) to (7.49).

This expected set of results assists the validity of the model by showing predictable behaviour of the cohesive zone. The sensitivity of the cohesive zone's position to the blast rate is made clear. This is not such a startling result as clearly the thermal energy transfer is a direct consequence of the blast rate and its incoming temperature.

7.5 Deadman

It became apparent, late in the analysis, that the deadman (or stagnant coke zone) would have an effect on furnace behaviour

Profile	Contour	Raceway A	Raceway B
std.	temp.	(7·42)	(7·44)
	pressure	(7·46)	(7·48)
a	temp.	(7·43)	(7·45)
	pressure	(7·47)	(7·49)

Table 7.2: Figure numbers corresponding to analysis with reduced blast.

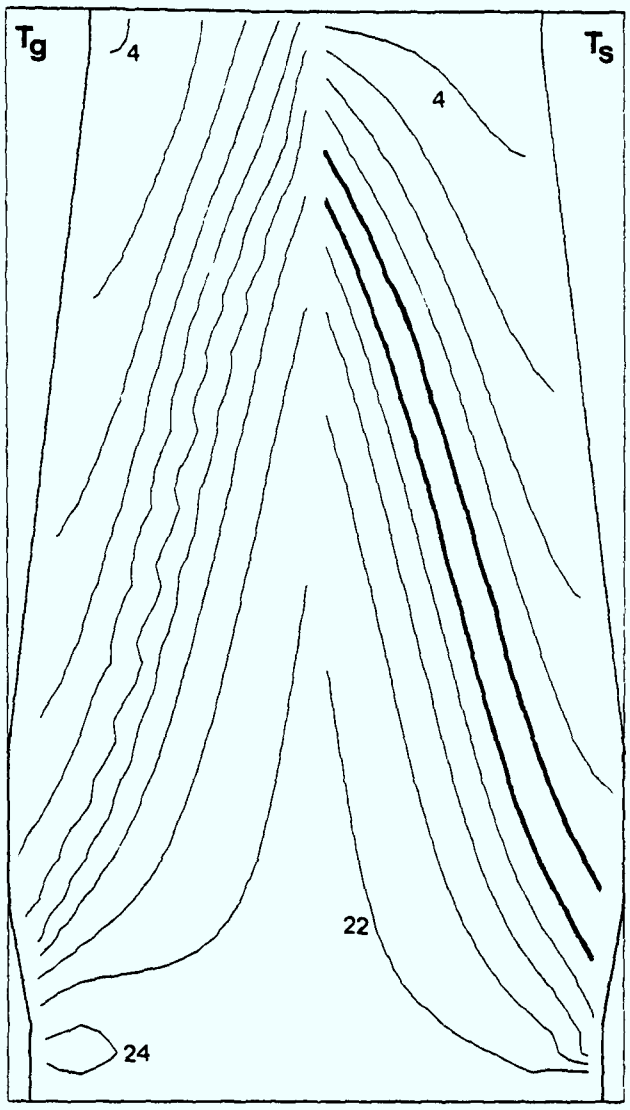

Figure 7.42: Temperature contours(10^2K)
-20%:rwA: std. profile

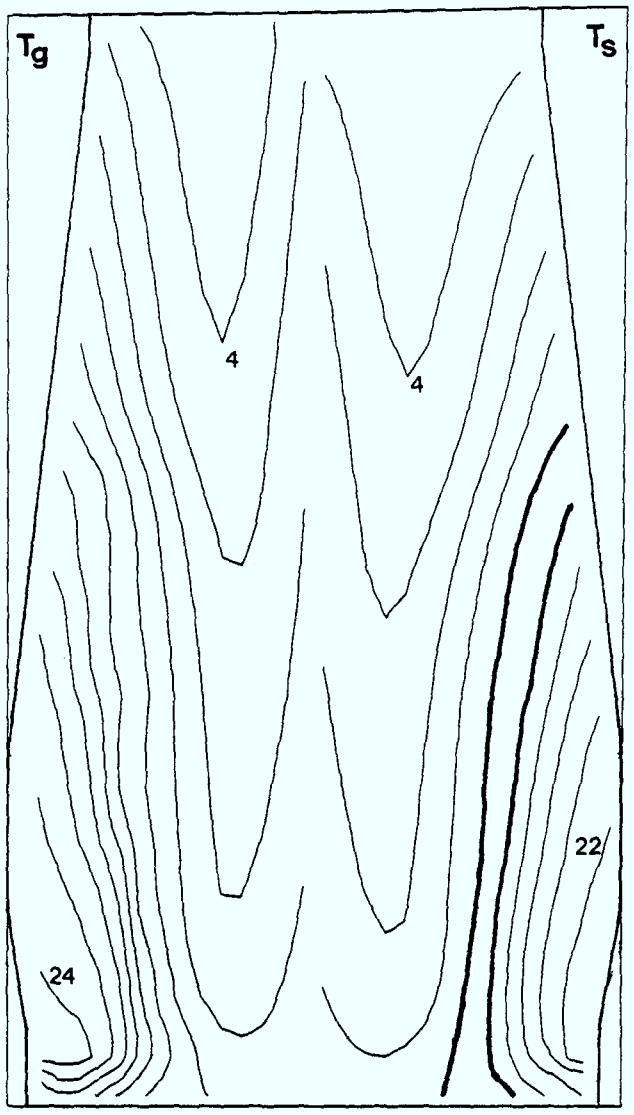

Figure 7.43: Temperature contours(10^2K)
-20%:rwA: profile a

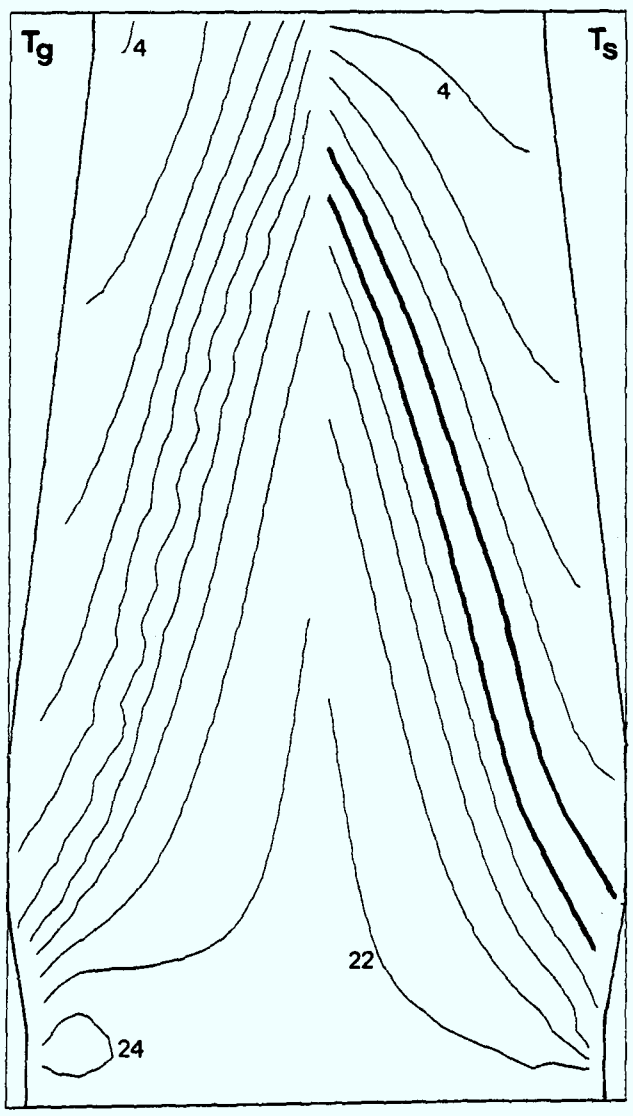

Figure 7.44: Temperature contours(10^2K)
-20%:rwB: std. profile

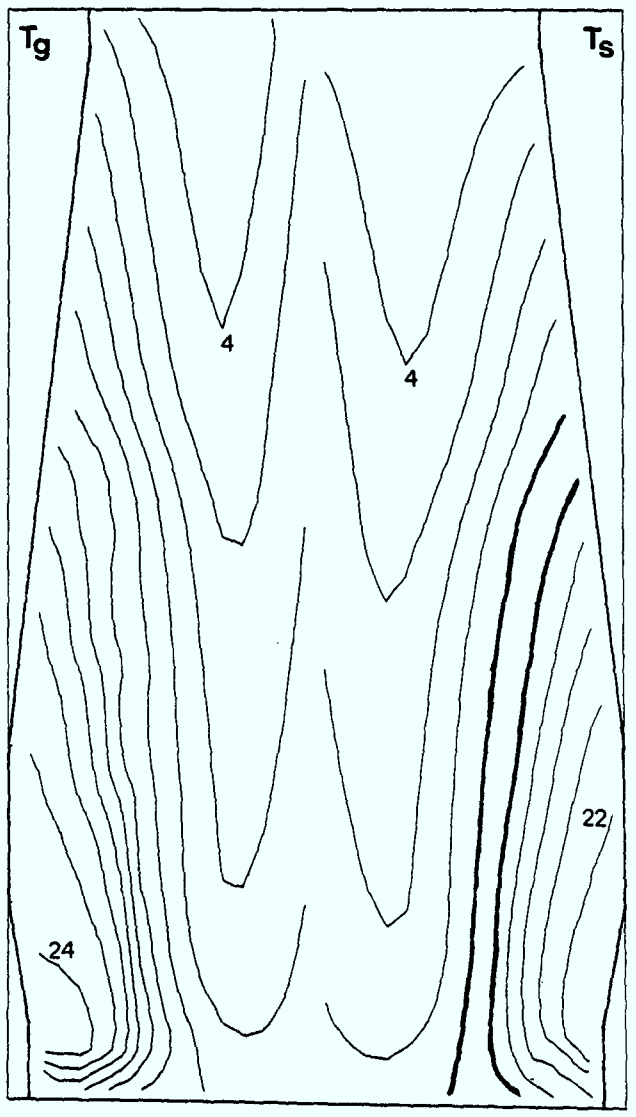

Figure 7.45: Temperature contours(10^2K)
-20%:rwB: profile a

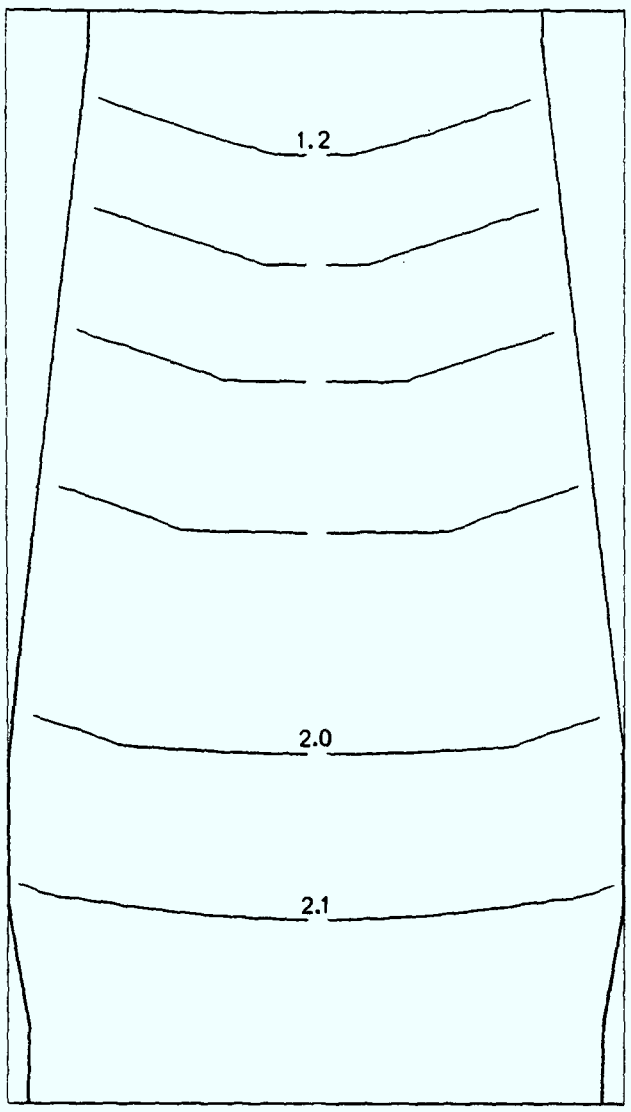

Figure 7.46: Pressure contours(bars)
-20%:rwA: std. profile

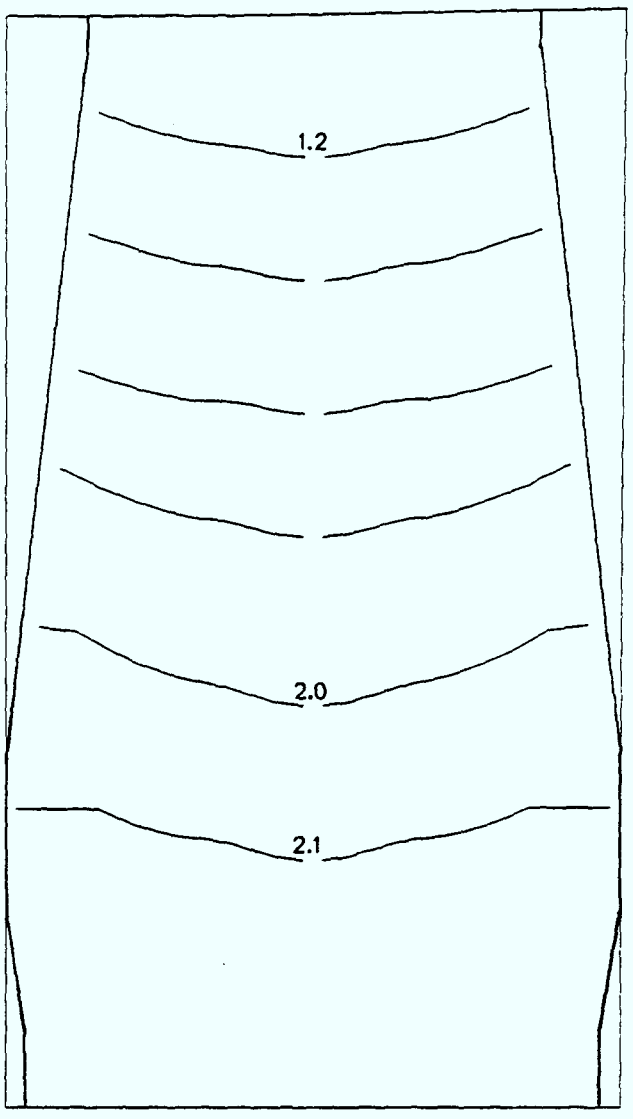

Figure 7.47: Pressure contours(bars)
-20%:rwA: profile a

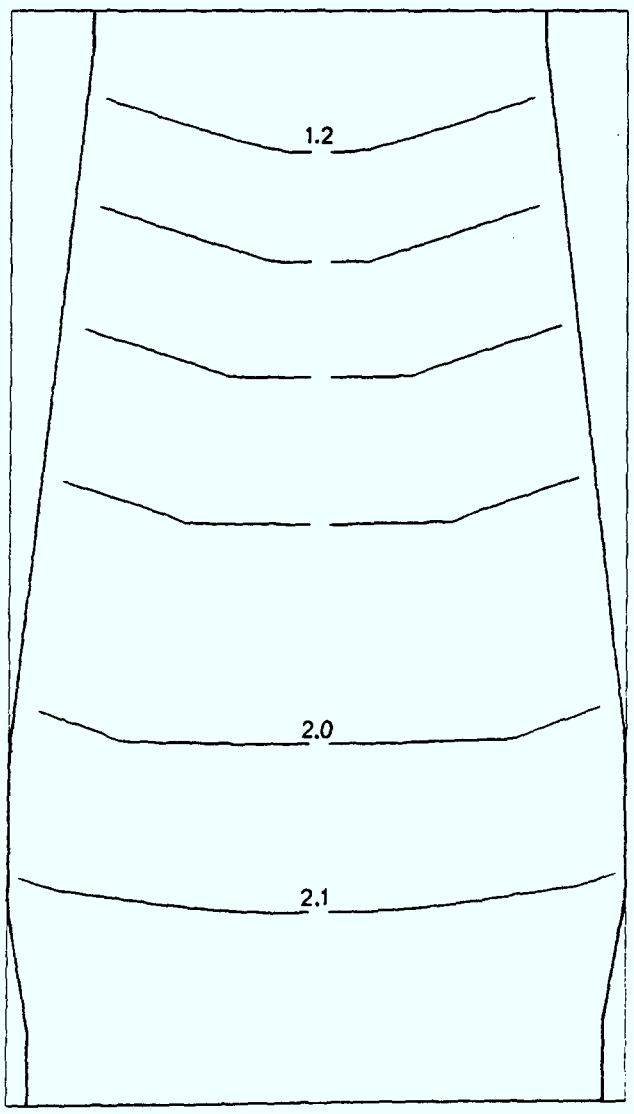

Figure 7.48: Pressure contours(bars)
-20%:rwB: std. profile

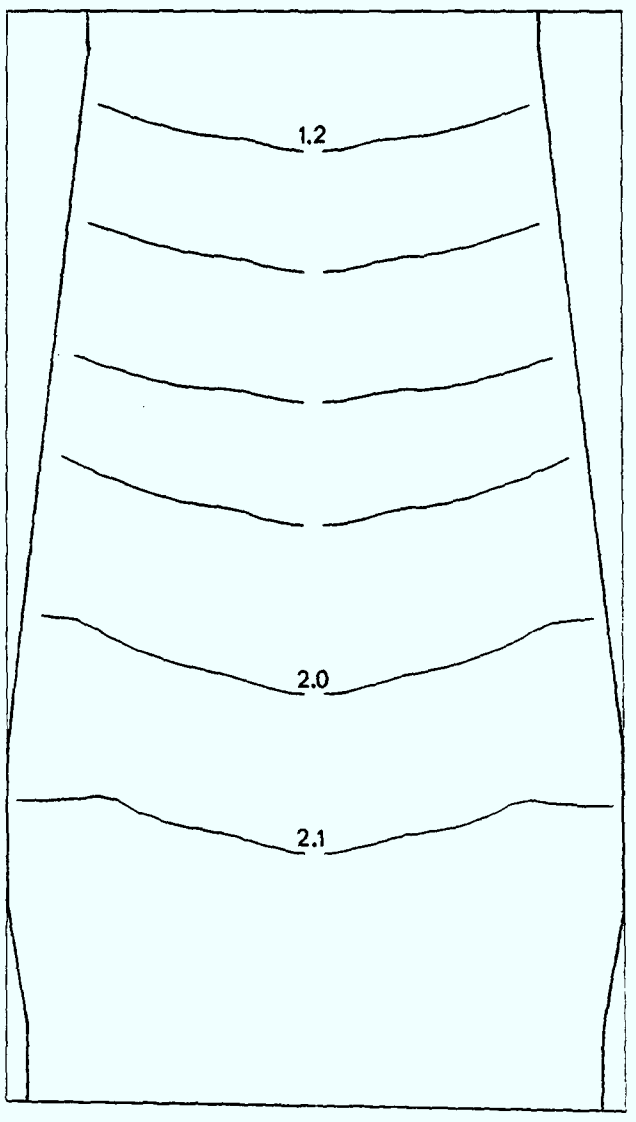

Figure 7.49: Pressure contours(bars)
-20%:rwB: profile a

particularly in the lower regions of the furnace. Two runs were performed to give an initial idea as to the dependence of the furnace on the deadman. A stagnant coke zone was set up by prescribing a high resistance to flow, this was implemented by setting the voidage of the solids to 0·1 in the zone. A simple cone shape was used as a deadman of base radius 3½m and height 5m. It was therefore expected that the gas flow would channel along the path of least resistance and thereby avoid the deadman.

The temperature contours for the standard profile and profile (a) are given in Figures (7.50) and (7.51) while the corresponding pressure contours are given in Figures (7.52) and (7.53). Only the two profiles mentioned were used as it was believed that the effects on a furnace with a 'high' and 'low' cohesive zone would give good indication as to any causes for change. The results are compared to those of section 7.2. In both cases the overall axial pressure gradient increased, due to the inclusion of a region of higher resistance. It was also observed that in the lower region of the furnace the radial gradient increased; this being due to the gas distributing through a region of higher resistance. For the standard profile case the cohesive zone remained unchanged while in the case of profile (a) the zone's central region lowered. This is consistent with the argument of effects being local and not affecting the furnace globally.

Similar conclusions are drawn about the deadman as for the inclusion of raceway shapes. The high resistance area of the stagnant coke only appears to affect the cohesive zone when it is located in the vicinity of higher resistance. This implies that although the deadman was not included in the standard mathematical model, its

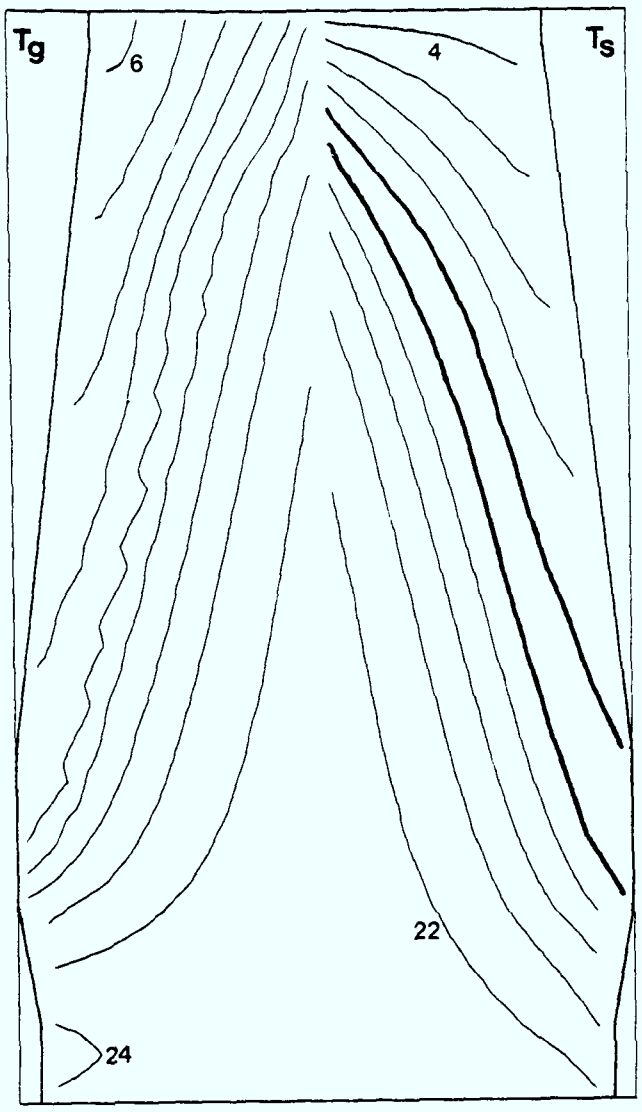

Figure 7.50: Temperature contours(10^2K)
DM: std. profile

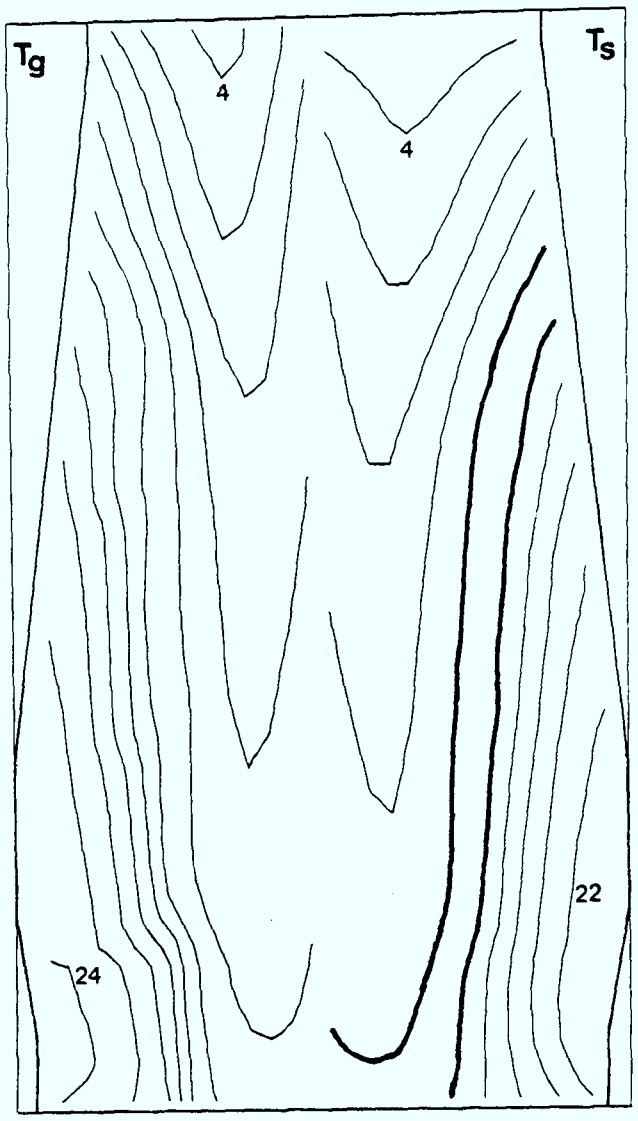

Figure 7.51: Temperature contours(10^2K)
DM: profile a

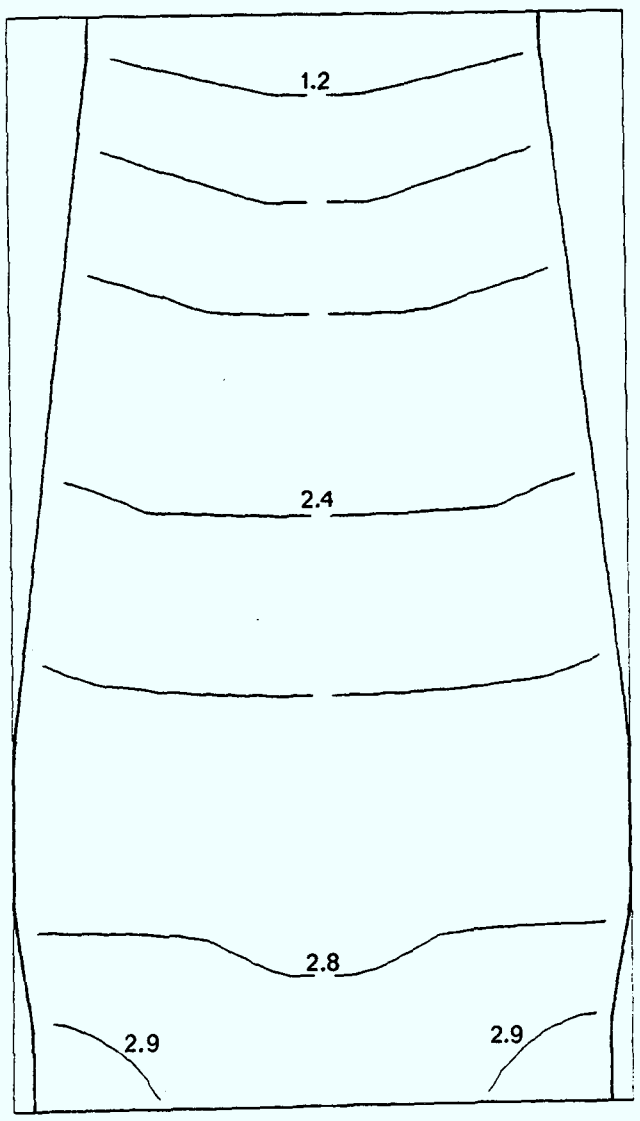

Figure 7.52: Pressure contours(bars)
DM: std. profile

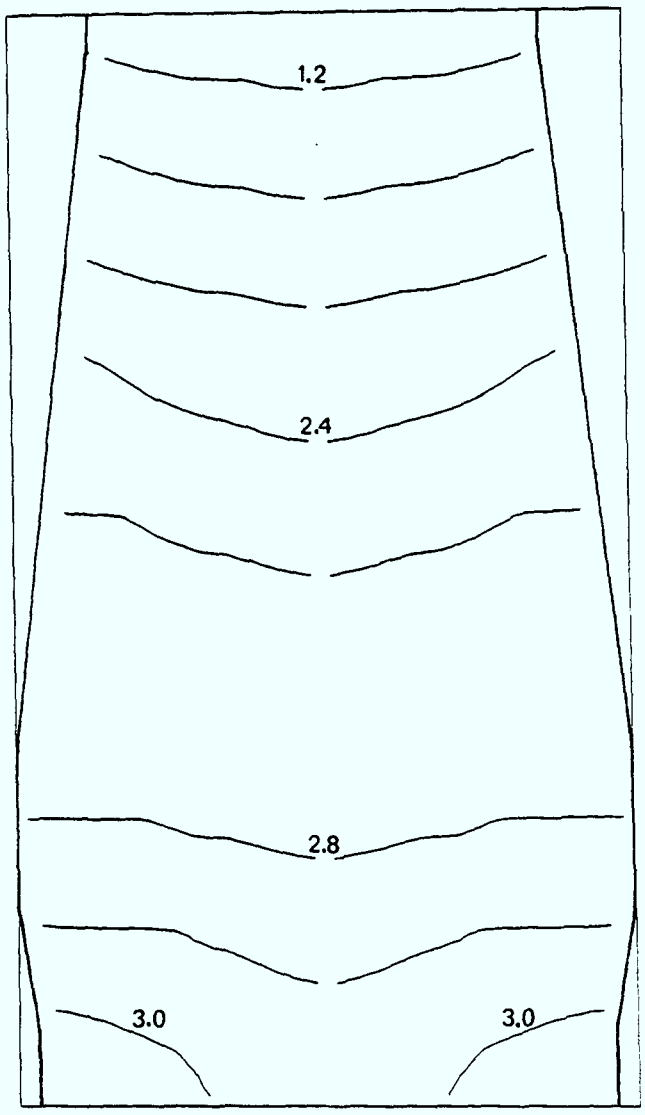

Figure 7.53: Pressure contours(bars)
DM: profile a

importance compared to other factors included, is secondary.

7.6 Conclusion

A variety of changes were performed on the basic mathematical model of chapter 4. It was desired to identify the sensitivity of the cohesive zone geometry to a number of factors, and to identify the role of the raceway with respect to the complete furnace system.

Changes to the ore:coke profile proved to be of high significance in determining cohesive geometry. This is due to the profile being directly linked to the determination of resistance magnitude and therefore affecting flow distribution. On addition of raceway shapes, to observe the effects of penetration and vertical growth, important results were obtained. The effects of raceway addition are only observed when the cohesive mass is in the raceway vicinity. When the furnace lower region is predominantly active coke, the effects to cohesive geometry and position are negligible. On exiting the raceway region the gas rapidly distributes through the coke, returning to familiar gas profiles. The vertical growth of the raceway did encourage peripheral flow but only when the cohesive mass was in the raceway vicinity. The changing of charging angle had an effect on the pressure gradients, as was expected. However, the raceway shapes, for the varying angle, only affected the cohesive mass when it was in the vicinity. It is concluded that although the angle is directly linked to the directional resistances, its effects on determining magnitude will only be apparent in the cohesive and stack zones.

The role of the stagnant coke zone was observed to be of secondary importance as it affects gas flow distribution in the local vicinity

only. Therefore it was concluded that excluding the deadman from the basic mathematical model was not primarily important.

CHAPTER 8

DISCUSSION AND CONCLUSIONS

8.1 Introduction

The mathematical model of the iron blast furnace was developed to analyse aspects of furnace behaviour. The model included the varying zones structures so as to determine the resistance changes, thus enabling an accurate gas distribution to be calculated. Many complex aspects were included in the model, and the provision for varying these was inherently built in.

The solution procedure for the above model was designed around an existing solver. Major developments and improvements had to be made to the original solver due to its limitations when dealing with certain classes of two phase flows. The reasons for choosing the particular solution algorithm employed, together with the basic philosophy for its modifications, are given later in section 8.2.

The experimentation performed gave insight into the difficult aspects of building an analogue and improved the understanding of furnace behaviour. The various redesigns of furnace and particle properties helped to identify future needs when modelling raceway phenomena, both physically and mathematically. As with the model results, the important factors influencing the cohesive zone were identified. More importantly, the effects of raceway geometry on the overall furnace structure were brought to light.

The following chapter is a conclusion of the results obtained, together with a discussion as to why certain routes were taken. Further work is suggested within the context of the conclusions drawn; this enables the importance of the results to be put into perspective.

8.2 Solution Procedure

As stated in chapter 5, the solution procedure employed is based on the PHOENICS computer program. This was chosen as it provided the only code available to have embedded, a two phase algorithm capable of representing interspersed phenomena. Another multi-phase code, known as SMAC (simplified marker and cell algorithm, see Bush and Marshall (1985)), was not appropriate as the iterative scheme relied on the time dependent equations for the non-linear terms. There was also some uncertainty as to its capabilities with highly interspersed phases, as the applications it was associated with were of a two 'separate' phase nature.

The algorithm implemented, in the PHOENICS code, to solve the differential equations was stated as SIMPLEST. This is true for one phase calculations but, strictly speaking, not so for a two phase problem of the kind presented. For two phase calculations, the code employs an algorithm known as IPSA (inter-phase-slip algorithm, see Rosten and Spalding (1981); Spalding (1985)). It will be presented here: the basic ideas behind IPSA; the reasons why it is not practical in the case considered; and, the method used for overcoming the problems, thus returning to what is effectively an extended SIMPLEST algorithm.

Shared pressure algorithm

In many two phase problems, the phases are subjected to a common pressure. The IPSA algorithm tackles this compilation by computing one pressure field from the two continuity equations. There is also the complication of the volume fraction to be considered, and this is solved in connection with the pressure and continuity equations. An outline of the iterative procedure is as follows:

i) Solve for the volume fractions,

ii) Solve for velocities,

iii) From a joint continuity equation, solve for pressure corrections.

Volume fractions. To take each of these steps in turn, the method for solving the volume fractions is described. A series of algebraic manipulations on the momentum equations leads to a relatively simpler set of eight equations:

$$L\{U_{ij}, pp\} = 0 \qquad (8.1)-(8.8)$$

where U stands for either V or W as appropriate, i stands for the subscript g or s, and j stands for the location n,s,e or w. The two continuity equations can be written as:

$$L\{r_g, W_{gn}, W_{gs}, V_{ge}, V_{gw}\} = 0 \qquad (8.9)$$

and

$$L\{r_s, W_{sn}, W_{ss}, V_{se}, V_{sw}\} = 0. \qquad (8.10)$$

(Equation (8.9) is the same as equation (5.18), and so it is clear what form equation (8.10) takes). A further equation is used, and that is the statement that the phases together occupy the whole volume, as set down in the form of equation (4.2). On substituting for the velocities in equations (8.9) and (8.10), from equations (8.1) to (8.8), the result for the volume fractions are:

$$L\{r_g, pp\} = 0 \qquad (8.11)$$

and

$$L\{r_s, p_p\} = 0. \qquad (8.12)$$

This is the form of the equations used in the solution of the volume fractions. Some further algebraic manipulation takes place, so as to speed up convergence, while ensuring adherance to the statement of (4.2) at all times.

Velocities. The solution of the velocities is the same as that laid down in chapter 5. In the case of the IPSA algorithm, dealing with two phases, there is also a corresponding set of equations for the solids phase velocities.

Pressures. The pressure correction is derived from the joint continuity equations. From previous calculations the r's and U's will not satisfy the mass balance equations immediately. In the IPSA algorithm, it is up to the pressure solution to restore the balances, by using a shared pressure. The procedure for arriving at a joint pressure correction equation will now be given; it should be noted how similar the method is to that in the SIMPLEST algorithm, the difference being that the errors (ie. imbalances) now contain those for both phases. Net mass sources arise, for each cell and phase, from the previously calculated r's and U's. These are divided by the local densities of the relevant phases and added together to create a set of volumetric imbalances. The volumetric imbalance can be written as a linear function of all the velocity components influencing the cell (ie. both phases), giving

$$\text{Error} = \sum_{\text{face}} \sum_{\text{phase}} (FU^*_{ij} + G) \qquad (8.13)$$

where F and G are constants. To reduce this error to zero the velocity corrections must satisfy

$$- \text{Error} = \sum_{\text{face}} \sum_{\text{phase}} FU'_{ij} \,. \qquad (8.14)$$

The pressure change required to bring about the desired velocity correction is obtained from the momentum equations, and given as:

$$U'_{ij} = H(p'_{nb} - p'_P) \qquad (8.15)$$

where H is a differential coefficient and the subscript nb stands for the relevant neighbouring cell. Note the form of (8.15) is that for equations (5.24) and (5.25). Combining equations (8.14) and (8.15) thus gives the form of the pressure correction equation,

$$- \text{Error} = \sum_{\text{face}} \left(\sum_{\text{phase}} FH\right)(p'_{nb} - p'_P) \,. \qquad (8.16)$$

This pressure correction equation now contains the imbalances of both phases and will be solved to produce a shared pressure. The complete set of equations, represented by (8.16), are solved over the whole field, thereby correcting the complete field each iteration.

The similarities between IPSA and SIMPLEST can now be drawn. In section 5.4.1, the iterative process of SIMPLEST is given in step form. The IPSA algorithm changes these steps by: adding the iterative solution of the volume fractions, between steps i) and ii); increasing the number of momentum equations to be solved, in step ii), by the addition of the solids momentum; and, replacing the

pressure correction equation, in step iii), by a joint continuity pressure correction equation. The remaining calculations, for updating the velocities and pressure, together with solution of the energy equations, remain the same.

Physical problems

Having described the ideas behind the IPSA algorithm, it is now necessary to draw attention to the physical problems encountered, when trying to apply this method to the problem considered. The flow characteristics of the blast furnace are: gases ascending through a packed bed of solids descending. The gas is driven through the furnace by a pressure gradient from the tuyere exit to furnace top. However, the solids flow is gravity induced, and the mass flowrate is determined by the rate of combustion in the raceway and the rate of iron drainage in the hearth. The rates of combustion and drainage are relatively slow, and so the solids flow is caused by the gravitational force inducing the filling of the space made available by the aforementioned methods, rather than a pressure gradient inducing flow. In the model, the gas flow is simulated by prescribing a mass inflow and allowing a pressure gradient to drive the gas. For the solids, the combustion and drainage rates are simulated by a single massflow rate entering or exiting the furnace system. The pressure gradient directions for both phases will be explained and they can be seen diagramatically in Figure (8.1). In the case of the gas flow, the effects of gravity are negligible when determining the pressure gradient, Δp_g. The top pressure, p, is fixed and shared by both phases. On determining the solids flow however, the effects of gravity are most significant. If the pressure gradient opposing the force of gravity, were not present, the solids would flow through the furnace

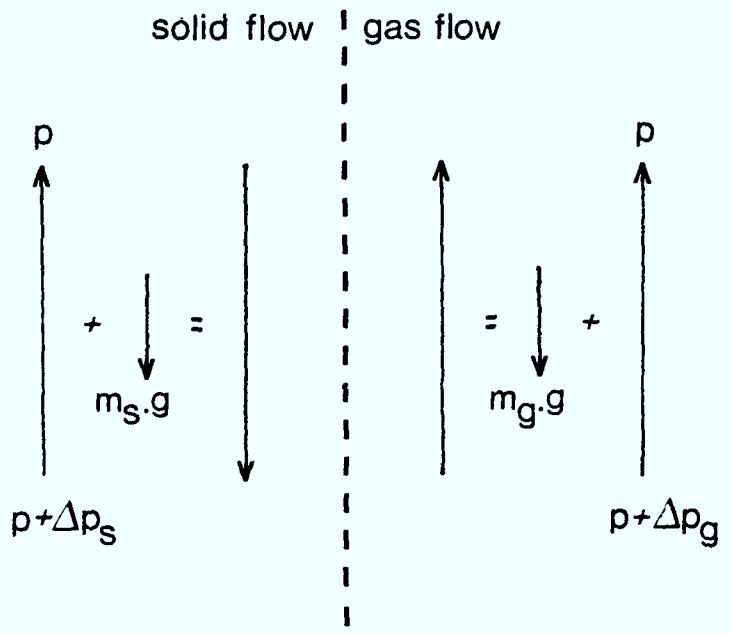

Figure 8.1: Pressure gradients for gas and solids flow.

at an extremely high rate. As the flowrate is predetermined in the simulation, to a very low rate, the pressure gradient must counteract the gravitational force. Therefore the gradient, Δp_s, should be determined according to the required mass flowrate.

As the two phase algorithm, IPSA, uses a shared pressure, it can be seen why a correct solution will not be obtained. For the pressure to be shared, the two independent gradients, Δp_g and Δp_s, must be the same. This is clearly not the case, and neither gradient can be adjusted to equal the other, as both phase mass flowrates are predetermined. Therefore, to enable the simulation to proceed, the pressure must only be used to determine gas flowrates, as is the situation in the physical case. What is needed then, is modification to the IPSA algorithm so that the pressure correction is dependent on the gas phase only.

Modifications to IPSA

The modification was achieved by; solving for the solid phase momentum outside the algorithm, then implementing the solution into the algorithm, leaving the pressure correction to reduce the gas phase volumetric errors. The method used for solving the solids momentum was the assumption of potential flow; a full account is given in chapters 4 and 5. It should be pointed out, how this new method of two phase solution (for the particular case considered), simulates the SIMPLEST algorithm described in chapter 5, when solving for the gas phase.

The differences, previously described between the two algorithms, no longer come into effect when using the modified algorithm for an independent solids momentum solution. Firstly, the volume fractions

are not solved for but retained at their previous evaluations, as described in section 4.2.1. Therefore the volume fractions solution, of IPSA, is no longer present. There was no change as to the velocities solution of the gas, thereby unchanging the IPSA algorithm, which in turn did not fundamentally alter from SIMPLEST. All that remains is to show how the pressure correction of IPSA, becomes effectively that of SIMPLEST.

The net mass sources arising, for each cell, from the previously calculated U's, are those for the gas phase only. This is due to the solids solution already satisfying continuity, before the IPSA algorithm starts. As a result, the volumetric imbalance, "Error", given in relationship (8.13), only contain imbalances for the gas. The joint pressure equation, (8.16), therefore solves for the corrections so as to reduce the gas volumetric imbalance. This is then effectively, a pressure correction equation influenced by the gas phase alone. (The pressure correction term, p', is used to obtain a velocity correction, U', for both phases. This does not alter the velocity field for the solids as the converged solution is used to overwrite any corrections).

It has therefore been shown how the IPSA algorithm, with its shared pressure, cannot solve for a problem of the type considered; or indeed any counter current packed bed system, where mass flowrates must be specified. The modification to the algorithms were therefore given, showing how the physical problems can be overcome by means of a successful solution procedure.

8.3 Experimentation

The experimental design of chapter 2 was brought about by a survey

into existing models and the needs of the research. The initial development to the furnace construction was performed, after a study of predicted raceway size took place. This study enabled the estimation of dimensions to use in order to obtain manageable results. It was desired that the raceway formed would be large enough to visualise easily and procure clear photographic results. On commencement of the experiment, the redesign of the complete apparatus became apparent, particularly in the furnace itself. The various furnace reconstructions and runs gave tremendous insight into the behaviour of the dry ice packed bed. These observations were supported further by the results obtained on changing the packed beds properties. On conclusion of the experiment, a new and successful technique for analysing raceway phenomena remained.

Some points to mention are those connected with the actual design features of both the apparatus and the simulating media. The second air delivery system used is intrinsically superior than the first. It was reported, in the running conditions of section 2.4.4, that the new system delivered a lower flowrate than previously. This was due to a resistance increase in the delivery line, due to the redesign. Despite lower rates being achieved, the new design has the capability of delivering a much higher flowrate by the simple upgrading of the cylinder regulators. Therefore the apparatus has achieved the potential to improve by performing relatively simple alterations. The inclusion of a flowmeter, producing results in real time, has meant improved accuracy in maintaining equal blast rates for all the tuyeres. This is an important feature as unequal blast rates can encourage azimuthal flow and effectively reduce the blast effect on raceway formation.

The use of dry ice as the simulation to coke particles proved satisfactory with respect to the sublimation properties. The problems encountered, with the packed bed not flowing freely, were shown to be due to the shape of the dry ice pellets. It is believed that this shape caused the existing hanging and bridging of particles to amplify. The addition of an inclined wall was not enough to reduce the problem, and it was only after the addition of a second, more spherical media, did the packed bed flow downwards. This directed the conclusions to look more closely at the shape of particles used. It was noted that, the mixed volumetric ratio of 1:1 was arrived at via experience with dry ice and to ensure the desired particle separation took place. If further work is to be carried out with the analogue, then an analysis to try to reduce the beans ratio should be performed. This would avoid the excessive build up of beans as the ice sublimates. A more desirable solution would be the acquisition of a more spherical dry ice pellet (or the second media having sublimation properties).

As the results pointed to the solids behaviour being critical in the vicinity of the raceway, it is clear as to how research in this area should proceed. As has been pointed out, and will be discussed later, the role of the raceway is not as significant as previously believed, when analysing the effects of flow distribution on the complete furnae structure. However, the modelling of the raceway is important in terms of: the chemical kinetics, mass transfer and solids flow distribution, and the effects on percolating molten iron. It is therefore believed that, research on the raceway, should be directed to analysing the solids behaviour. Not only modelling of the flow characteristics of packed beds, but stress analysis on packing and particle shape, and their role in the moving

bed. The present experimental analogue is well suited to studying flow characteristics above and around the raceway. The adaptations required would be the addition of some form of tracer particles to the bed. This could be achieved by dyeing the ice pellets (eg. with a coloured alcohol).

On looking at the complete physical study, from furnace modification to experimental results, one concluding factor can be drawn. That is, the furnace redesigns and packed bed change have been a direct consequence of the solids behaviour. The results repeatedly showed the vital role of the solids when looking at raceway formation, and not gas distribution properties alone. Granted, the change in tuyere diameter and blast rate showed a certain control over the raceway, but not as influential as the solids. This is an interesting result when brought along side the mathematical models' conclusions that, the raceway does not significantly affect furnace operation from a gas distribution point of view.

8.4 Numerical Modelling

The mathematical model, of chapter 4, was designed to simulate features of the iron blast furnace. The model involved the gas and solids flow distributions together with energy calculations and heat transfer. The addition of directional resistances to gas flow enabled the inclusion of zones into the model (ie. the variation of various ore and coke properties throughout the furnace). This in turn, enabled the prediction of zone geometries, particularly the position and geometry of the ore softening-melting zone (ie. cohesive mass). As explained in the opening chapter, the cohesive zone is of particular importance as it strongly influences the gas flow distribution, as well as softening and melting the ore.

Therefore, on varying parameters, it was decided to observe the results from the cohesive zone point of view, thus observing the effects on furnace behaviour.

The most significant change was that of the ore:coke charging profile. The results to these changes are reported in chapter 7. This result, however, was not new, but it assisted the validation of the model as described in chapter 6.

It was of interest to the current research to identify the significance of the raceway region, as regards its effects on the complete furance process. The results of chapter 7 brought to light the raceways' role, with respect to the effects on gas distribution and the resultant effects on the cohesive zones' geometry. It is clear that, the furnace internal geometry is not affected when the cohesive zone is not in the vicinity of the raceway. The effect of a large active coke zone in this area is that the gas is distributed very rapidly, thereby damping any local changes caused by a raceway. A change in the charging angle also confirmed these results. While the expected pressure change and the change of the flow in the stack occurred, little effect was had on the cohesive zone. As the active coke is so important in the distribution of gas, it would be of future interest to model the effects of percolating iron, in the context of the complete furnace process.

Although it has been concluded that the effects of raceway geometry are determined by the position of the cohesive zone (and are not as significant as believed when the effects come into play anyway), it must be remembered that this is with respect to the gas flow. The role of the raceway is still of vital importance as regards chemical

kinetics, as it is the main combustion zone for the coke.

In summary therefore, little attention need be paid to the raceway zone, when modelling the blast furnace from a flow distribution stand point. It is also of interest to note, in conjunction with the modelling conclusions, the results of the raceway experiment showing a higher dependence on particulate behaviour, rather than gas distribution only.

8.5 Conclusions

A mathematical model has been developed, to simulate various aspects of an iron blast furnace. This has involved the modelling of a counter current gas flow through a packed bed, looking at the momentum and energy equations of both phases. The addition of directional resistances has enabled the prediction of the geometry of various zones, thereby allowing an accurate analysis of the effects of parametric changes. Most important, is the ability to predict the location and geometry of the cohesive zone, as this is a vital region in the determination of gas distribution to the upper part of the blast furnace. The solution procedure used, was a modified version of an existing multi-phase algorithm (IPSA). The result was a significantly enhanced SIMPLEST algorithm, having the ability to solve for two phases (ie. gaseous and particulate) with interspersed counter current flow characteristics, where the particulate behaviour is that of a packed bed. It was shown why the original algorithm would not successfully predict results, due to the problems' counter current nature, and a successful alternative was presented.

In addition to the mathematical model, a physical model of the raceway was designed and operated, giving insight into the factors affecting raceway geometry. On performing the experiment, it was shown how important a role the particles play in determining a steady raceway. The effects of particle-particle interaction were shown to be most significant in enabling the packed bed to flow freely.

From the mathematical results, it was concluded that the ore:coke charging profile played a vital role in determining the behaviour in

the furnace. More importantly, the conclusion that the raceway zone does not play a significant role in the determination of gas distribution, was brought to light. More specifically, the raceway has little effect when the cohesive zone is not in the immediate vicinity, thereby leaving the active coke zone as predominant.

What does this research show as regards blast furnace modelling? The main concluding thrust, of both the physical and mathematical model, is to highlight the insignificant role of raceway geometry when modelling the blast furnace, from an inert view point. It is therefore suggested that future modellers do not get unnecessarily diverted by the detailed fluid flow behaviour of the raceway zone.

NOMENCLATURE

$A_{e,w,n,s}$	areas at control volume faces e,w,n,s.
$A_{E,W,N,S}$	coefficients corresponding to nodal positions E,W,N,S.
$\bar{A}_s$	surface area of solids per unit volume.
$\underline{a}_{grav}$	gravitational constant vector.
C_Φ	'coefficient' for source term of variable Φ (equation (5.31)).
C_g, C_s	specific heat capacity of gas and solids.
d_p	diameter of solids particles.
F_g	friction factor.
F_1, F_2	inertial resistance for coke and ore.
f_1, f_2	viscous and inertial resistances.
$\bar{f}_2$	inertial resistance averaged at furnace top boundary.
f_x, f_y	directional resistances.
g	constant for acceleration due to gravity.
$\underline{\underline{H}}$	matrix associated with resistances (equation (4.10)).
h	heat transfer coefficient.
h_g, h_s	thermodynamic enthalpies for gas and solids.
$\underline{i}$	direction vector.
k_g, k_s	thermal conductivity of gas and solids.
L	latent heat of melting of ore.
$L\{\}$	linear function of variables.
L_b	furnace packed bed height.
M_A	molecular weight of air.
m_o	mass fraction of ore.
$\dot{m}$	mass flowrate.
m_g, m_s	mass of gas or solids.
p	pressure.
p_{ext}	pressure at top of furnace.
p_g, p_s	pressure for gas and solids.

R_o	molar (universal) gas constant.
R	magnitude of radius at furnace top.
r	radial distance.
r_g, r_s	volume fractions for gas and solids.
r_p	radius of a solids particle.
S_Φ	source term for dependent variable Φ.
S_{Φ_P}	source term for control volume of nodal point P.
$S^C_{\Phi_P}, S^P_{\Phi_P}$	constant and coefficient for linearised source.
T	temperature.
T_g, T_s	temperature for gas and solids.
T_g^{in}, T_s^{in}	input temperature for gas and solids.
T_u, T_ℓ	upper and lower temperature limits for cohesive zone.
U	velocity.
U_{ij}	velocity component.
$\bar{U}_g$	superficial gas velocity (scalar).
V	volume.
V_C	volume of control cell.
V_Φ	'value' for source term of variable Φ (equation (5.31)).
$\bar{V}_g$	gas velocity (scalar).
$\underline{V}_g, \underline{V}_s$	velocity vector for gas and solids.
V_g, V_s	radial velocity component for gas and solids.
W_g, W_s	axial velocity component for gas and solids.
W_s^{in}	axial input velocity for solids.
z	axial distance.

Greek

α	coke volume fraction.
β	gas mass flowrate.
Γ_ϕ	transport coefficient for dependent variable ϕ.
γ	constant representing resistance to flow (equation (4.34)).
Δp	increment of pressure.
$\Delta r, \Delta z$	control volume dimensions.
$\delta r, \delta z$	increments between nodes in relevant direction.
ϵ	packed bed porosity.
Θ	circumferential distance.
θ	angle of inclination of layers.
λ	constant for stream function boundary condition.
μ_g	laminar viscosity of gas.
π	pi ; (3·141593).
ρ	density.
ρ_g, ρ_s	density of gas and solids.
$\bar{\rho}_g$	average density of gas at furnace top boundary.
ρ_o, ρ_c	density of ore and coke.
τ	wall shear stress.
ϕ	dependent variable.
$\bar{\phi}_s$	shape factor of solids particles.
ψ	stream function.
ω	solids mass inflow.
$\bar{\omega}$	relaxation parameter for SOR.

Subscripts

e,w,n,s	east,west,north,south control volume faces.
E,W,N,S	east,west,north,south nodal positions.
g	gas phase.
I,J	position on stream function grid (Figure (5.6)).
i,j	position on scalar grid (Figure (5.6)).
ij	i phase and j control face location.
nb	neighbouring cell nodal position.
s	solids phase.

Superscripts

in	input value.
(K)	K^{th} value in iterative scheme.
*	previous calculated value.
'	correction factor.

Mathematical symbols

$[\![a,b]\!]$	maximum a or b.
∇	vector derivative.
$\nabla\times$	curl.

REFERENCES

BIRD R B, STEWART W E & LIGHTFOOT E N (1960)

Transport Phenomena: Published by Wiley International Edition.

BONNEKAMP H, ENGEL K, GREBE K & WINZER G (1984)

"The Freezing with Nitrogen and Dissection of Mannesmanns' No.5 Blast Furnace": Presented to Ironmaking Conference, Chicago; April 1-4.

BUSH A W & MARSHALL G S (1985)

"The SMAC code for Multi-phase flow: A First Approach": Presented to Polymodel Conference, Teesside Polytechnic; May 22-23.

CROSS M & GIBSON R D (1979)

"Gas Flow Through Multilayered Regions of Porous Media": Powder Technology, Vol.24, pp.167-178.

CROSS M, GIBSON R D & HILL P (1980)

"Factors Affecting the Cohesive Zone Shape of Large Blast Furnaces": British Steel Corporation report No.T/IM/1036/1/80/D; Dec.29.

CROSS M, GIBSON R D, MOON J T & TRAICE F B (1981)

"Factors Affecting the Gas Flow Characteristics of Blast Furnaces": Presented to Minnesota Section AIME 54th Annual Meeting, Duluth, Minnesota; Jan.

CROSS M, GIBSON R D, TONKS M G & TRAICE F B (1984)

"Towards a comprehensive Mathematical Model of the Iron Blast Furnace": Presented to AIME-SME/TMS 1st International Symposium on Automatic Control in Mineral Processing and Process Technology, L A, California; Feb.26-March 2.

CROSS M, MOON J T, GIBSON R D, TONKS M G & PINYOUN M J (1979)

"Experimental Verification of the Practical Theory to Describe the Gas Flow Through the Blast Furnace": British Steel Corporation Report No. T/IM/1106/2/79/D; March.

DUNCAN W J, THOM A S & YOUNG A D (1970)

Mechanics of Fluids: Published by Edward Arnold, 2nd Edition.

DURNOV V K, BABUSHKIN N M, KITAEV B I, SCHERBATSKY V B & SHABEL'ZON B M (1981)

"Investigation of Raceway Dynamics on a model": International Blast Furnace Hearth and Raceway Symposium, pp.6-1/6-7.

ELLIOT J F, BUCHANAN R A & WAGSTAFF J B (1952)

"Physical Conditions in the Combustion and Smelting Zones of a Blast Furnace": Transactions AIME, Journal of Metals, pp.709-717; July.

ERGUN S (1952)

"Fluid Flow Through Packed Columns": Chemical Engineering Progress, Vol.48, No.2, pp.89-94; Feb.

ERGUN S & ORNING A A (1949)

"Fluid Flow Through Randomly Packed Columns and Fluidized Beds": Industrial and Engineering Chemistry, Vol.41, No.6, 1179-1184; Jan.

FIELDEN C J & WOOD B I (1968)

"A Dynamic Digital Simulation of the Blast Furnace": BISRA Industry Report No.PE/B/26/68.

GARDNER G C (1960)

"A New Correlation of Blast Penetration in a Blast Furnace": Transactions of Metallurgical Society of AIME, Vol.218, pp.423-428; June.

GREBE K & de HAAS H (1983)

"In-Situ Behaviour of Pellets in Direct Reduction and Blast Furnaces": Ironmaking Proceedings, Vol.42, pp.149-159.

HATANO M, HIRAOKA B, FUKUDA M & MASUIKE T (1977)

"Analysis of the Combustion Zone in the Experimental Blast Furnace": Transactions ISIJ, Vol.17, pp.102-109.

HATANO M, KURITA K & TANAKA T (1983)

"Aerodynamic Study on Raceway in Blast Furnace": Ironmaking Proceedings, Atlanta, ISS-AIME, Vol.42, pp.577-586.

HATANO M, MIYAZAKI T & IWANAGA Y (1980)

"Mathematical Model for Blast Furnace Operation Considering the Degradation of Coke by Gasification": Transactions ISIJ, Vol.20, pp.293-300.

HILLNHUTTER F W, KISTER H & KRUGER B (1975)

"Investigation of the Phenomena of Movement in Front of the Tuyeres of a Blast Furnace using and Endoscope": Ironmaking Proceedings AIME, Vol.34, pp.368-382.

KANBARA K et al (1976)

"Internal Conditions of a Blast Furnace as Revealed by Dissection": Tetsu-to-Hagane, Vol.62, (5) 535-546.

KINNEY S P, ROYSTER P H & JOSEPH T L (1927)

"Iron Blast-Furnace Reactions": Department of Commerce, Bureau of Mines technical paper 391.

KUDOH J, TAKEDA K, YAGI J & OMORI Y (1983)

"Gas Flow and Heat Transfer Analysis for the Blast Furnace Operation": Ironmaking Proceedings, Atlanta, ISS-AIME, Vol.42, pp.615-627.

KUWABARA M, HSIEH Y, ISOBE K & MUCHI I (1981)

"Mathematical Modelling of the Tuyere Combustion Zone of the Blast Furnace": International Blast Furnace Hearth and Raceway Symposium, pp.7-1/7-11.

KUWABARA M, ISOBE K, MIO K, NAKANISHI K & MUCHI I (1983)

"A Mathematical Representation of Physical & Chemical Phenomena In The Lower Part of Blast Furnace": Proc Joint Symposium ISIJ & Aus.IMM, Tokyo, Japan; Oct.13-14.

KUWABARA M & MUCHI I (1975)

"Theoretical Analysis of Blast Furnace Operation Based on the Gas Flow through Layered Ore and Coke Burdens": Aus.IMM, Illawarra Branch - BFA Symposium, Wollongong, pp.61-67.

KUWABARA M & MUCHI I (1977a)

"Mathematical Model of Blast Furnace with Horizontally Layered Burdens": Transactions ISIJ, Vol.17, pp.271-278.

KUWABARA M & MUCHI I (1977b)

"Mathematical Model of Blast Furnace with Radially Distributed Burdens": Transactions ISIJ, Vol.17, pp.321-329.

KUWABARA M & MUCHI I (1977c)

"Theoretical Analysis of Gas Flow in Shaft with Layered Burdens": Transactions ISIJ, Vol.17, pp.330-338.

McCUTCHEON K C (1965)

"The Tuyere Raceways and Smelting Zone in the Blast Furnace": Blast Furnace and Steel Plant for October, pp.930-937.

McINTEE C J K & ROBERTSON T (1981)

"The Development of a Physical Analogue of a Large Blast Furnace": British Steel Corporation Report No.T/BS/1254/5/81/D; Dec.

McINTEE C J K, ROBERTSON T & YOUNG R W (1982)

"The Validation Exercise for the Large Blast Furnace Model Using Results Obtained from a Physical Analogue": British Steel Corporation Report No.T/BS/1254/6/82/D; April.

MACKIN K G (1979)

"Kinetic Model of the Blast Furnace": British Steel Corporation Report No.WL/80/1075/79/D; Feb.

MARKATOS N C, RHODES N & TATCHELL D G (1982)

"A General Purpose Program for the Analysis of Fluid Flow Problems": Numerical Methods for Fluid Dynamics, Academic Press, New York, pp.463-480.

MILNE-THOMSON L M (1952)

Theoretical Aerodynamics: Published by Macmillan and Co., 2nd Edition.

MUCHI I (1967)

"Mathematical Model of Blast Furnace": Transactions ISIJ, Vol.7, pp.223-237.

NERDD PROJECT (1983)

Final Report "Replacement of Oil by Coal Injection at the Blast Furnace": No.79/9/85; July 1980-March 1983.

PATANKAR S V (1980)

Numerical Heat Transfer and Fluid Flow: McGraw-Hill Book Company, Hemisphere Pub. Corp.

PERROTT G & KINNEY S P (1923)

"Combustion of Coke in Blast-Furnace Hearth": Transactions of AIMME, Vol.69, pp.543-586.

POVEROMO J J, SZEKELY J & PROPSTER M (1975)

"Flow Maldistribution in the Iron Blast Furnace": Aus.IMM, Illawarra Branch - BFA Symposium, Wollongong.

PROPSTER M & SZEKELY J (1979)

"Gas Flow Through Cohesive Zone of Blast Furnace": Ironmaking and Steelmaking, No.5, pp.209-220.

ROSTEN H I & SPALDING D B (1981)

"The Mathematical Basis of the PHOENICS-EARTH Computer Code": CHAM TR/58b; Jan.

SMITH G D (1978)

Numerical Solution of Partial Differential Equations: Finite Difference Methods: Published by Clarendon Press, Oxford, 2nd Edition.

SOHN H Y (1978a)

"The Law of Additive Reaction Times in Fluid-Solid Reactions": Metallurgical Transactions B, Vol.9B, pp.89-96; March.

SOHN J Y (1978b)

"Mathematical Models of Iron Ore Reduction": Presented to The International Conference "Physical Chemistry and Steelmaking 1978", Versailles; Oct.23-25.

SPALDING D B (1980a)

"Modelling of Fluid-Mechanics, Heat-Transfer and Chemical-Reaction Processes": A lecture course, Imperial College, CFDU Report HTS/80/1.

SPALDING D B (1980b)

"Numerical Computation of Multiphase Fluid Flow and Heat Transfer": Recent Advances in Numerical Methods in Fluids, Editors - C Taylor and K Morgan, pp.139-167.

SPALDING D B (1981)

"A General Purpose Computer Program for multi-dimensional, one- and two- phase flow": Mathematics and Computers in Simulation, North Holland Press, Vol.23, pp.267-276.

SPALDING D B (1985)

"The Numerical Computation of Multi-phase Flows": Presented to Polymodel Conference, Teesside Polytechnic; May 22-23.

STANEK V & SZEKELY J (1972)

"The Effects of Non-Uniform Porosity in Causing flow Maldistributions in Isothermal Packed Beds": The Canadian Journal of Chemical Engineering, Vol.50, pp.9-14; Feb.

STANEK V & SZEKELY J (1973)

"Flow Maldistribution in Two Dimensional Packed Beds Part II: The Behaviour of Non-Isothermal Systems": The Canadian Journal of Chemical Engineering, Vol.51, pp.22-30; Feb.

STANEK V & SZEKELY J (1974)

"Three-Dimensional Flow of Fluids Through Non-uniform Packed Beds": AIChE Journal, Vol.20, No.5, pp.974-980; Sept.

SZEKELY J & KAJIWARA Y (1979a)

"A Mathematical Representation of Spatially Non-Uniform, Counter-current Flow of Gases and Liquids in Packed Beds - of Relevance to Flow Phenomena in the Bosh of Iron Blast Furnaces": Transactions ISIJ, Vol.19, pp.76-84.

SZEKELY J & KAJIWARA Y (1979b)

"The Interaction Between Gas and Liquid Flow in a Simulated Blast Furnace: A Preliminary Investigation": Metallurgical Transactions B, Vol.10B, pp.447-450; Sept.

SZEKELY J & POVEROMO J J (1975a)

"A Mathematical and Physical Representation of the Raceway Region in the Iron Blast Furnace": Metallurgical Transactions B, Vol.6B, pp.119-130; March.

SZEKELY J & POVEROMO J J (1975b)

"Flow Maldistribution in Packed Beds: A Comparison of Measurements with Predictions": AIChE Journal, Vol.21, No.4, pp.769-775; July.

SZEKELY J & PROPSTER M (1977)

"Resistance of Layer-charged Blast Furnace Burdens to Gas Flow": Ironmaking and Steelmaking, No.1, pp.15-22.

SZEKELY J & PROPSTER M (1979a)

"The Structure and Flow Resistance of Layer Charged Particulate Systems in the Modelling of Gas Flow through Simulated Blast Furnace Burdens": Transactions ISIJ, Vol.19, pp.11-20.

SZEKELY J & PROPSTER M (1979b)

"Theoretical Prediction of Non-uniform Gas Flow Through Simulated Blast Furnace Burdens": Transactions ISIJ, Vol.19, pp.21-31.

TAGGART I J, PINCZEWSKI W V, McCARTHY M J & BURGESS J M (1983)

"Recirculating Gas Flow in the Blast Furnace Raceway Zone": 8th Australian Fluid Mechanics Conference, Univ of Newcastle, NSW, Australia; Nov.28-Dec.2.

TASHIRO K, KANAYAMA U, HARA Y, OKUNO Y & FUJITA K (1980)

"Behaviour of Cohesive Zone in Blast Furnace": Presented to International Ironmaking Conference, Arles, France; June 2-4.

TOGINO Y, SUGATA M & YAMAGUCHI K (1980)

"Estimation of Lower Limit of Fuel Rate in Blast Furnace by Mathematical Model": Transactions ISIJ, Vol.20, pp.639-645.

TURKDOGAN E T (1978)

"Blast Furnace Reactions": Metallurgical Transactions B, Vol.9B, pp.163-179; June.

WAGSTAFF J B (1953)

"Further Studies of the Tuyere Zone of the Blast Furnace": Transactions AIME, Journal of Metals, pp.895-902; July.

WAGSTAFF J B & HOLMAN W H (1957)

"Comparison of Blast Furnace Penetration with Model Studies": Transactions AIME, Journal of Metals, pp.370-376; March.

WAKAYAMA S, KANAYAMA Y & OKUNO Y (1979)

"Characteristics and Control of burden distribution in the Blast Furnace": Ironmaking and Steelmaking, No.6, pp.261-267.

YAGI J & MUCHI I (1970)

"Theoretical Estimations on the Longitudinal Distributions of Process Variables in Blast Furnace and on its Productivity": Transactions ISIJ, Vol.10, pp.392-405.

YAGI J & SZEKELY J (1977a)

"A Mathematical Formulation for the Reduction of Iron Oxide Pellets in Moving Beds with Non-Uniform Gas and Solids Flow": Transactions ISIJ, Vol.17, pp.569-575.